

**Alma Mater Studiorum – Università di Bologna**

**DOTTORATO DI RICERCA IN**

**Geofisica**

Ciclo XXVI

**Settore Concorsuale di afferenza: 04/A4**

**Settore Scientifico disciplinare: GEO/10**

**TITOLO TESI**

**Numerical modeling of the Alto Tiberina  
low-angle normal fault mechanics**

**Candidato**

Luigi Vadacca

**Relatore**

Dr. Emanuele Casarotti

**Coordinatore Dottorato**

Prof. Michele Dragoni

**Esame finale anno 2014**

## Abstract

The aim of this Thesis is to obtain a better understanding of the mechanical behavior of the active Alto Tiberina normal fault (ATF). Integrating geological, geodetic and seismological data, we perform 2D and 3D quasi-static and dynamic mechanical models to simulate the interseismic phase and rupture dynamic of the ATF. Effects of ATF locking depth, synthetic and antithetic fault activity, lithology and realistic fault geometries are taken in account. The 2D and 3D quasi-static model results suggest that the deformation pattern inferred by GPS data is consistent with a very compliant ATF zone (from 5 to 15 km) and Gubbio fault activity. The presence of the ATF compliant zone is a first order condition to redistribute the stress in the Umbria-Marche region; the stress bipartition between hanging wall (high values) and footwall (low values) inferred by the ATF zone activity could explain the microseismicity rates that are higher in the hanging wall respect to the footwall. The interseismic stress build-up is mainly located along the Gubbio fault zone and near ATF patches with higher dip ( $30^{\circ} < \text{dip} < 37^{\circ}$ ) that we hypothesize can fail seismically even if a typical Byerlee friction (0.6-0.75) is assumed. Finally, the results of 3D rupture dynamic models demonstrate that the magnitude expected, after that an event is simulated on the ATF, can decrease if we consider the fault plane roughness.

# Contents

<b>1. Introduction.....</b>	<b>5</b>
<b>2. The Alto Tiberina low-angle normal fault.....</b>	<b>7</b>
2.1. Introduction.....	7
2.2. Tectonic setting.....	7
2.3. Seismicity.....	9
2.4. Long-term and short-term deformation.....	10
2.5. Geometries.....	12
2.6. Frictional reactivation theory for normal faults.....	15
2.7. Open questions.....	17
<b>3. Numerical method.....</b>	<b>18</b>
3.1. Introduction.....	18
3.2. Finite element method (FEM).....	18
3.2.1. <i>Comsol Multiphysics</i> .....	19
3.2.2. <i>PyLith</i> .....	20
3.3. Spectral element method (SEM).....	21
3.3.1. <i>SPECFEM3D</i> .....	22
3.4. Fault implementation.....	24
<b>4. Modelling the interseismic deformation of the Alto Tiberina     fault system by 2D numerical simulations: locking depth,     fault activity and effects of lithology.....</b>	<b>26</b>
4.1. Introduction.....	26
4.2. Modelling description.....	27
4.3. Model results.....	37
4.3.1. <i>ATF locking depth effects</i> .....	37
4.3.2. <i>Synthetic and antithetic fault activity effects</i> .....	40
4.3.3. <i>Lithology effects</i> .....	51

4.4. Discussion and concluding remarks.....	53
<b>5. Modelling the interseismic deformation of the Alto Tiberina fault system by 3D numerical simulations: fault roughness effects.....</b>	<b>57</b>
5.1. Introduction.....	57
5.2. Model description.....	57
5.3. Model results.....	61
5.4. Discussion and concluding remarks.....	63
<b>6. Rupture dynamics from 3D Alto Tiberina rough-fault numerical simulations.....</b>	<b>70</b>
6.1. Introduction.....	70
6.2. Rupture dynamic modeling setup .....	71
6.3. Results.....	76
6.4. Discussion and concluding remarks.....	80
<b>7. Conclusions.....</b>	<b>82</b>
<b>References</b>	<b>84</b>
<b>Acknowledgements</b>	<b>91</b>

## 1. Introduction

### 1.1. Overview of the problem

The low-angle normal faults (LANFs) are a particular class of normal faults characterized by very low dips (0-30°). Initially discovered in the Basin and Range province, US, (Anderson, 1971; Longwell, 1945; Wernicke, 1981), then they have been recognized in most other extensional tectonic setting (e.g. Collettini, 2011). Geological evidences indicate that several LANFs originated and slipped in the brittle crust as primary, gently dipping normal faults (Wernicke et al., 1985; Wernicke, 1995; Axen, 2004). Moreover large displacements are associated at these faults, which are active within a crustal stress field characterized by vertical  $\sigma_1$  trajectories (Collettini and Holdsworth, 2004; Hayman et al., 2003; John and Foster, 1993; Jolivet et al., 2010; Lister and Davis, 1989). Active LANFs are proposed in Papua New Guinea, Gulf of Corinth (Greece) and Apennines on the base of seismological data (Chiaraluce et al., 2007; Abers et al., 1997; Rietbrock et al., 1996) even if there are no strong evidences for large ( $M > 6$ ) earthquakes triggered along these structures (Jackson and White, 1989; Collettini and Sibson, 2001).

Since when the LANFs have been discovered, the scientific community debate around two principal questions: a) how can they be born in the brittle crust and b) how can they accommodate the extension. In fact, these faults are not conform to the fault mechanical theory that predicts only steep (about 60°) normal faults in the brittle crust (Anderson, 1951) and frictional lock up of existing normal faults at 30° dip (Collettini and Sibson, 2001; Sibson, 1985) considering a typical 0.7 friction coefficient (Byerlee, 1978); then, for dip less than 30°, new steep faults should form.

We tackle the second issue (b) by considering the Altotiberina fault, an active low-angle normal fault cutting the brittle crust of Northern Apennines with an average dip of  $17^\circ$ . In this work, integrating geological, seismological and geodetic data we use the finite element method to model the interseismic phase of the Alto Tiberina Fault system. At first, through 2D numerical simulations we investigate the effects of ATF locking depth, synthetic and antithetic fault activity and lithology on the deformation rates and stress build-up (Chapter 4). Then we evaluate these effects performing 3D numerical models that include a realistic geometry of the Alto Tiberina fault plane (available on the basis on seismic reflection profiles; Mirabella et al., 2011) and characterized by strong dip-angle variations (Chapter 5). Finally we discuss the rupture dynamic problem on rough faults. For this purpose, through spectral element method numerical code, we investigate the geometrical effects of a simulated earthquake on the Alto Tiberina fault in terms of maximum magnitude (Chapter 6).

## **2. The Alto Tiberina low-angle normal fault**

### 2.1. Introduction

The Alto Tiberina fault (ATF) is a 70 km long low-angle (about 17°) normal fault East-dipping in the Umbria-Marche Apennines (Central Italy) and characterized by SW-NE oriented extension and rates of 2-3 mm/yr. Striated geological fault planes (Lavecchia et al., 1994), focal mechanisms and borehole breakouts (Montone et al., 2004) define a regional active stress field with a nearly vertical  $\sigma_1$  and NE trending subhorizontal  $\sigma_3$ . In this area historical and instrumental earthquakes mainly occur on West-dipping high-angle normal faults. Within this tectonic context, the ATF has accumulated 2 km of displacement over the past 2 Ma, but the deformation processes active along this misoriented fault, as well as its mechanical behavior, are still unknown. In this chapter we present a review of the main geological and seismological aspects that outline the ATF mechanical behavior.

### 2.2. Tectonic setting

The northern Apennines consists of a NE verging thrust-fold belt formed as the result of the collision between the European continental margin (Sardinia-Corsica block) and the Adriatic lithosphere (e.g., Alvarez, 1972; Reutter et al., 1980). From the Oligocene to the present-day, the area has experienced two phases of eastward migrating deformation: an early compression with eastward directed thrusting and a later phase of extension (e.g., Elter et al., 1975; Pauselli et al., 2006). The interpretation of the seismic reflection profiles (Pialli et al., 1998) shows that a

significant amount of extension within the brittle upper crust is accommodated by a system of East dipping LANFs with associated high-angle antithetic structures (i.e. Chiaraluce et al., 2007). Older parts of the extensional system are significantly exhumed to the west in the Tyrrhenian islands (e.g., Elba) and Tuscany (Carmignani and Kligfield, 1990; Keller et al., 1994; Jolivet et al., 1998; Collettini and Holdsworth, 2004) while the ATF (Barchi et al., 1998; Boncio et al., 2000; Collettini and Barchi, 2002), which is the easternmost of these structures, is located in the inner sector of the Umbria-Marche Apennines (Figure 1) where an extensional stress field is active today.

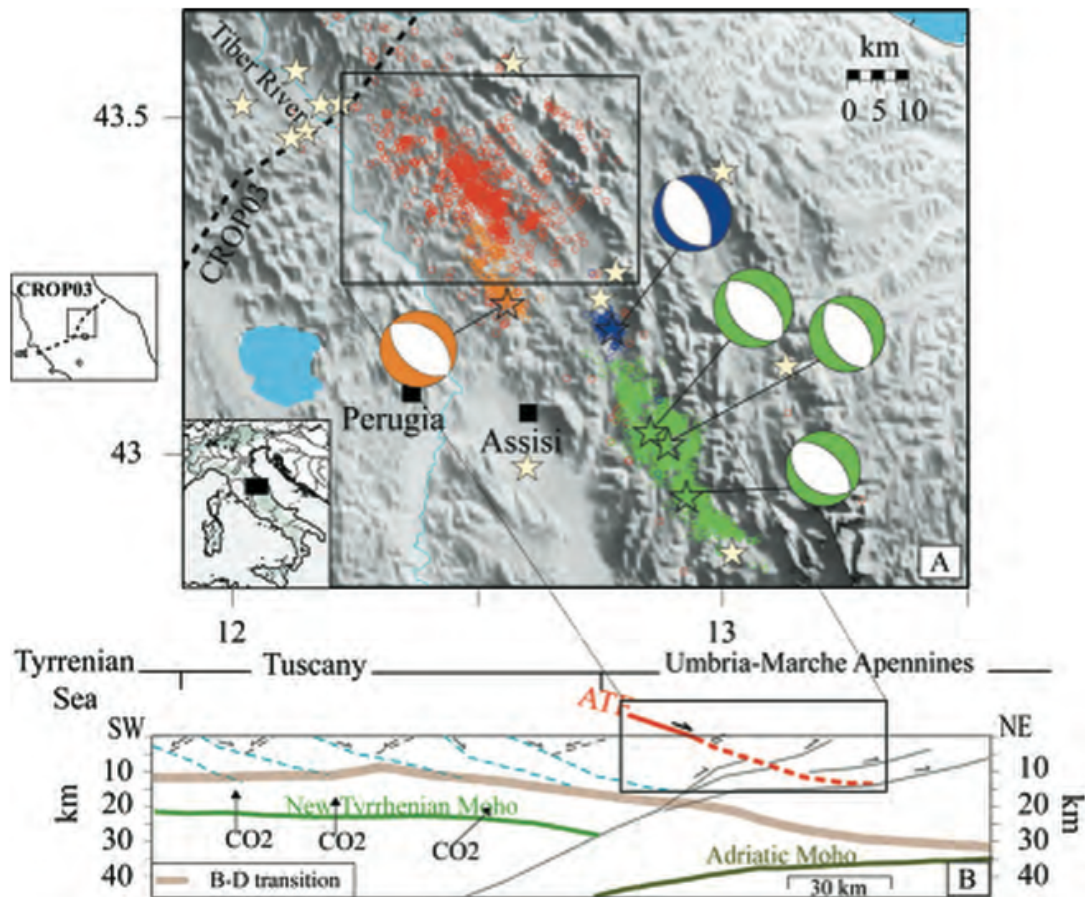


**Fig. 1.** a) Seismicity in the northern Apennines. In white stars, historical earthquakes are shown. Red symbols show the epicenters of the earthquakes recorded during the 2000–2001 seismic survey (Chiaraluce et al., 2007). Orange, blue and green symbols indicate the aftershocks of the 1984 Gubbio ( $M_w$  5.1), the 1998 Gualdo Tadino ( $M_w$  5.1) earthquakes and 1997 Colfiorito sequence respectively. b) Crustal-scale cross section interpretation of the CROP03 (courtesy of Chiaraluce et al., 2007).

### 2.3. Seismicity

At present, the active extension region is concentrated in the inner zone of the Umbria-Marche Apennines where the strongest historical and instrumental ( $5.0 < M < 6.0$ ) earthquakes are located (Figure 1). The seismicity does not follow the arc shape structures inherited from the previous compressional tectonic phase but clusters along a  $\sim 30$  km wide longitudinal zone (Chiaraluce et al., 2004; Chiarabba et al., 2005) where the historical earthquakes are also located (Figure 5a; Chiaraluce et al., 2007).

In the past 20 years, three main seismic sequences have occurred in the ATF region: the 1984 Gubbio sequence (Mw 5.1), the 1997 Colfiorito sequence (Mw 6.0, 5.7 and 5.6), and the 1998 Gualdo Tadino (Mw 5.1) sequence (Figure 5). All the mainshocks are related to SW dipping ( $\sim 40^\circ$ ) normal faults, with fault plane ruptures dipping in the opposite direction to the ATF. In this region there is an important contribute of fluid overpressure on the seismicity as interpreted for the Colfiorito sequence (Miller et al., 2004; Antonioli et al., 2005). During a temporary seismic experiment, Chiaraluce et al. (2007) recorded  $\sim 2000$  earthquakes with  $M_L = 3.1$ . The microseismicity defines a 500 to 1000 m thick fault zone that crosscuts the upper crust from 4 km down to 16 km depth. The fault coincides with the geometry and location of the ATF as derived from geological observations and interpretation of depth-converted seismic reflection profiles (Figure 2). In the ATF zone, Chiaraluce et al. (2007) also observe the presence of clusters of earthquakes occurring with relatively short time delays and rupturing the same fault patch. To explain movements on the ATF, oriented at high angles ( $\sim 75^\circ$ ) to the maximum vertical principal stress, they suggested the fault is mostly accommodated by aseismic slip in velocity

strengthening areas while microearthquakes occur in velocity weakening patches by fluid overpressures.

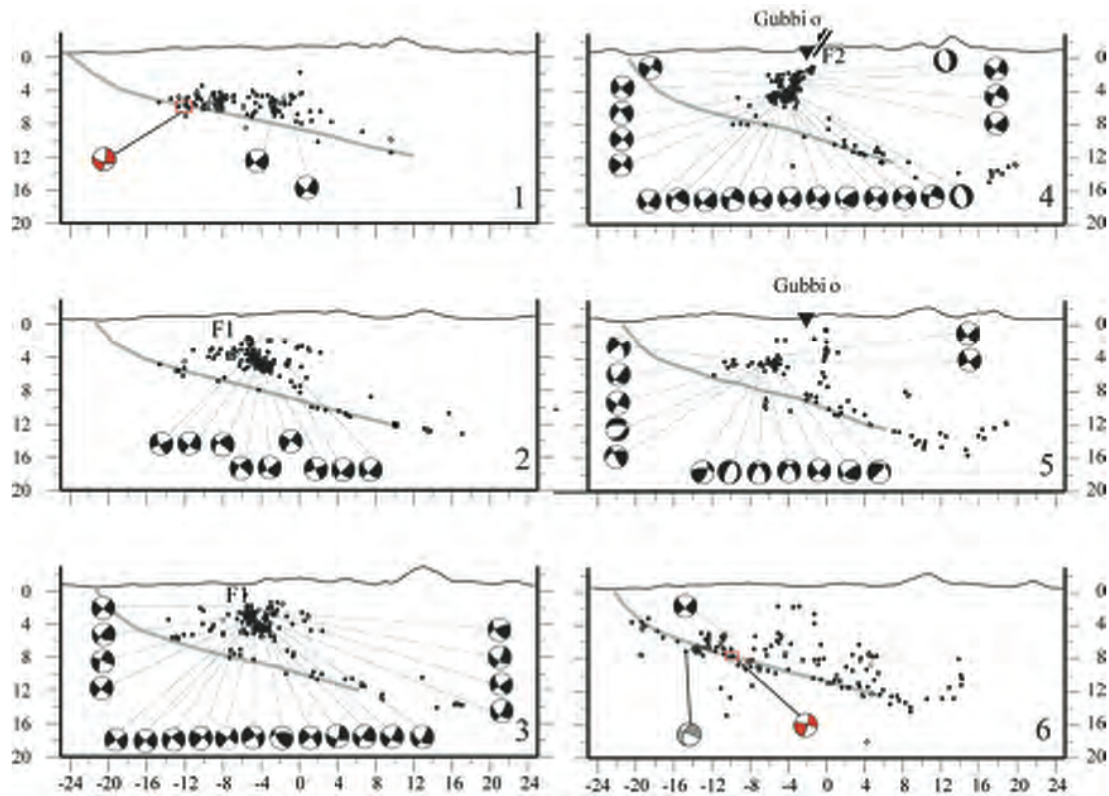


**Fig. 2.** Microseismicity location compared with the ATF plane for different cross-sections from NW to SE (courtesy of Chiaraluca et al., 2007).

#### 2.4. Long-term and short-term deformation

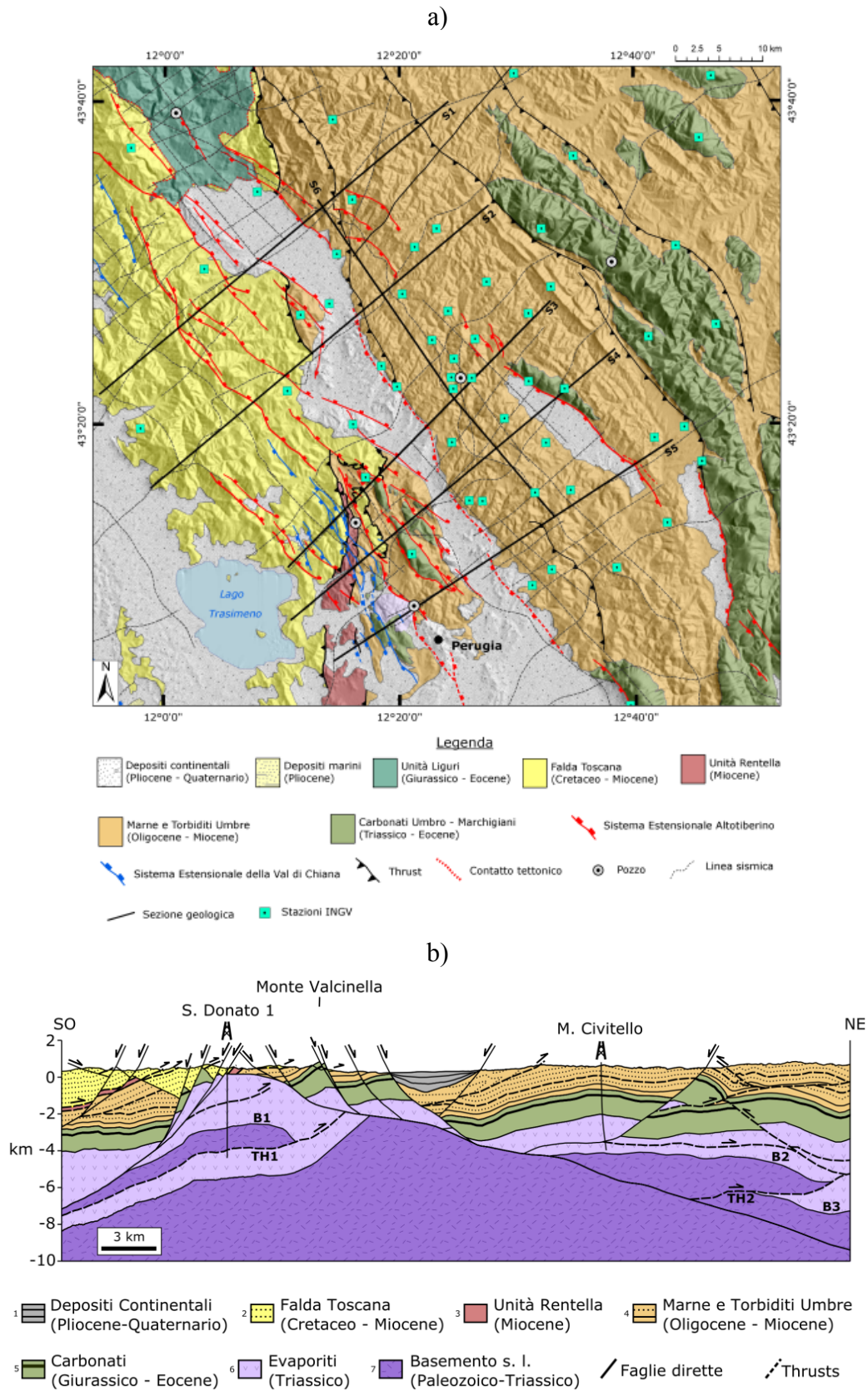
On the basis of the long-term extensional values obtained through cross-section balancing, Mirabella et al. (2011) inferred a 3 mm/yr long-term extension rate in the study area. Very similar values (2.7– 3.0 mm/yr) have been calculated through GPS measurements for the present-day extensional rate in northwestern Umbria (Figure 3; Serpelloni, personal communication). The authors interpret such convergence as evidence that extension within the study area occurs almost exclusively along the



## 2.5. Geometries

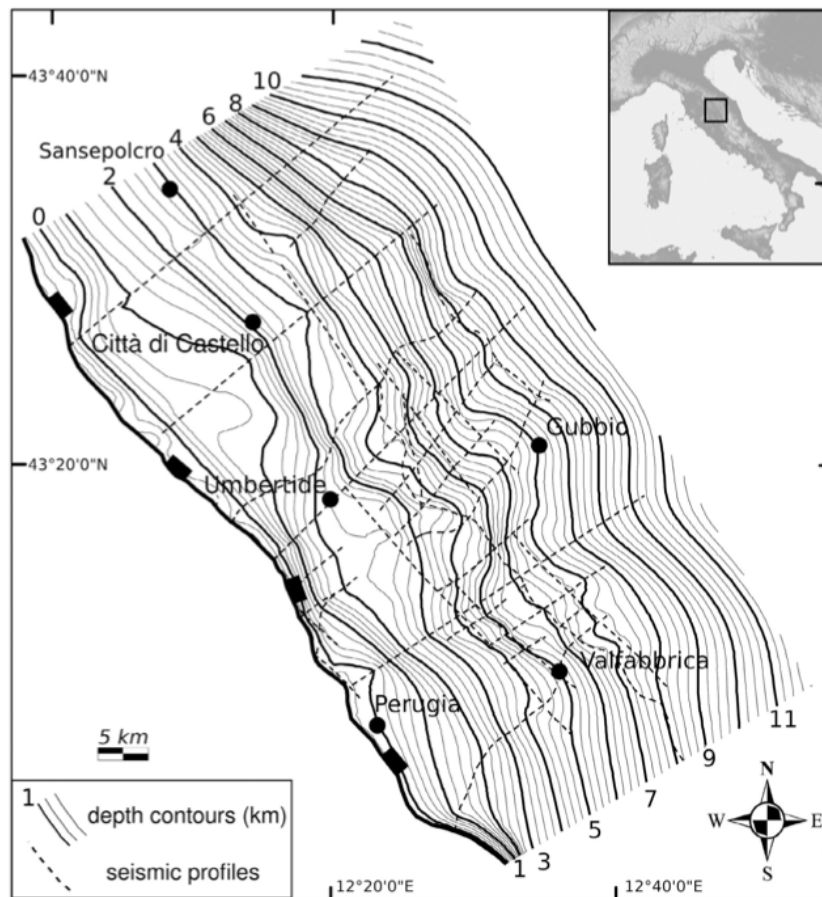
The knowledge of the fault plane geometry is a priority for interseismic and rupture dynamic modeling studies. Moreover, a good crustal velocity model is necessary to understand where local stress accumulations occur. Miller et al. (2004) through geophysical data have identified the Triassic Evaporites as the source region of the major extensional earthquakes of the Northern Apennines ( $M \sim 6$ ). For this reason, in this paragraph we analyse the structural setting where the ATF is located.

Figure 4a shows the geological map of the study area. We consider the S3 cross section (Figure 4b) for this structural analysis. From the surface to the depth four principal seismostratigraphic units are recognized (Mirabella et al., 2011): Turbidites ( $V_p = 4.00$  Km/s); Carbonatic multilayer ( $V_p = 5.50$  km/s); Evaporites ( $V_p = 6.10$  km/s) and Phyllites (or Basament s.l.;  $V_p = 5.00$  Km/s). These units have been dislocated by the activity of several synthetic and antithetic normal faults that intersect the ATF with depth. The most Eastern antithetic fault (Gubbio fault) is constituted by a typical geometry flat-ramp. This feature is associated at a pre-extensional stage of the Gubbio fault activity related to the evolution of the Miocene foredeep (Mirabella et al., 2004). Instead, the ATF is associated entirely at the last extensional phase (Mirabella et al., 2011). It is possible recognize, simply by the S3 cross-section, a staircase geometry for the ATF



**Fig. 4.** a) Geological map of the study area. b) Geological-structural cross-section cutting the inner ATF central part (courtesy of Mirabella et al., 2011)

The three-dimensional ATF fault geometry is well known by the interpretation of seismic profiles (Figure 5; Mirabella et al., 2011). Figure 6 shows the reconstruction of the ATF fault plane starting from the isobaths of Mirabella et al. 2011. Along-dip and along-strike irregularities and strong variation of the immersion slope are evident. The fault dip ranges from minimum value near to a flat plane to maximum values of  $37^\circ$  (Figure 6). This feature is very important in terms of well-orientation plane following the theory of reactivation, as discussed in the next paragraph.



**Fig. 5.** Isobath map of the ATF reflector. The thick lines are the depth contours drawn every kilometer, the thin lines are the depth contours every 250 m, the dotted lines are the sampled seismic lines from which the contours have been drawn (Mirabella et al., 2011).

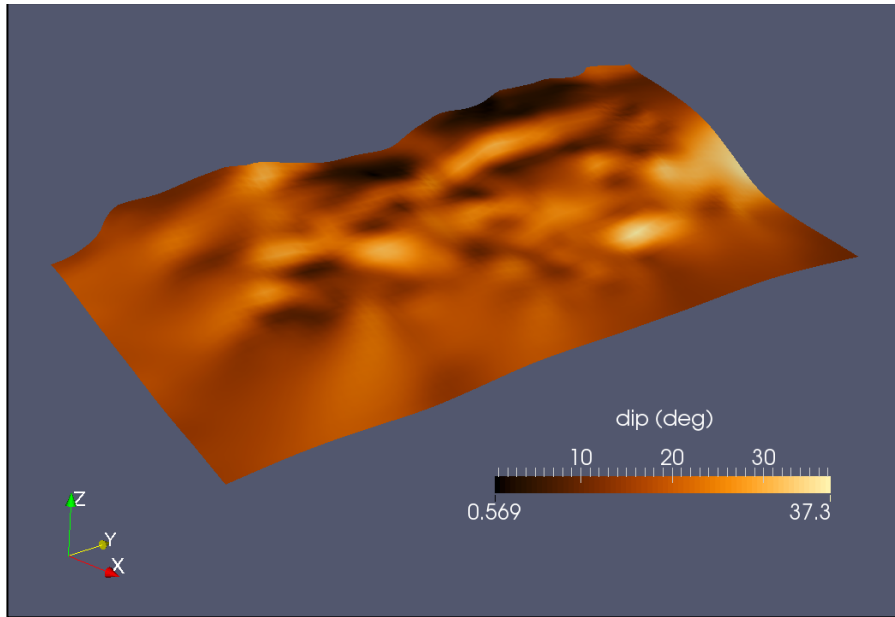


**Fig. 6.** ATF geometry obtained by the isobath map of Mirabella et al. (2011). We plot the dip distribution of the fault plane.

## 2.6. Frictional reactivation theory for normal faults

Following the analysis of Sibson (1985) and Collettini (2011) the re-shear of existing cohesionless faults with coefficient of sliding friction,  $\mu$ , can be defined by Amontons' law:

$$\tau = \mu (\sigma_n - P_f) \quad (1)$$

Then, for the two-dimensional case in which an existing fault containing the  $\sigma_2$  axis lies at a reactivation angle  $\theta_r$  to  $\sigma_1$ , Eq. (1) may be rewritten in terms of the effective principal stresses (Sibson, 1985; Collettini, 2011) as:

$$(\sigma'_1 - \sigma'_3) \sin 2\theta_r = \mu [(\sigma'_1 + \sigma'_3) - (\sigma'_1 - \sigma'_3) \cos 2\theta_r] \quad (2)$$

which reduces to

$$R = (\sigma'_1/\sigma'_3) = (1 + \mu \cot \theta_r) / (1 - \mu \cot \theta_r) \quad (3)$$

Eq. (3) defines how easy is to reactivate a fault as a function of  $\theta_r$  (Sibson, 1985). The stress ratio for reactivation  $R$  is plotted against  $\theta_r$  for the particular case of  $\mu = 0.75$  in Figure. 7.  $R$  has a minimum positive value  $R^* = (\sqrt{1 + \mu^2} + \mu)^2$  at the optimum angle for frictional reactivation given by  $\theta^* = \frac{1}{2} \tan^{-1} (1/\mu)$ , but increases to infinity for  $\theta_r = 0$  and  $\theta_r = 2\theta^*$ . For  $\mu = 0.75$ ,  $\theta^* = 26.5^\circ$  with  $R^* = 4$ . For  $\theta_r > 2\theta^*$ ,  $R < 0$  which requires  $\sigma'_3 < 0$ , therefore the effective least principal stress must be tensile (Sibson, 1985).

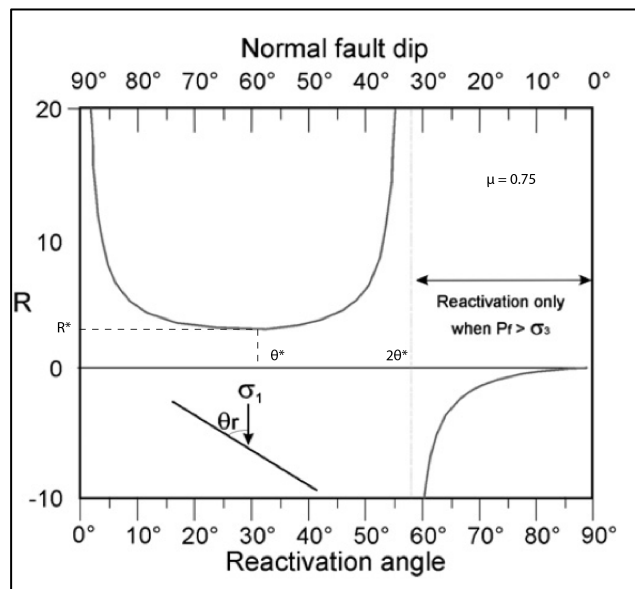


**Fig. 7.** Stress ratio,  $R$ , for frictional reactivation of a cohesionless fault plotted against the reactivation angle,  $\theta_r$ , and normal fault dip (courtesy from Collettini, 2011).

In this way, the re-shear is only possible for overpressure conditions where  $P_f > \sigma_3$ . However, the tensile overpressure condition is difficult to be maintained because hydrofractures formed when  $P_f = \sigma_3 + T$  (where  $T$  is the tensile rock strength) draining off the pressurised fluids (Collettini, 2011). For this reason particular friction conditions are necessary to reactivate a misoriented fault (e.g.  $\mu < 0.6$ ).

## 2.7. Open questions

The principal features of the ATF can be so summarized: 1) it is an active low angle normal fault dipping  $\sim 20^\circ$  in the brittle crust; 2) the fault is constituted by a finite plane larger than  $2.7 \cdot 10^3 \text{ Km}^2$  suggesting that a maximum  $M \sim 7$  earthquake could occur in case of rupture propagating along the entire fault-surface (Mirabella et al., 2011); 3) the fault roughness is characterized by strong along-dip and along-strike irregularities. All these features are not yet sufficient to delineate a precise mechanical behavior for this fault and many questions have yet to find answers. Hence first question is: what is the effect of ATF system (ATF + other faults) on the interseismic deformation? And where the maximum interseismic stress build-up is expected? Another important aspect concerning the roughness associated at the ATF since the geometrical irregularity of the fault plane can generate a strong redistribution of the interseismic stress. Even the dynamic of the rupture can be influenced by that accentuated roughness.

### **3. Numerical method**

#### 3.1. Introduction

In this Chapter, two different numerical methods to resolve the partial derivate equations (PDE) are discussed: the finite element method (FEM) and the spectral element method (SEM). The FEM will be use to resolve quasi-static problem in order to simulate the interseismic phase in Chapter 4 and 5. The SEM will be adopted to simulate dynamic ruptures of the ATF in Chapter 6. We examine the principal features of these methods and a short description of the numerical codes adopted in this thesis.

#### 3.2. Finite element method (FEM)

The FEM is a computational technique that describes the deformation state of a continuum system through the solution of PDEs at one or more variables, with a note analytic shape and defined in small regions of the continuum (Islail-Zadeh and Tackley, 2010). The method needs to discretize the system, that is to divide it in a equivalent system of a small structures (elementary components). In this way the solutions are formulated for every unit and combined to obtain the solution of the original structure. The smaller the elementary components are, the closer the system is to the continuum case, the greater the complexity of the solution becomes. Generally, it needs to research a good compromise between accuracy, numerical cost and complexity of the studied problem.

The system so defined has configured in the way that displacement and stress are continue from one element to the other, that internal stress is in equilibrium and that the boundary conditions are satisfied. In a FE analysis, we have to consider three types of fundamental relations: a) the geometrical relationship between strain and displacement, called equations of compatibility; b) the constitutive relation of the material; c) the equilibrium equation.

The approximation process requests to discretize the continuum system through different steps: the continuum media is divided in elements; the elements are connected through nodes located on the vertices (the displacements of the nodes define the incognita of the problem); we choose an interpolation criterion that defines the displacement in every point of the element as function of the displacement at the nodes; the strain is calculated from the displacement and from the strain, through the constitutive relations of the material, can be obtained the stress; the system of forces so constituted have equilibrated the internal stress and the external load applied. Every approximation during the process introduces an arbitrary degree in the solution, for this the described step should be performed with maximum cure.

### *3.2.1. Comsol Multiphysics*

Comsol Multiphysics is the software that we adopted for 2D quasi-static models of ATF. It is a commercial FEM software that consents to resolve many scientific problems with a multiphysics approach, through the coupling of different physics described by a system of PDEs. The code provides the possibility to define geometries, physics parameters, material properties, loads and boundary conditions.

In Comsol, it is also possible to define equations ad hoc used by the code in combination of the PDEs to resolve specific problems. The package can be used by a graphic interface that permits to operate in all modelling phases in simple way, starting to build the geometry directly in the code or importing it from other CAD software. The geometry is discretized by triangular or quadrilateral elements.

### 3.2.2. *PyLith*

PyLith (Aagaard et al., 2013) is the numerical code adopted for 3D quasi-static simulation of ATF interseismic phase. PyLith is open source, ad-hoc designed for 3-D dynamic and quasistatic simulations of crustal deformation, primarily earthquake and volcanoes. PyLith is one component in the process of investigating tectonic problems (Figure 8). Given a geological problem of interest, it need first provide a geometrical representation of the desired structure. Once the structure has been defined, a computational mesh must be created. PyLith provides three mesh importing options: CUBIT Exodus format, LaGriT GMV and Pset files, and PyLith mesh ASCII format. Present output consists of VTK or HDF5/Xdmf files which can be used by a number of visualization codes (e.g., ParaView, Visit, MayaVi, and Matlab).

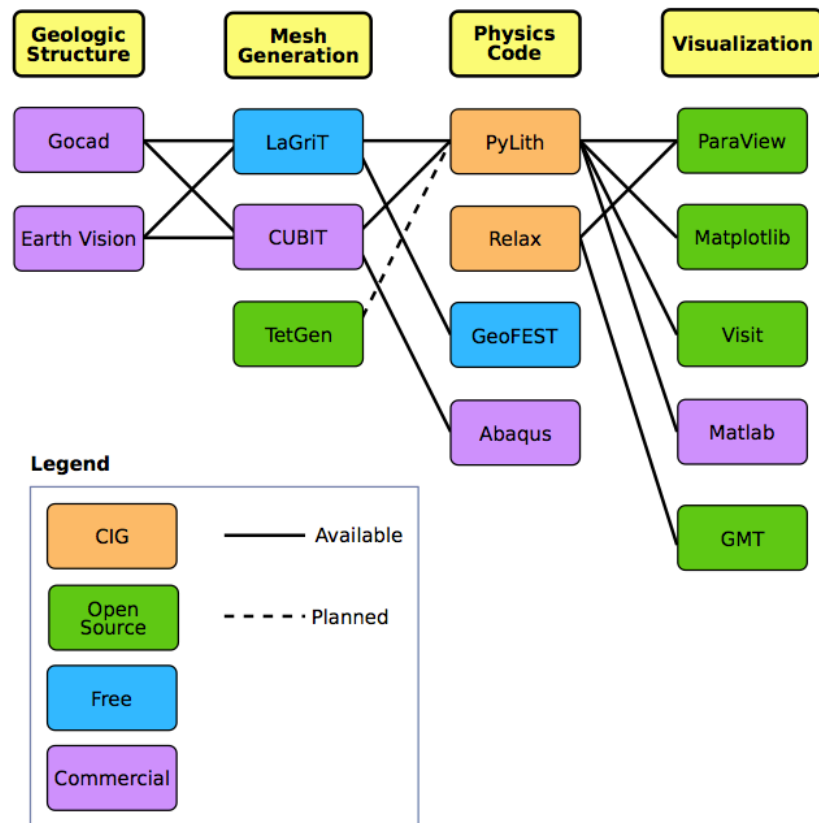


**Fig. 8.** Workflow involved in going from geologic structure to problem analysis (courtesy of Aagaard et al., 2013).

### 3.3. Spectral element method (SEM)

Spectral element method (SEM) is a high-order accurate and flexible method originally introduced in computational fluid dynamics (Patera, 1984) and after has been successfully applied in seismic wave propagation (Komatitsch et al, 2005; Chaljub et al, 2007). Recently this method is finding new perspectives in the earthquake dynamic too (Kaneko et al., 2008; Ampuero, 2009; Galvez et al., 2013). The main features of this method can be so summarized: 1) In contrast to many numerical methods, such as finite-difference and pseudospectral methods that are based upon a strong formulation of the problem (they work directly with the equation of motion) SEM (like FEM) is based upon the weak formulation of wave or integral

equation. 2) Simulation volumes are discretized using a grid (mesh) of hexahedral elements. This mesh can honour any discontinuity in the model and can be fully unstructured (i.e., the number of elements that share a given point can vary and take any value), thus very complex geometries and any arbitrary shaped domain can be accommodated. Using hexahedral elements leads to several benefits, such as optimized tensor products, a diagonal mass matrix and a smaller number of elements compared to tetrahedral meshing (Peter et al., 2011). Mechanical properties can vary inside each element, allowing fully heterogeneous media to be implemented. 3) SEM uses high-degree (between 4 and 10) Lagrange polynomials as basis functions. This ensures a very high spatial accuracy and an exponential decreasing of errors typical of spectral and pseudo-spectral methods. 4) Very efficient implementation on parallel computers with distributed memory. This tremendously reduces the computational costs, making SEM suitable to be used for large, high-resolution simulations on very powerful machines.

### *3.3.1. SPECFEM3D*

In this work, to resolve the problem of the ATF dynamic rupture, we use SPECFEM3D, an open source code that uses the spectral element method and built ad hoc to resolve wave propagations and earthquake dynamic problems. The code finds application in highly complex 3D heterogeneous media. The workflow consists in different step-by-step operations as shown in figure 9. Starting from a detail geological and tomographic model the first crucial step is the meshing. The mesh in SPECFEM3D can be built in three different ways. The first option is using meshfem3D, a tool included in the code. It allows to design relatively simple mesh for

layercake models, using an analytical linear interpolation from the top to the bottom of the mesh (Peter et al., 2011).

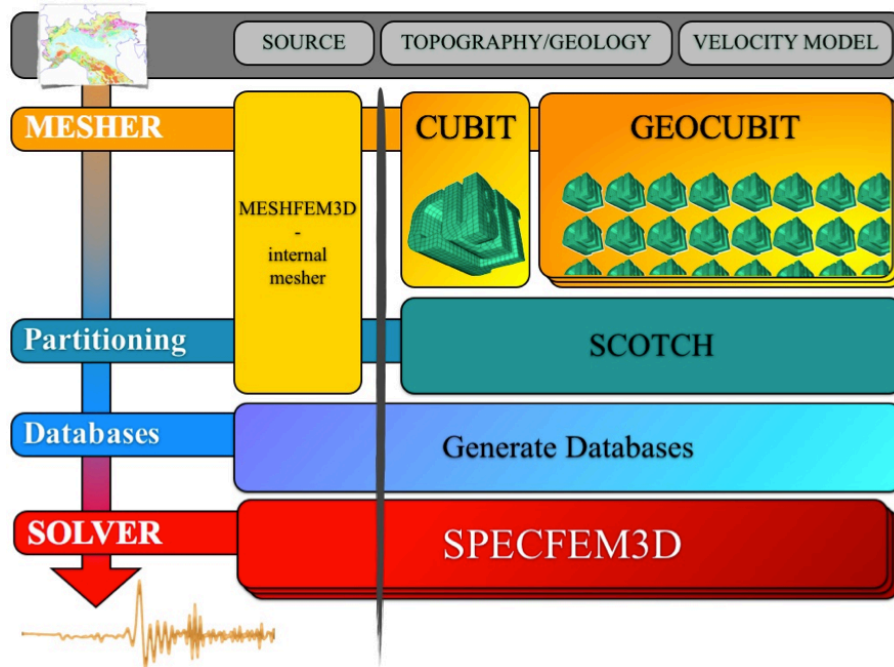


**Fig. 9.** Workflow for running spectral-element simulations with SPEC3D. The gray box on top contains the input elements for the code (courtesy of Magnoni, 2012).

For complex geometries, in particular in presence of strong discontinuity like faults, is possible to use CUBIT (Blacker et al., 1994) an external 3D unstructured mesh generator. The third possibility is using GEOCUBIT, a Python script collection based upon CUBIT (Casarotti et al., 2008). After that the mesh is built, it came partitioned in different slices through a software packages SCOTCH (Pellegrini and Roman, 1996). Every slice will be distributed for every core on the cluster (Fig. 10). After meshing and partitioning is possible to generate a database to assign the material and fault property. The last input to run the simulations are the definition of the location of receivers. At the end, the spectral-element solver performs a numerical integration of the wave equation, simulating the synthetic waveforms for each of the considered stations.

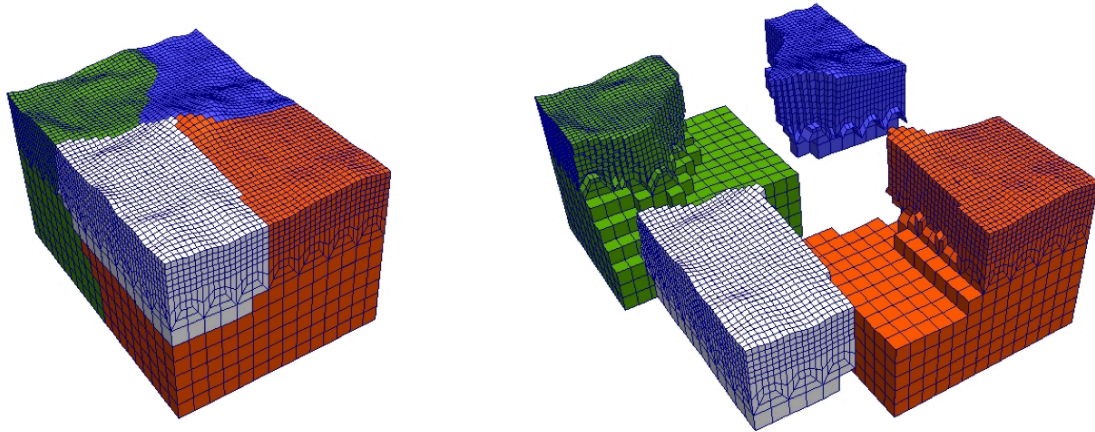


**Fig. 10.** Mesh partitioned using SCOTCH to run in parallel on four cores. The four partitions are indicated by different colors (courtesy of Peter et al., 2011).

### 3.4. Fault implementation

In order to create relative motion across the fault surface in the finite-element mesh, two different methods are used in Comsol and PyLith codes (Fig.11a-b). In Comsol the fault is defined as a contact pairs. These pairs define boundaries where the parts may come into contact but cannot penetrate each other under deformation. The frictional constitutive law is defined along this contact surface.

The boundaries where the fault is defined are splitted apriori before that the mesh is built. In this way the contact is constituted by different nodes with different index and are bound together by the cohesion forces (Fig. 11a). The boundaries of the contact pairs are called master and slave. For definition the slave cannot penetrate in the master boundary. In this way in order to facilitate the convergence is preferably that the slave identifies the hangingwall and the master boundary the footwall of the fault. This is because when, in the interseismic model, a gravity load is applied the slave is

the boundary from which the pressure comes and the master is the boundary that undergoes the pressure.

Differently, in PyLith additional degrees of freedom are added along with adjustment of the topology of the mesh. These additional degrees of freedom are associated with cohesive cells. These zero-volume cells allow control of the relative motion between vertices on the two sides of the fault. PyLith automatically adds cohesive cells for each fault surface. Figure 11b illustrates the results of inserting a cohesive cell in a mesh consisting of two quadrilateral cells. The great advantage of PyLith respect to Comsol is that different friction constitutive law are already implemented in the code. In SPEC3D, as in Comsol, the fault is implemented splitting the surface, directly in the mesher (Day et al., 2005, Galvez et al., 2013)

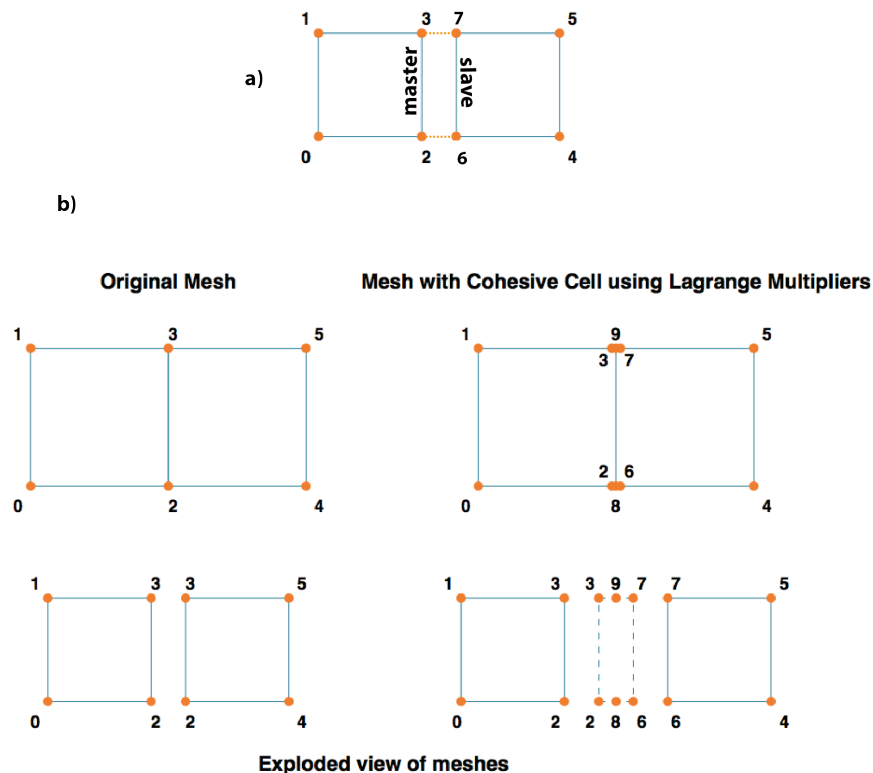


**Fig. 11.** Example of fault implementation for quadrilateral cells. a) In Comsol the nodes are splitted apriori; (b) in PyLith a cohesive cell is inserted into a mesh. The zero thickness cohesive cell (shown with dashed lines) controls slip on the fault via the relative motion between vertices 3 and 7 and 2 and 6 (like in the Comsol code, after Aagaard et al., 2013).

## **4. Modelling the interseismic deformation of the Alto Tiberina fault system by 2D numerical simulations: locking depth, fault activity and effects of lithology**

### 4.1. Introduction

A critical issue of active low-angle normal faults (LANFs) is the identification of their mechanical behaviour. In fact, being misoriented faults with principal stress axis  $\sigma_1$ , the large displacement and the lack of large earthquakes associated at these structures could be explained with a stable sliding behavior (Collettini, 2011). We take this issues considering the study case of the Alto Tiberina fault a very low-angle normal fault dipping  $\approx 17^\circ$  in the Northern Apennines (Figure 1). There are different ways to understand the mechanics behaviour of an active fault. These can be divided in inverse and direct methods. For example, geodetic inversions (e.g. Tong et al., 2013; Rolandone et al., 2008) and repeating earthquake localization (e.g. Turner et al., 2013) have been successfully used to define the creeping portion of the San Andreas Fault (another well known misoriented fault but in strike-slip regime). Friction laboratory experiments (direct methods) on rock samples of San Andreas Fault zone have confirmed those hypotheses (e.g. Carpenter et al., 2011).

Concerning the Alto Tiberina fault, Chiaraluce et al., (2007), during a temporary seismic experiment, have observed the presence of clusters of earthquakes occurring with relatively short time delays and rupturing the same Alto Tiberina Fault patches. They hypothesized a velocity strengthening rheology for the ATF zone with same fault patches with velocity weakening behaviour; moreover friction laboratory experiments on fault zone rocks of the Zuccale low angle normal fault, the natural

analogue of the ATF, showed a prevalent velocity strengthening rheology of the fault (Smith and Faulkner, 2010; Collettini et al; 2009).

In this Chapter, we show the results of 2D numerical mechanical models of the interseismic phase of the ATF system, constrained by geological, seismological and geodetic information. In particular we are going to analyse the following aspects: a) the ATF locking depth, b) the influence of the synthetic and antithetic faults activity and c) the influence of the lithology on the stress distribution and on the interseismic deformation rates.

#### 4.2. Modelling description

We performed 2D finite element mechanical simulations with plain strain approximation by means of the commercial software COMSOL Multiphysics (<http://www.comsol.com/>). We used a NE-SW regional cross-section cutting the central part of the ATF as base of the models (Figure 12 and 4) and considered only the faults associated at the ATF system defined by Mirabella et al. (2011). The mesh consists of approximately 270.000 triangular elements with a finest resolution of 25 m near the faults and decreases to 2000 m along the boundaries (Figure 19).



In this way, the model compacts under the weight of the rocks and is brought in a stable equilibrium with gravity. In this first step, the boundary conditions, applied to all models, are the following: (a) the upper part of the models is free to move in all directions, (b) the SW and NE lateral boundaries of the crust and the bottom of the model are kept fixed in the direction perpendicular to these boundaries (slip parallel to these boundaries is allowed, Figure 13a). In the second stage (interseismic phase) we stretched the crust for 1000 years, applying a constant horizontal velocity of 0.5 mm/yr and 3.5 mm/yr on the SW and NE lateral boundaries respectively (Figure 13b) in according to the present-day plate kinematics of the Northern Apennines region (Hreinsdottir and Bennett, 2009; Serpelloni, p.c.). All the remaining boundary conditions are maintained.

The stress field resulting from the first stage is defined as uniaxial strain reference frame (Engelder, 1993). This state of stress is characterized by vertical stress  $S_v = \rho g y$  (where  $\rho$  is the density,  $g$  is the gravity acceleration and  $y$  is the depth) and horizontal stress  $S_h = S_H = (\nu/(1 - \nu)) * S_v$ , where  $\nu$  is the Poisson's ratio. In this way for  $\nu = 0.25$ , the vertical stress is three times larger than the horizontal stress. If the obtained orientations of the stress axis are compatibles with those of the study area (Chiaraluce et al., 2007; Montone et al., 2004), the magnitude can be certainly away from reality. Because no constrain by stress measurements (e.g. leak off tests; Engelder, 1993) is available, a stress reference state is necessary. For this reason, the stress obtained during the second stage (extension phase) is not significative in absolute terms. Consequently, during the discussions of the results, we will consider only the tectonic stress, equal to the difference between the stress at end of the simulation and the stress obtained after the application of gravity.

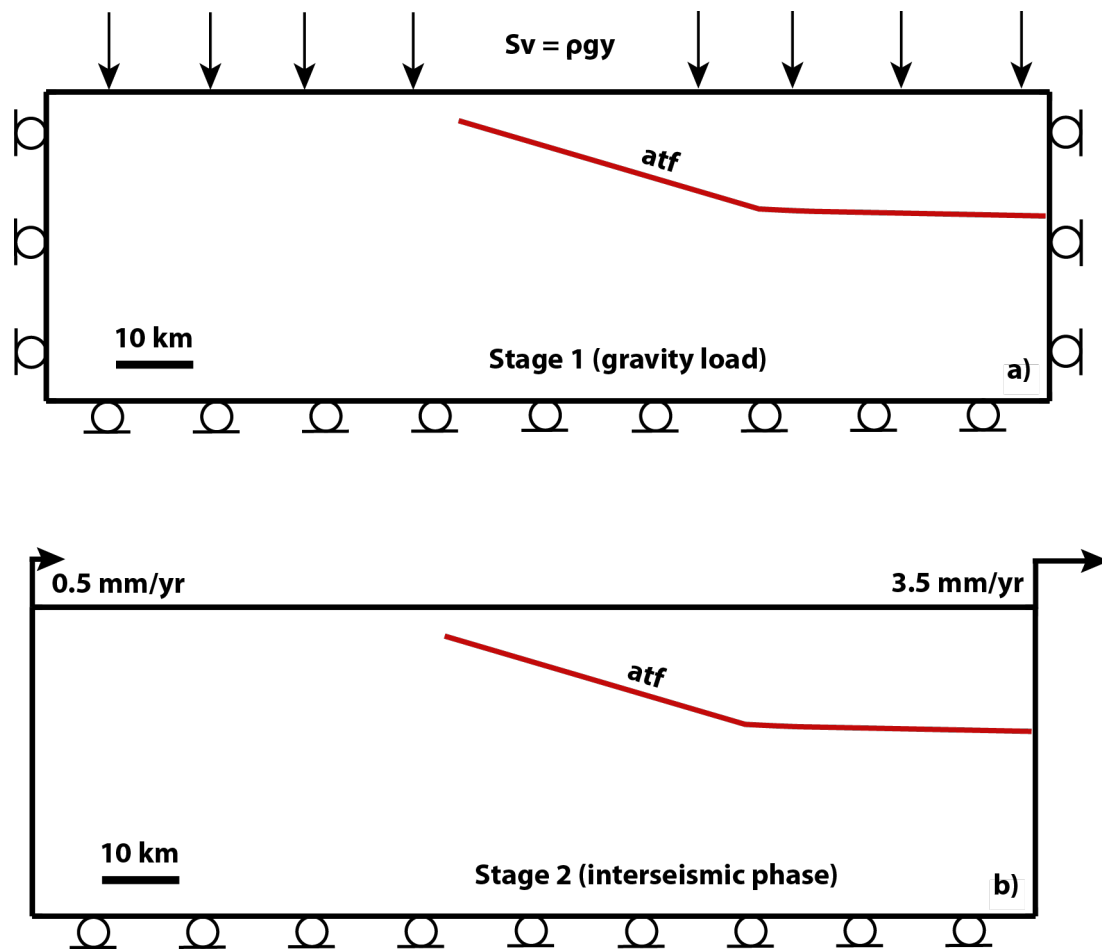


**Fig. 13.** Boundary conditions for a generic model. a) During the stage1 a gravity load is applied. b) During the stage 2, the crust is stretched applying a constant horizontal velocity of 0.5 mm/yr and 3.5 mm/yr on the SW and NE lateral boundaries. Note that these boundary conditions are the same for all models considered in this work.

In all models the faults are defined as 100 m thick shear zone. The weakness of the synthetic and antithetic shear zones is defined considering a Young modulus value of 100 MPa (two order of magnitude lower then the intact rocks; Tab. 2; Pasuselli and Federico, 2003), consistently with the typical Young's moduli of unconsolidated rocks, as well as in situ measurements from various fault cores worldwide (Hoek, 2000; Schon, 2004; Gudmundsson, 2011). In this way when we will consider that these faults are active, it will means that they will have a Young modulus of 100 MPa (Tab. 2). Otherwise when inactive, the faults will have a Young modulus equal to that of the intact rocks (Tab. 2). This assumption is in according to different geological

evidences. In fact during the evolution of an active seismogenic fault, the Young modulus in the damage zone decreases due to the formation of new fractures. The same effect is obtained by the formation of gouge during earthquake rupture (e.g. Reches and Dewers, 2005). These factors reduce the effective Young modulus of the fault zone. By contrast, for an inactive fault, the effective Young modulus of the core and damage zone may increase because of healing and sealing of the associated fault rocks and fractures (e.g. Gudmundsson, 2004).

Otherwise, in order to simulate a free-slip motion along the ATF we consider a very compliant ATF zone with Young modulus value of 10 MPa. We have probed that a so-defined compliant fault zone has the same effects on the deformation rates respect to free-slip motion simulated along a contact with friction near to zero (Figure 14 and 15). The boundary conditions for this test are the same of figure 13 and the mechanical properties are listed in Table 1. Moreover we have assumed that the compliant fault zone and the free-slip contact are active below 5 km of depth (Figure 14). This method to simulate the ATF free-slip motion has the great advantage to reduce the computational costs and convergence problems respect to fault frictional contacts method. For this reason in all models we approximate the free-slip behaviour of the ATF as a compliant fault zone. We remark that in the following models the ATF is always active as a free-slip fault below the prescribed locking depth; above that the ATF is inactive (i.e. the Young modulus of the fault zone is equal to that of the intact rock, Tab. 2).

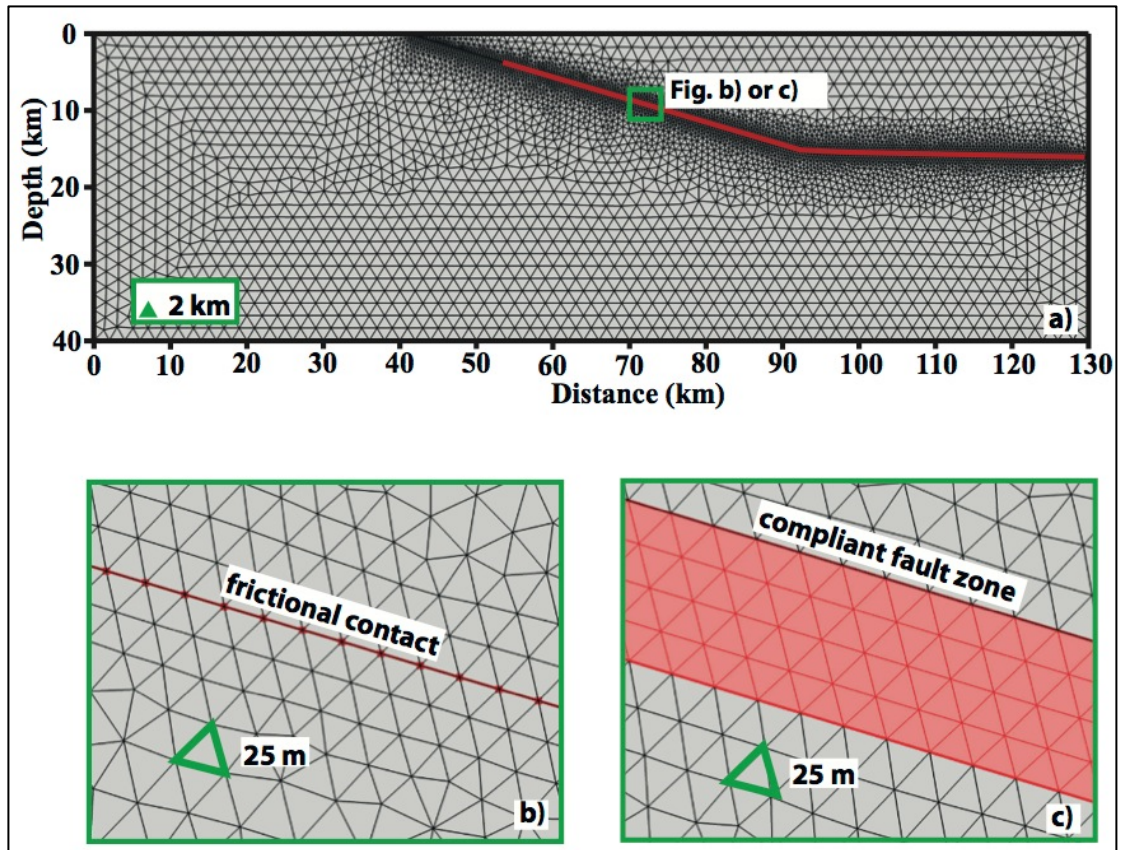


**Fig. 14.** a) Mesh used to test the frictional contact model (FC) b) and compliant fault zone model (CFZ) c). The results are shown in figure 15. Note that the dimensions of the triangular mesh are maintained the same for both the models.

	Intact rock			ATF fault zone			ATF fault	
	Young modulus (Pa)	Poisson's ratio	Density (Kg/m <sup>3</sup> )	Young modulus (Pa)	Poisson's ratio	Density (Kg/m <sup>3</sup> )	Friction coefficient	Cohesion (Pa)
FC model	5.33e10	0.25	2570	-	-	-	≈ 0	0
CFZ model	5.33e10	0.25	2570	1e7	0.35	2500	-	-

**Tab. 1.** Mechanical properties used for FC and CFZ models (Figure 14-15) to test the effects of the free-slip behaviour simulated via a fault frictional contact and a compliant fault zone. A Coulomb failure criterion is used for FC model.

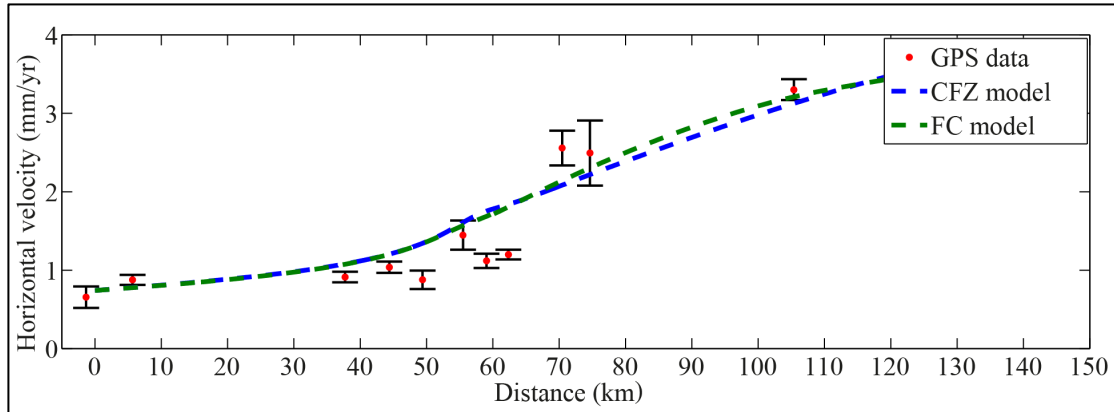


**Fig. 15.** a) Horizontal velocity for the CFZ and FC models characterized by a different approximation of the free-slip behaviour. The boundary conditions are the same of figure 13. Note that the horizontal component of the velocity is very similar for both the models.

Three different model settings are considered. First, we focus on the ATF locking depth and we consider four characteristic depths whence the ATF was in free-slip (2 km, 5 km, 8 km, 11 km; ATF models; Figure 16). The effects of the other faults are neglected. Moreover, to understand the only effects of the ATF locking depth, uniform elastic parameters for the crust are adopted (Table 2).

In the second set of models, we consider the influence of the activity of synthetic and antithetic faults on the interseismic deformation. We assume different configurations for every ATF locking depth previously considered: ATF2, ATF5, ATF8 and ATF11 models (Figure 17). Initially we consider that all the synthetic and antithetic faults are active (e.g. ATF2-a; Figure 17). Successively we consider inactive these faults (one-by-one from west to east, e.g. ATF2-b-d; Figure 17). In the last model, only the antithetic Gubbio fault is active (e.g. ATF2-e; Figure 17). This set-up allows us to understand what faults is mainly accommodated the deformation. In these models, uniform elastic parameters for the crust are adopted (Table 3).

Finally, we consider the effects of the lithology on the interseismic stress build-up and deformation rates (ATF5-e-litho model, Figure 18). We consider only the principal

layers, representing lithological units characterized by similar competence (Pauselli and Federico, 2003; Mirabella et al., 2011; Table 4). In this model we assume that the Gubbio fault is active together with the ATF (that is instead free-slip).

We maintain the same boundary conditions for the three different model settings as shown in figure 13.

	Young modulus (Pa)	Poissons ratio	Density (Kg/m <sup>3</sup> )
Intact rock	5.33e10	0.25	2570
ATF fault zone (active)	1e7	0.35	2500
ATF or synthetic and antithetic fault zones (inactive)	5.33e10	0.25	2570

**Tab. 2.** Mechanical properties used for ATF models (Figure 16) to test the effects of the ATF locking depth.

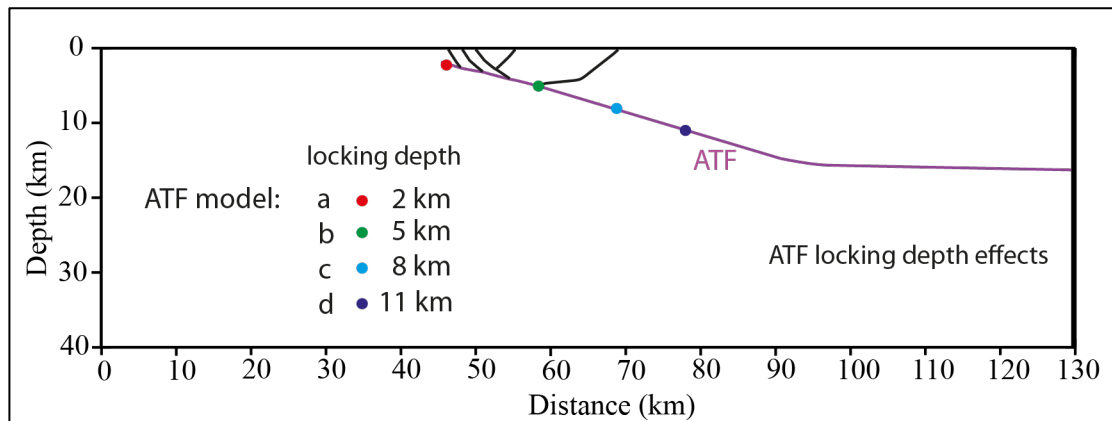


**Figure 16.** ATF model set-up. In this configuration setting we explore the effects of the ATF locking depth. We build four models for different ATF locking depth: ATFa (2km), ATFb (5 km), ATFc (8 km) and ATFd (11 km). Above the locking depth the ATF is inactive (see text). No effects of other faults are considered in these models. The crust is homogeneous (Tab. 2).

	Young modulus (Pa)	Poissons ratio	Density (Kg/m <sup>3</sup> )
Intact rock	5.33e10	0.25	2570
ATF fault zone (active)	1e7	0.35	2500
Synthetic and antithetic fault zone (active)	1e8	0.35	2500
ATF or synthetic and antithetic fault zones (inactive)	5.33e10	0.25	2570

**Tab. 3.** Mechanical properties used for ATF2, ATF5, ATF8 and ATF11 models (Figure 17) to test the effects of synthetic and antithetic fault activity for different ATF locking depth.

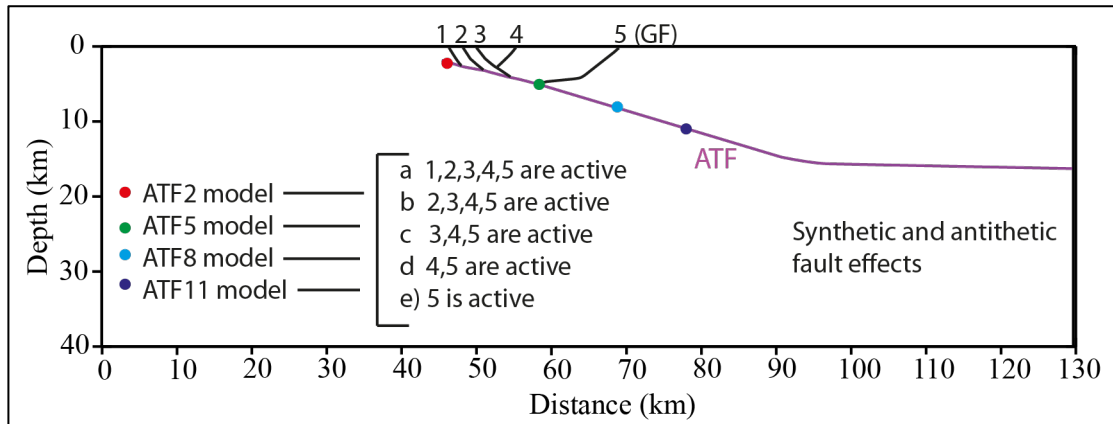


**Figure 17.** ATF2, ATF5, ATF8 and ATF11 model set-up. In this configuration setting we explore the effects of the synthetic and antithetic fault activity for different ATF locking depth (2 km, 5 km, 8 km and 11 km). In this way for every ATF locking depth we build five different configurations depending on the synthetic and antithetic fault that are active. In ATF\_a model all the faults are active. In ATF\_b model configuration the faults 2, 3, 4 and 5 are active. In the ATF\_c model the faults 3,4 and 5 are active. Then in the ATF\_d model only the antithetic faults 4 and 5 are active. Finally in ATF\_e model only the Gubbio fault (5 or GF) is active. The symbol \_ corresponds to 2, 5, 8 and 11 depending on the ATF locking depth considered. Above the locking depth the ATF is inactive. The crust is homogeneous (Tab. 3).

	Young modulus (Pa)	Poissons ratio	Density (Kg/m <sup>3</sup> )
Turbidites	3.17e10	0.25	2390
Carbonates	6.68e10	0.25	2660
Evaporites	8.65e10	0.25	2800
Pyllites	5.33e10	0.25	2570
Basament	9.21e10	0.25	2840
ATF fault zone (active)	1e7	0.35	2500
GF fault zone (active)	1e8	0.35	2500
ATF or synthetic and antithetic fault zones (inactive)	*	*	*

**Tab. 4.** Mechanical properties used for ATF5-e-litho model (Figure 18) to test the effects of the lithology considering only the antithetic Gubbio fault active and for ATF locking depth of 5 km. (\*) Note that in this model the inactive fault zones are defined with different elastic parameter values depending of the lithology that the fault intersects (e.g. if one inactive fault zone intersect the Turbidites, then it will have the same elastic parameters of the Turbidites; and so on).

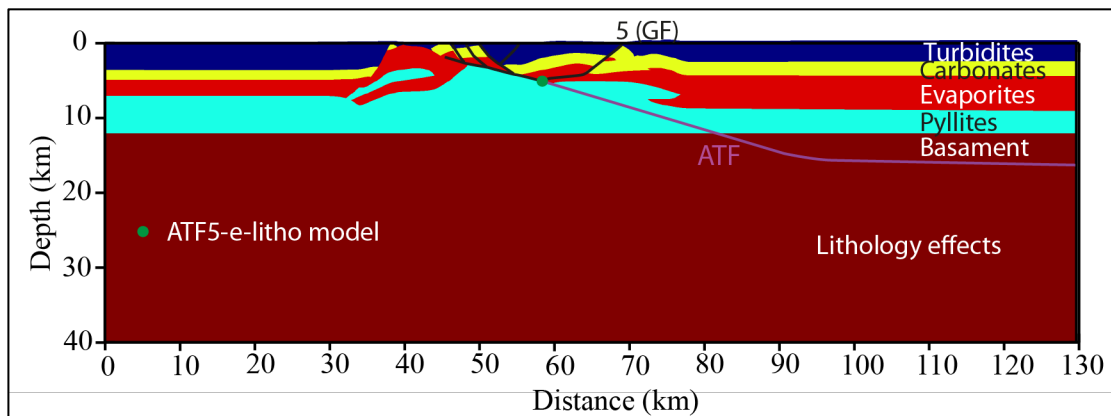


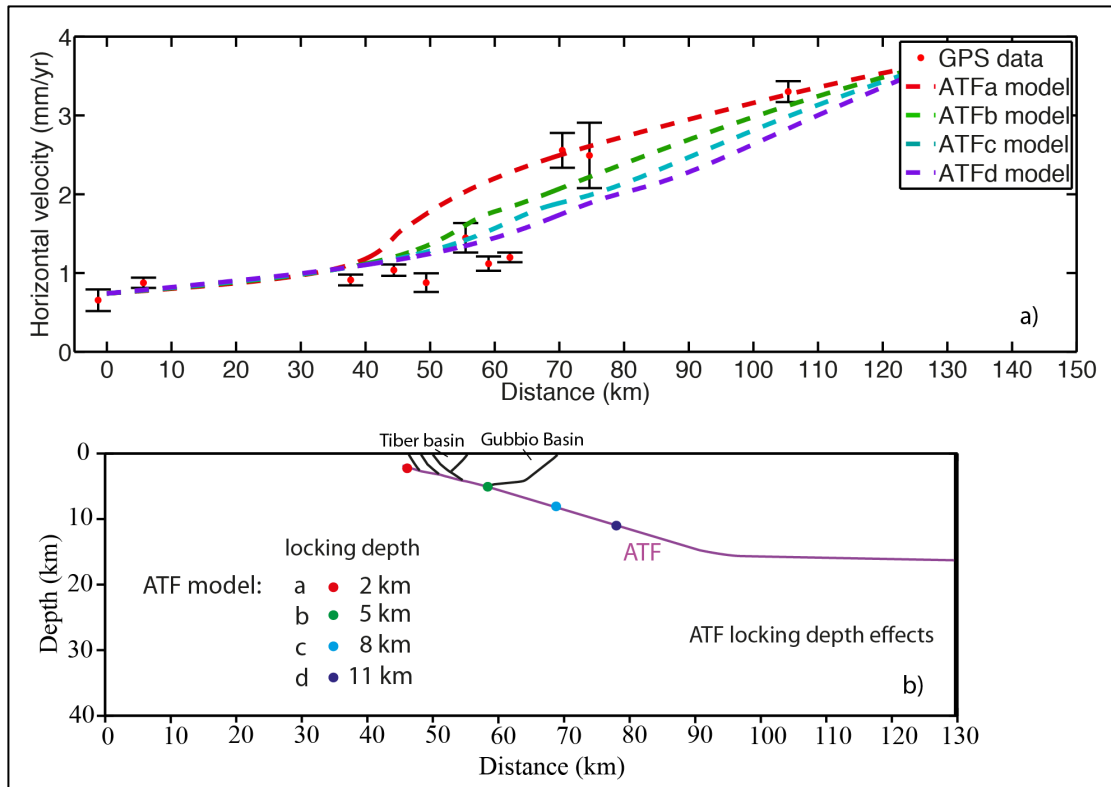
**Fig. 18.** ATF-e-litho model set-up. In this model we explore the effects of the lithology. We consider five main layers: Turbidites, Carbonates, Evaporites, Pyllites and Basament. The mechanical properties for every layers are shown in table 4. In this model we consider one ATF locking depth of 5 km and that only the Gubbio fault is active.

### 4.3. Model results

For each set of models we compare the horizontal velocity obtained by the different configurations with the GPS velocity measured during 10 years (Figure 12). We use 11 GPS stations whose distance from the cross-section is less than 10 km (from SW to NE they are: SIO1, REPI, CSSB, VALC, UMBE, ATLO, MVAL, PIET, ATFO, ATBU, FOSS; Figure 12). Then, we evaluate the Von Mises stress, in order to quantify the interseismic stress build-up and have indication of shear stress.

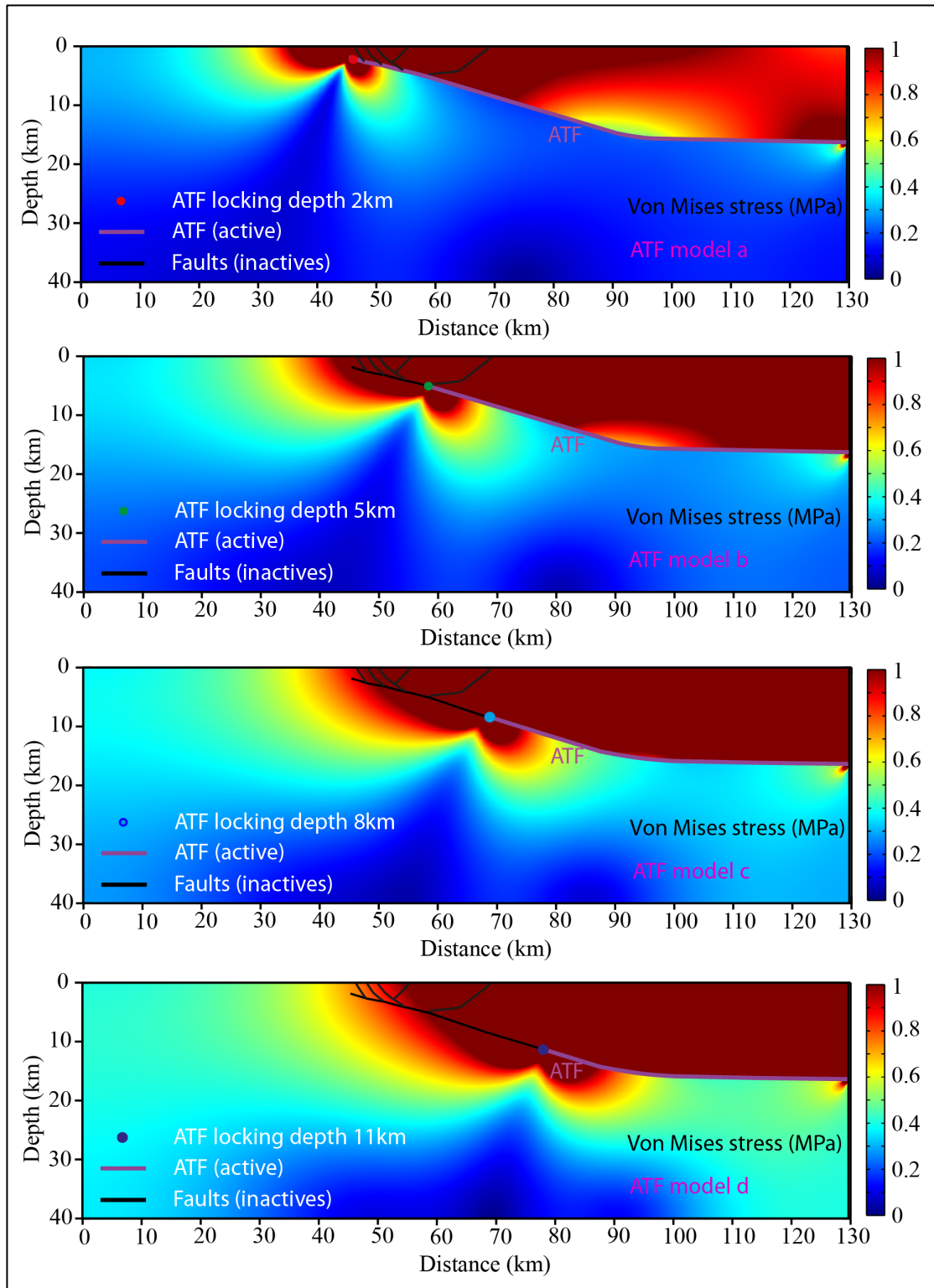
#### *4.3.1. ATF locking depth effects*

Figure 19 shows the horizontal velocity field inferred from GPS data and numerical simulations for different ATF locking depth. The GPS data show an increase of the horizontal velocity from the High Tiber basin to the Gubbio basin (Figure 19). In this way the strain is localized in a 20 km wide area between two crustal blocks with rigid behavior (to SW and to NE, Figure 19). By comparing the results for the different locking depth we note that the best fitting was obtained for a 5 Km locking depth (see Table 5). Indeed, for a locking depth of 8 and 11 km, we observe that the horizontal velocities are underestimated respect to the GPS data. Nevertheless, for shallow locking depth (2 km), the horizontal velocities are overestimated.



**Fig. 19.** a) Horizontal velocity for ATF model considering different ATF locking depth (2km, 5km, 8 km, 11 km). The mechanical property values for these models are shown in Table 2. The effects of other faults are neglected and an homogeneous crust is considered. Note the strain is mainly located in a 20 km wide area from the Tiber basin to the Gubbio basin (shown in b). The best fit is obtained for ATFb model (see Table 5).

Figure 20 shows the interseismic stress build-up after 1000 years and for different ATF locking depth. We can observe that high values of stress are localized near the tip point of the ATF generated by the free-slip along the fault. Moreover, for all different locking depth, we can recognize two prevalent areas at different stress magnitude: one localized in hanging-wall of the ATF with high values of stress, and another one situated in the footwall with lower values of stress.



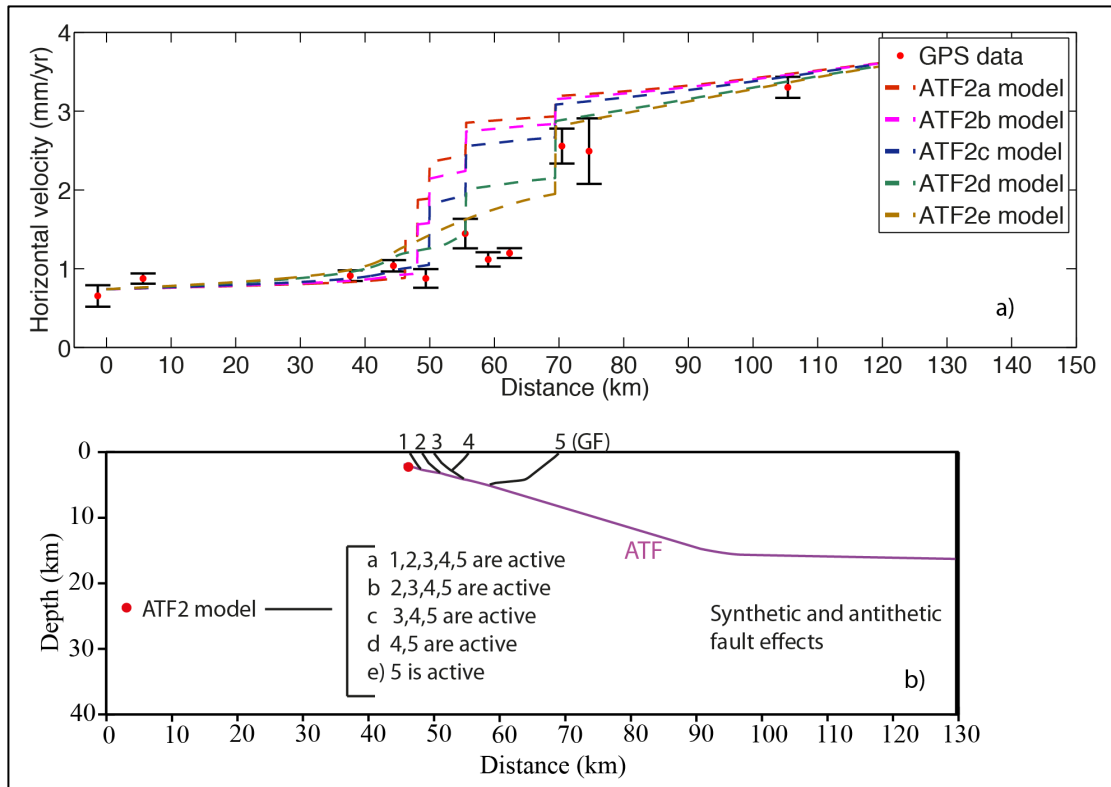
**Fig. 20.** Interseismic stress build-up for ATF models considering different ATF locking depth (2 km, 5 km, 8 km and 11 km). The effects of other faults are neglected and an homogeneous crust is considered. Note that the only effect of the ATF locking depth generates a bipartition of stress concentration between hanging wall and footwall.

These models emphasize the main role of the ATF to accommodate the extension in this region. Nevertheless, the free-slip motion of this structure is not sufficient to explain the GPS data and the contribute of other faults could be so relevant.

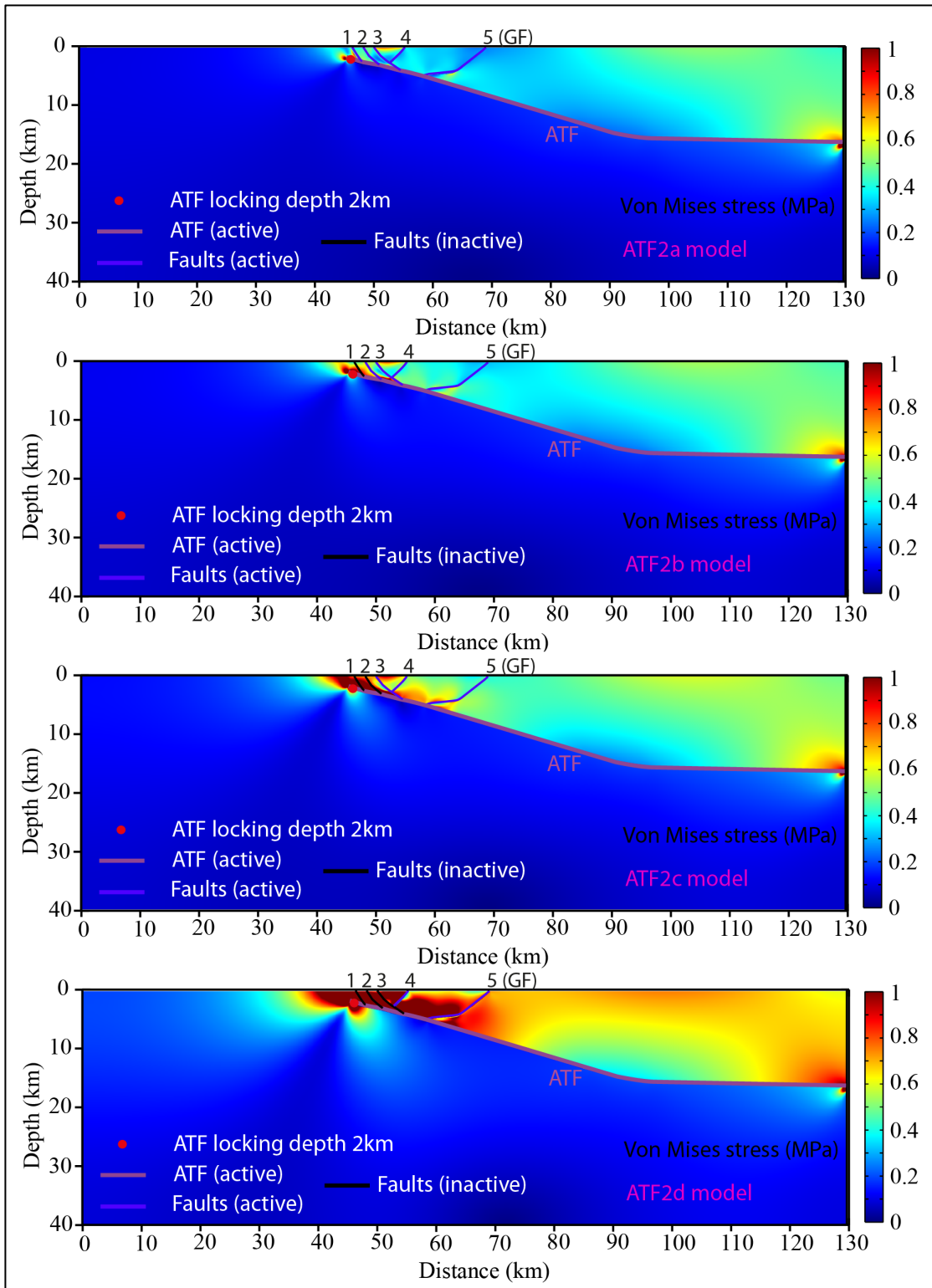
#### *4.3.2. Synthetic and antithetic fault activity effects*

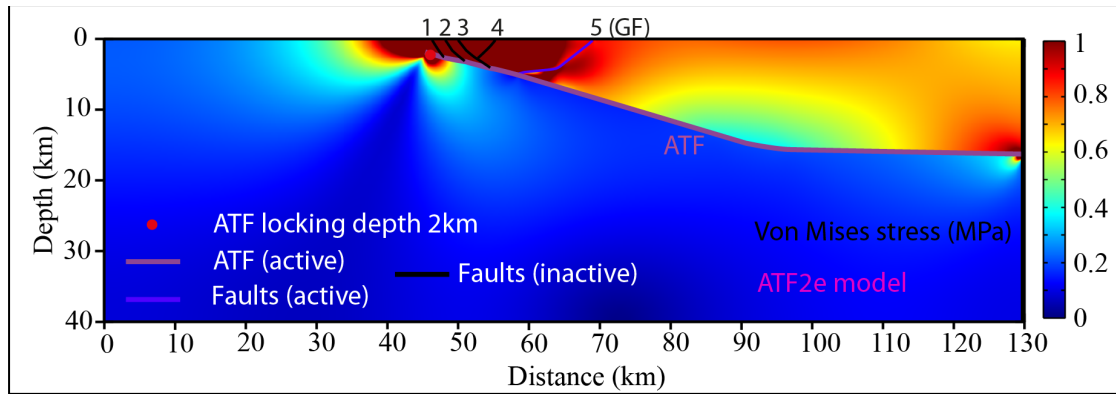
The effects of the synthetic and antithetic fault activity for different ATF locking depth on the horizontal velocity are here analyzed. In Figure 21, we show the results for a 2km ATF locking depth (ATF2 models). When all faults are considered active (ATF2a model), the velocity curve trend of the model is shifted towards higher values respect to the GPS data. The velocity trend of the models gradually improves when only the eastern faults are active (for example when only the antithetic faults are active; ATF2d-e models). The best fitting is reaching when only the Gubbio fault (GF) is maintained active.

The interseismic stress build-up for ATF2 model is shown in figure 22. We can observe that when all faults are considered active the stress accumulations in the ATF hanging-wall decrease (ATF2a model). In particular, more faults are active and more the stress build-up decreases. In fact when the Gubbio fault (GF, ATF2e model) is the only active structure the stress magnitude in the ATF hangingwall is reduced at values similar at the ATF<sub>e</sub> model (i.e when no synthetic and antithetic faults were active, Figure 20).



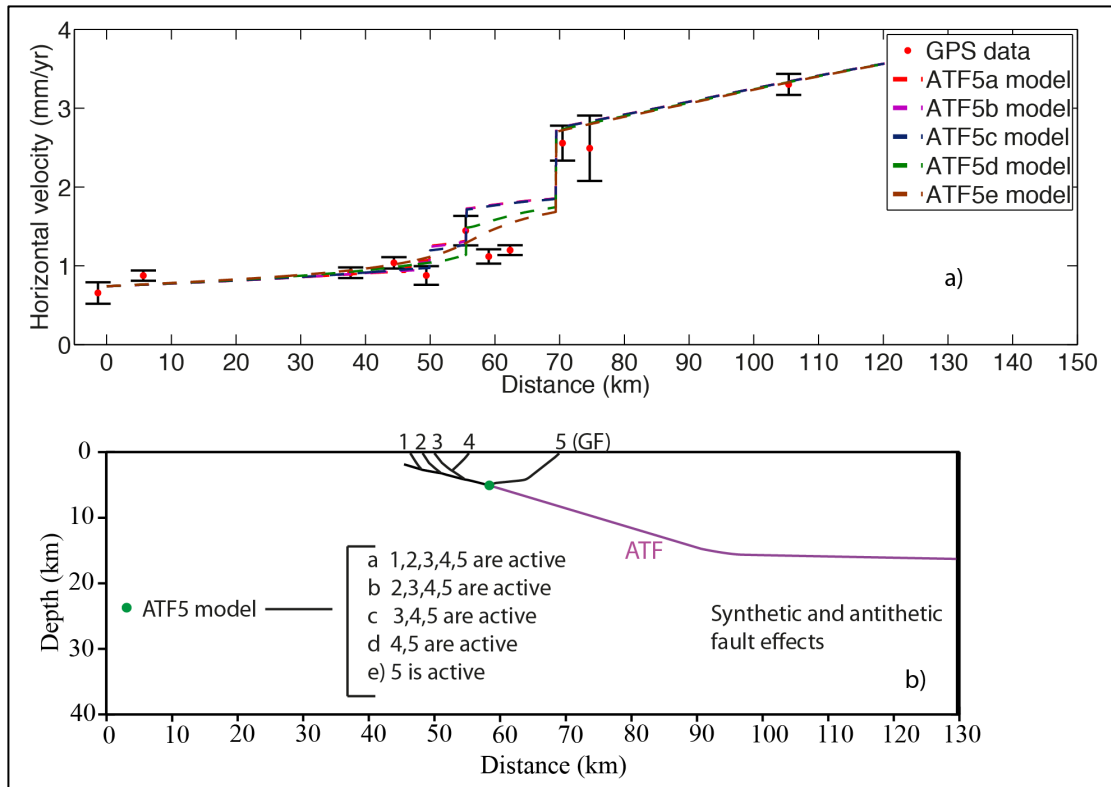
**Fig. 21.** Horizontal velocity for ATF2 model. We explore different configurations of the synthetic and antithetic fault activity (ATF2a, ATF2b, ATF2c, ATF2d and ATF2e models) for one ATF locking depth of 2km. The mechanical property values for these models are shown in Table 3. The best fitting is obtained for the ATF2e model (see Table 5).





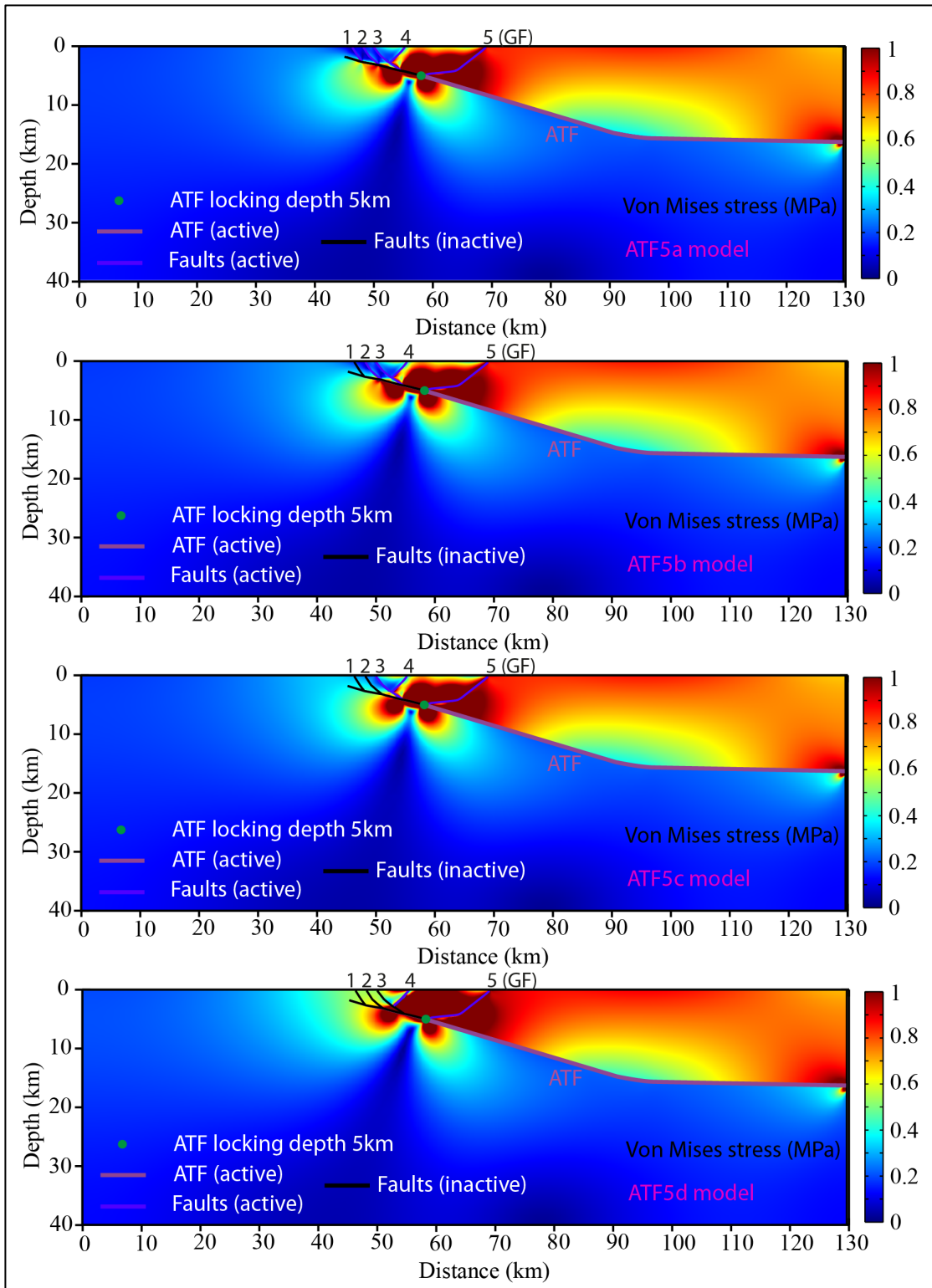
**Fig. 22.** Interseismic stress build-up for ATF2 model. We explore different configurations of the synthetic and antithetic fault activity (ATF2a, ATF2b, ATF2c, ATF2d and ATF2e models) for one ATF locking depth of 2km. The mechanical property values for these models are shown in Table 3.

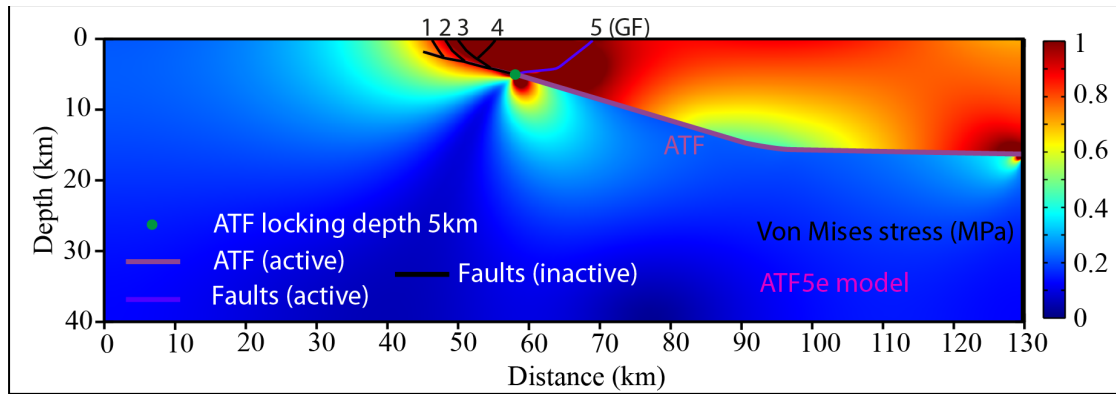
In figure 23 are shown the effects of synthetic and antithetic fault activity considering a 5km ATF locking depth (ATF5 models). Contrary to the ATF2 model (Figure 21), the velocity trend is greatly improved also for the cases in which the western faults are active (ATF5a-c, Figure 23). This is due to very low values of horizontal velocity in correspondence to the synthetic faults. In fact, in the ATF5a model the horizontal velocity in correspondence to the synthetic fault 1 is near to 1 mm/yr (Figure 23). Conversely, for the same fault activity configuration but considering one ATF locking depth of 2 km (ATF2a model, Figure 21), the horizontal velocity reaches values near to 1.5 mm/yr in correspondence to the fault 1. In this way, in the ATF5 models the effects of the antithetic faults are more relevant than those of the ATF2 models by localizing the higher values of the horizontal velocity versus east (Figure 23). The best fitting, also in this case, is reaching when only the Gubbio fault (GF) is maintained active (ATF5e model, Figure 23).



**Fig. 23.** Horizontal velocity for ATF5 model. We explore different configurations of the synthetic and antithetic fault activity (ATF5a, ATF5b, ATF5c, ATF5d and ATF5e models) for one ATF locking depth of 5km. The mechanical property values for these models are shown in Table 3. The best fitting is obtained for the ATF5e model (see Table 5).

Figure 24 shows the interseismic stress build-up for ATF5 model. The stress is located mainly in the Gubbio basin for all activity fault set-up. In this case the stress distribution is strongly controlled by the ATF locking depth.

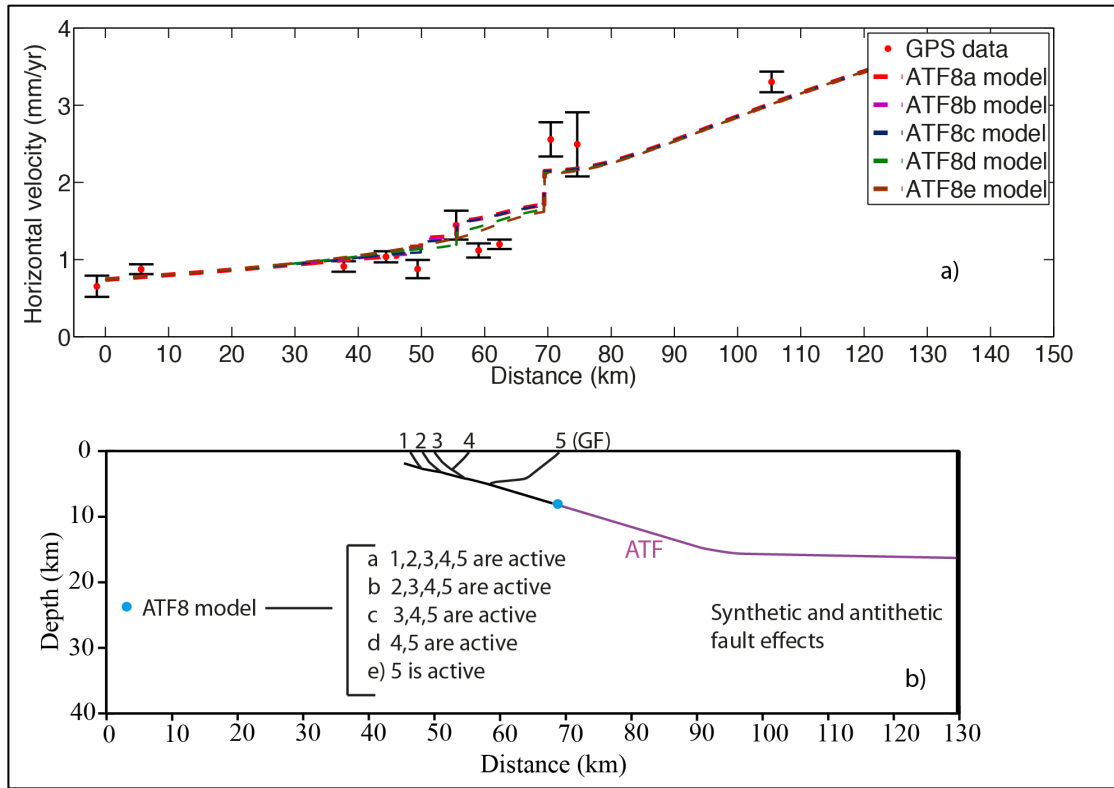




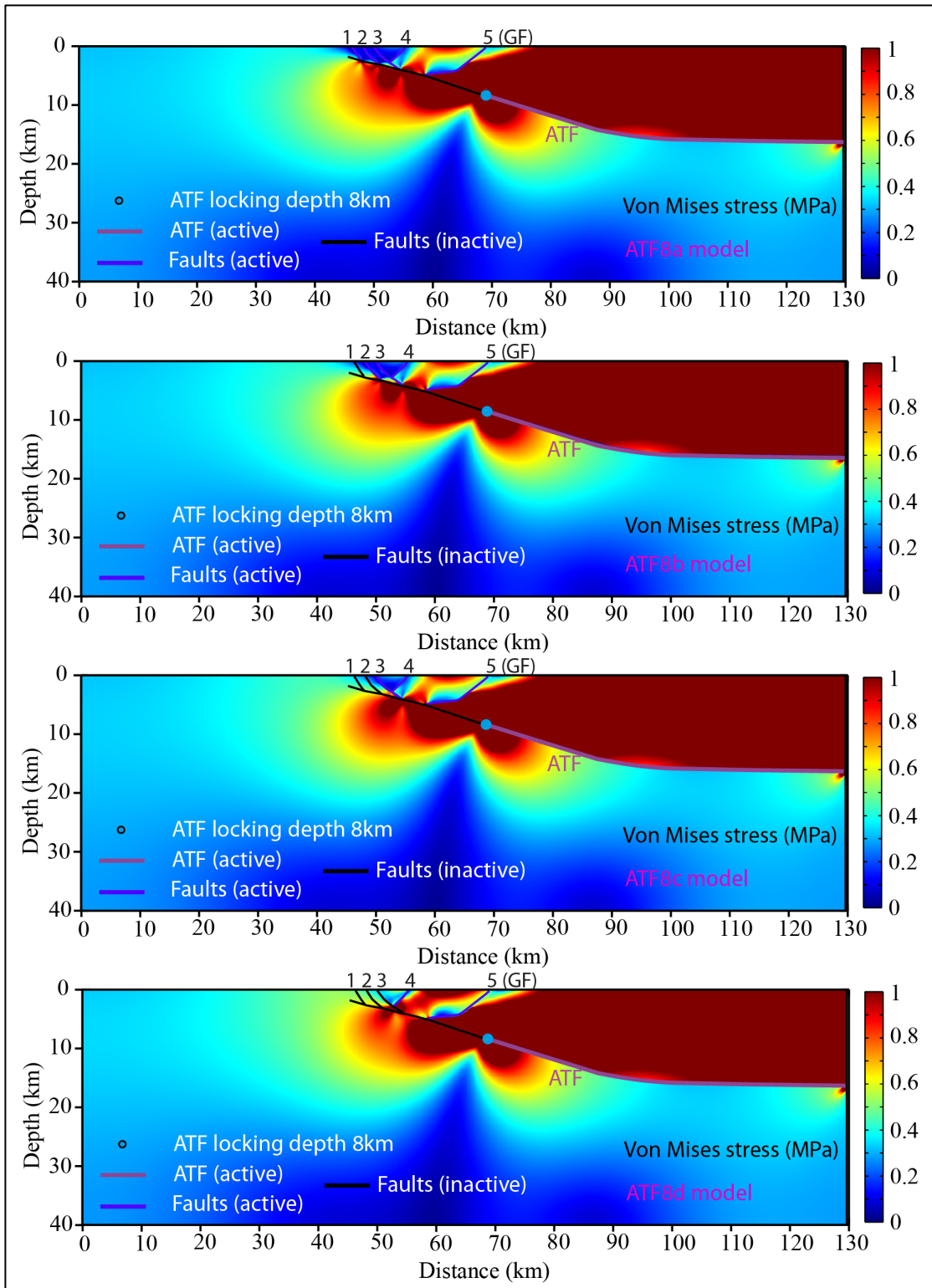
**Fig. 24.** Interseismic stress build-up for ATF5 model. We explore different configurations of the synthetic and antithetic fault activity (ATF5a, ATF5b, ATF5c, ATF5d and ATF5e models) for one ATF locking depth of 5km. The mechanical property values for these models are shown in Table 3.

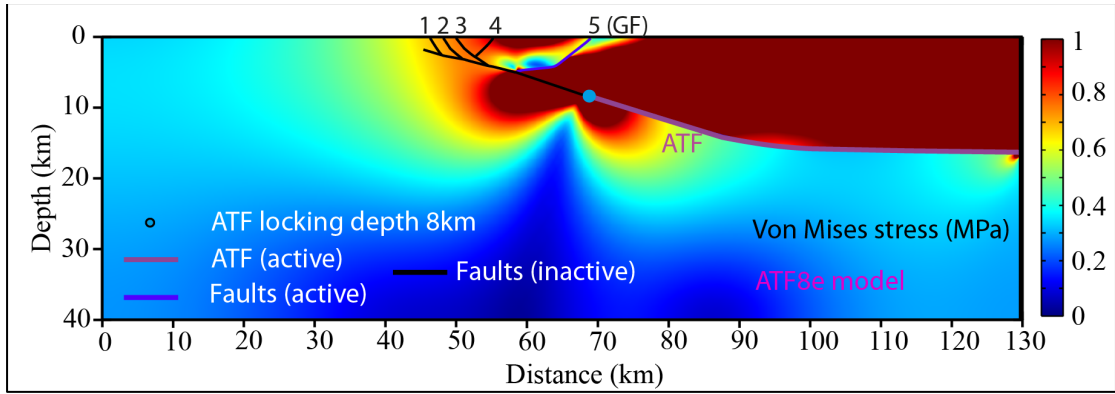
The effects of the synthetic and antithetic faults for one ATF locking depth of 8 km are shown in figure 25 and 26 (ATF8 models). The horizontal velocity trend of the models shows no significant difference between the configurations examined (Figure 25). In fact, in this case, the deformation is located mainly in proximity of the Gubbio fault even more respect the ATF5 model where high values of velocity were also obtained in correspondence of the other antithetic fault (Figure 23). It is notable that the modelled velocity trend underestimates GPS data, as in the cases where the influence of the synthetic and antithetic fault activity is neglected (Figure 20). In this way the influence of deeper ATF locking depth on the other faults decreases. However the best velocity fit in this case is obtained by ATF8a model where all faults are active. This is reasonable because the contribute of the synthetic faults (though small in this case) tends to shift the horizontal velocity trend toward higher values. The interseismic stress build-up increases in depth near the ATF flat and in the eastern part of the model due at a deeper ATF locking depth (Figure 26).

The last case of these models considers one ATF locking depth of 11 km (ATF11 models, Figure 27-28). The effects are very similar at the model previously described

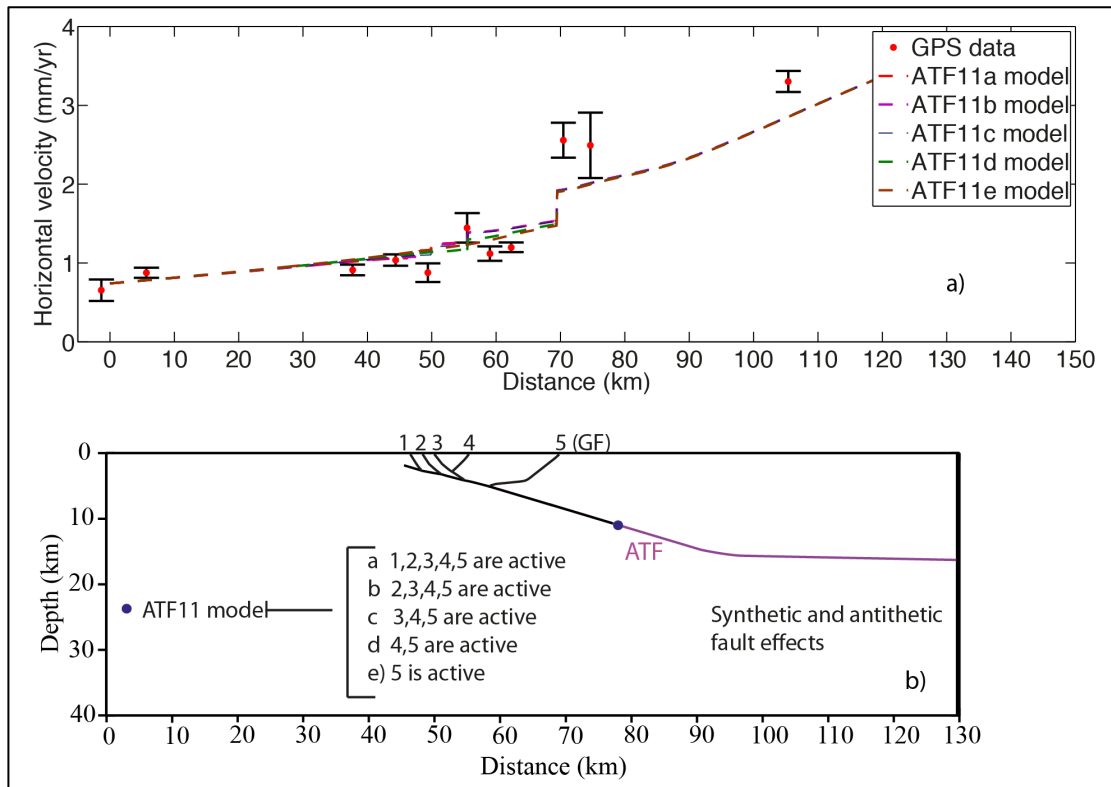


**Fig. 25.** Horizontal velocity for ATF8 model. We explore different configurations of the synthetic and antithetic fault activity (ATF8a, ATF8b, ATF8c, ATF8d and ATF8e models) for one ATF locking depth of 8km. The mechanical property values for these models are shown in Table 3. The best fitting is obtained for the ATF8a model (see Table 5).

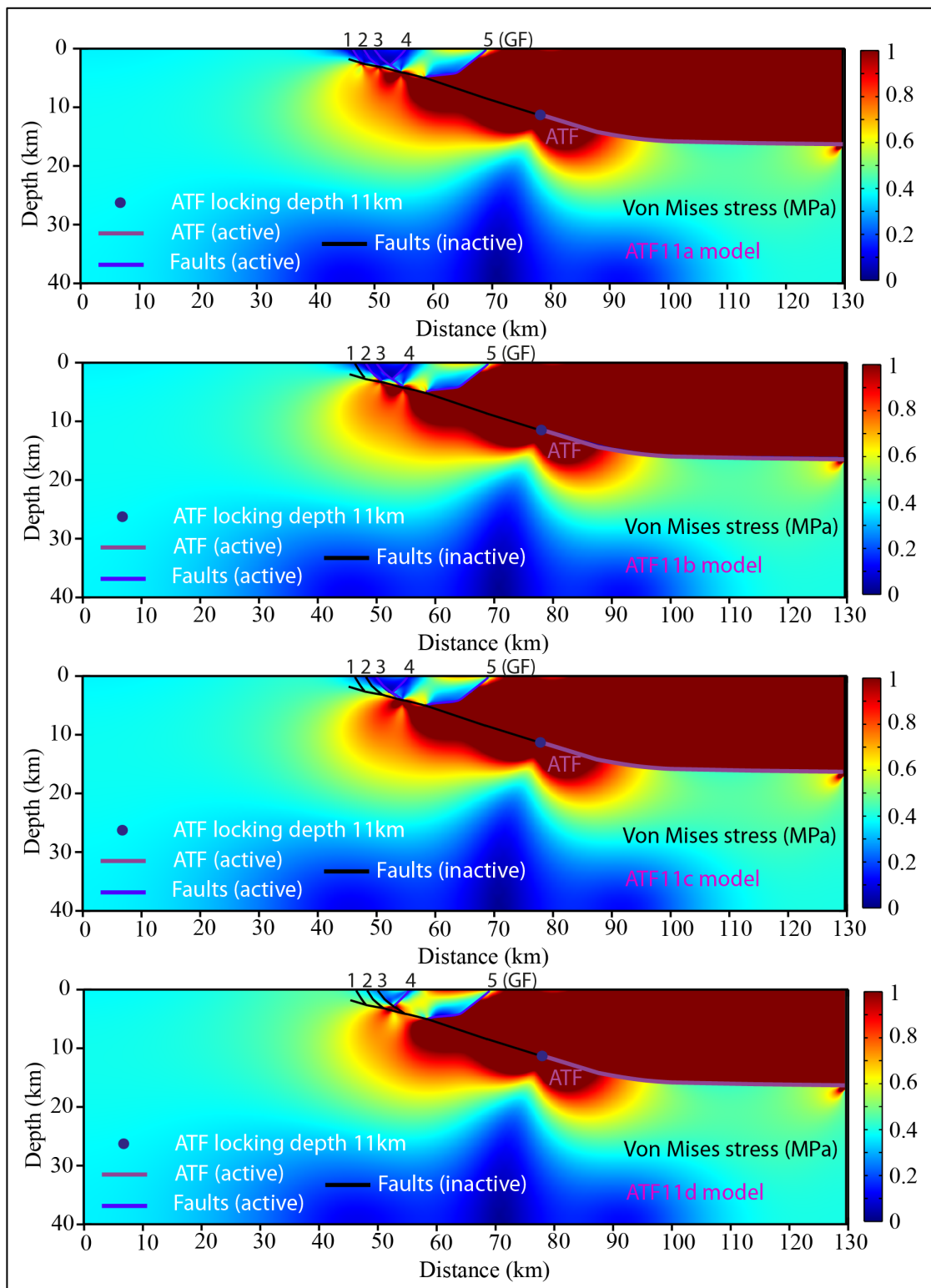




**Fig. 26.** Interseismic stress build-up for ATF8 model. We explore different configurations of the synthetic and antithetic fault activity (ATF8, ATF8b, ATF8c, ATF8d and ATF8e models) for one ATF locking depth of 8km. The mechanical property values for these models are shown in Table 3.



**Fig. 27.** Horizontal velocity for ATF11 model. We explore different configurations of the synthetic and antithetic fault activity (ATF11a, ATF11b, ATF11c, ATF11d and ATF11e models) for one ATF locking depth of 8km. The mechanical property values for these models are shown in Table 3. The best fitting is obtained for the ATF11a model (see Table 5).



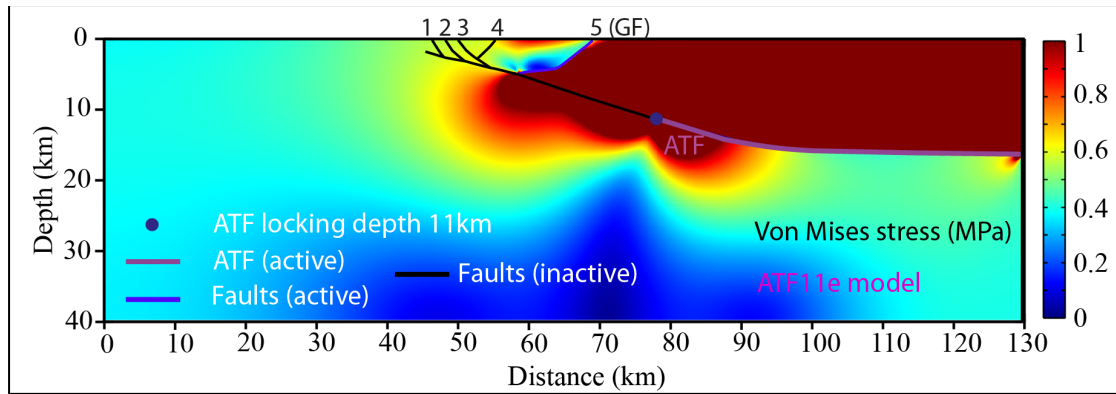


**Fig. 28.** Interseismic stress build-up for ATF11 model. We explore different configurations of the synthetic and antithetic fault activity (ATF11, ATF11b, ATF11c, ATF11d and ATF11e models) for one ATF locking depth of 11km.

Before to analyze the lithology effects, we compare the best solution obtained between the models previously considered. Figure 29 shows that the best fitting is obtained considering the ATF locking depth at 5 km and only the antithetic Gubbio fault is active (ATF5e model, Table 5). Therefore, in the next analyses we will consider this model as the base to study the effects of the lithology.

#### 4.3.3. Lithology effects

Comparing the horizontal velocity obtained by ATF5e model (homogeneous crust) and ATF5e-litho model (heterogeneous crust, Table 5), we don't observe remarkable differences (Figure 30). Conversely the stress build-up is strongly influenced by the lithology (Figure 31). In fact the mechanical contrast between different layers causes a redistribution of the stress. In particular we have higher values of stress (respect to the homogeneous case) between the evaporites and the surrounding rocks (phyllites and carbonates) where the mechanical contrast is strong. On the contrary, at shallower depth, the stress build-up decreases due at the presence of the turbidites (soft material).

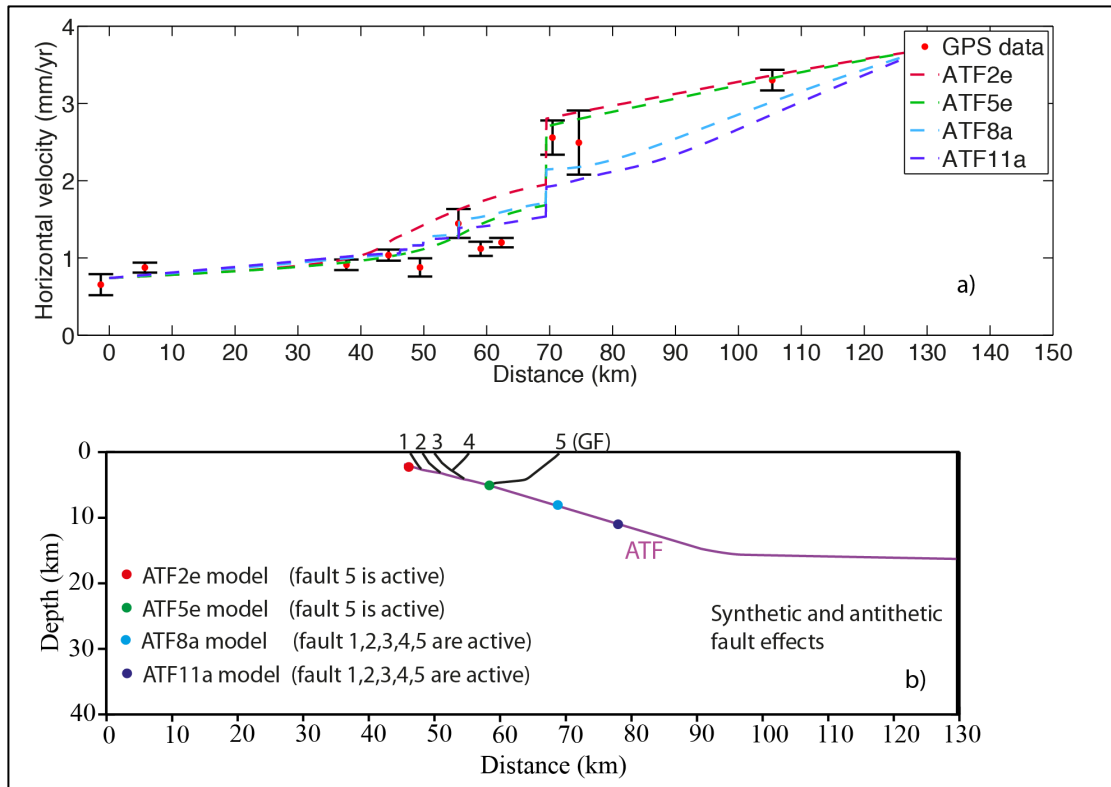


**Fig. 29.** Horizontal velocity for ATF2e, ATF5e, ATF8a and ATF11a models. We compare the best solution between ATF2, ATF5, ATF8 and ATF11 models. The best fitting is obtained by ATF5e model (see Table 5).

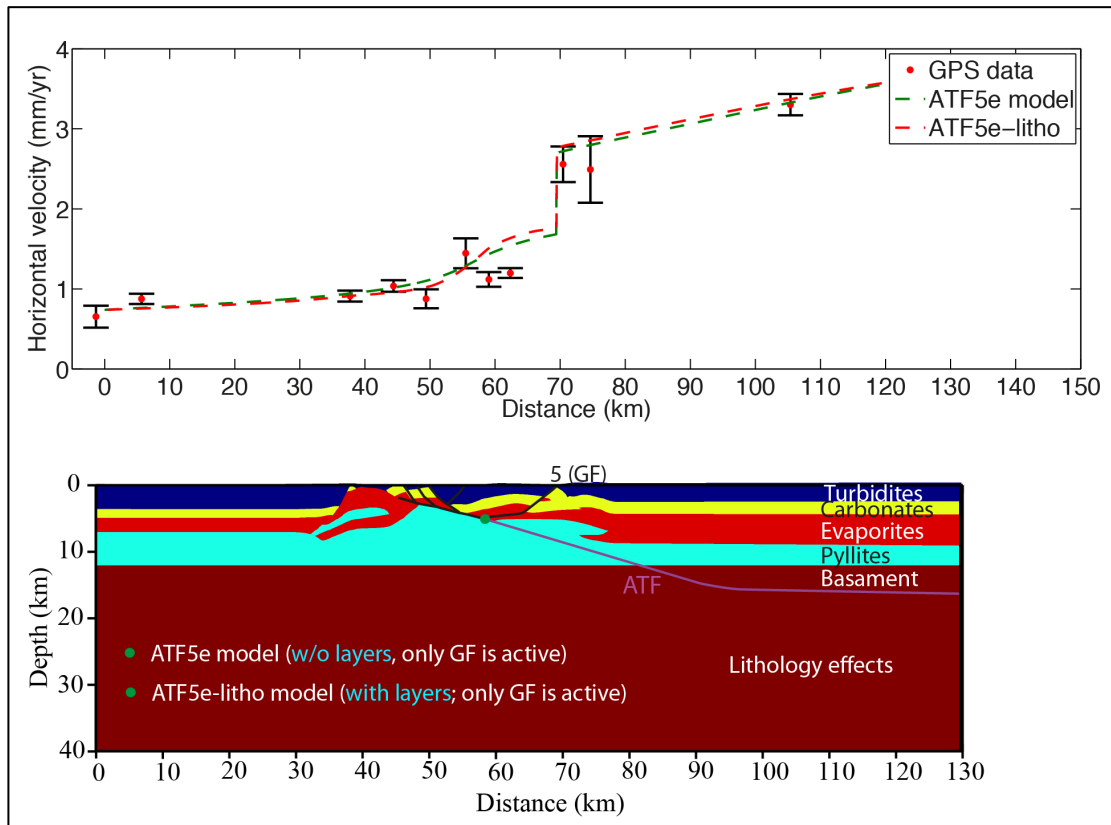


**Fig. 30.** Horizontal velocity for ATF5e (homogeneous crust) and ATF5e-litho (heterogeneous crust, Table 5) models. Note that no remarkable differences are found.

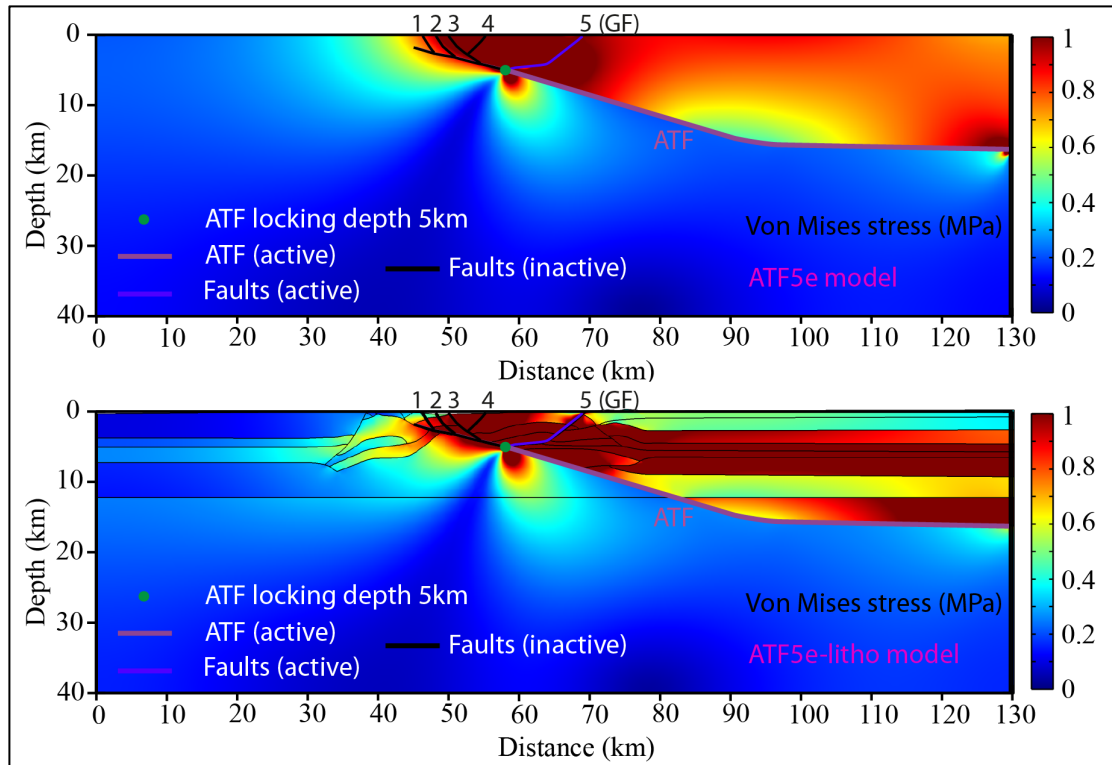


**Fig. 31.** Interseismic stress build-up for ATF5e and ATF5e-litho models. In these models only the ATF fault (with locking depth of 5 km) and GF are active.

#### 4.4. Discussion and concluding remarks

The results of the simulations suggest important considerations concerning the mechanical role of ATF fault zone to accommodate the extension in Northern Apennines. At first, the “ATF model” results (Figure 19) highlight that the GPS velocity data are better fitted considering one ATF locking depth of 5km (Table 5). In fact, for locking depth of 8 or 11 km, the horizontal velocity obtained is underrated. Otherwise, for shallower locking depth (2 km) we obtain overestimated deformation rates. However the only activity of the ATF is not sufficient to reflect the deformation

rates. In fact, the best fitting of the horizontal velocity is obtained by considering an active Gubbio fault zone (ATF5e model, Figure 29-30).

An important aspect shown in the synthetic and antithetic fault activity models is that the ATF locking depth influence the deformation rates in proximity of the other faults. This is evident comparing the horizontal velocity trend obtained for 2 km (Figure 21) and for 5 km ATF locking depth (Figure 23). In fact for shallower ATF locking depth (Figure 21) the contribute of synthetic faults is important and leads the horizontal velocity curve towards higher values. On the contrary, for deeper ATF locking depth the deformation is accommodate mainly by the antithetic faults (Figure 23).

The results shown in Figure 32 suggest two mainly mechanisms of build-up and repartition of the interseismic stress: 1) stress bipartition between hanging wall (high values) and footwall (low values) inferred by the activity of the ATF; 2) high stress build-up in the evaporites due to the mechanical contrast with the surrounding geological formations. The stress bipartition is consistent with the microseismicity of this area that is characterised by higher rate in the ATF hanging wall (Figure 32). In particular in figure 32 we compare the relocated seismic events with  $M_L$  3.2 (Chiaraluce et al., 2007) and a distance from the section less then 10 km with the Von Mises shear stress obtained by ATF5e-litho model. We can observe that the microseismicity delineates an angle of  $17^\circ$  of ATF fault zone but is located also near the Gubbio fault zone where there are high values of stress.

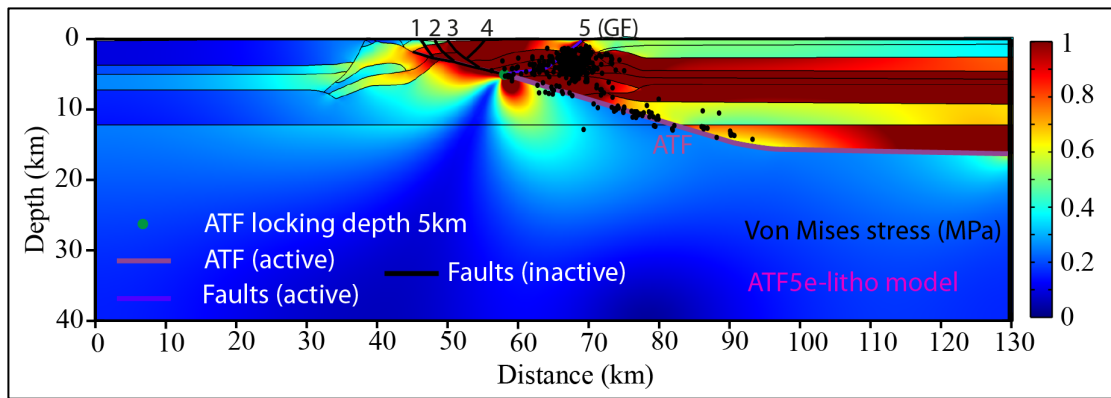


**Fig. 32.** Comparison between the microseismicity (by Chiaraluce et al., 2007) and the interseismic stress build-up obtained by ATF5e-litho model.

In conclusion, we suggest that the presence of a very compliant Alto Tiberina fault zone (or a free-slip ATF plane) is a first order condition to redistribute the stress in this part of the Northern Apennines.

Models	WRMS
ATFa	0.62
ATFb	0.30
ATFc	0.31
ATFd	0.38
ATF2a	1
ATF2b	0.93
ATF2c	0.81
ATF2d	0.51
ATF2e	0.37
ATF5a	0.36
ATF5b	0.35
ATF5c	0.35
ATF5d	0.25
ATF5e	0.19
ATF8a	0.21
ATF8b	0.23
ATF8c	0.26
ATF8d	0.26
ATF8e	0.27
ATF11a	0.23
ATF11b	0.24
ATF11c	0.25
ATF11d	0.25
ATF11e	0.25
ATF5e-litho	0.23

**Tab. 5.** Weighted root mean squares (WRMS) for each model are calculated. ATF5e is the best model obtained from the 2D numerical simulations. In yellow the relative best model for each model set.

## **5. Modelling the interseismic deformation of the Alto Tiberina fault system by 3D numerical simulations: fault roughness effects.**

### 5.1. Introduction

In the chapter 4 we have modelled the interseismic deformation of the ATF system through 2D numerical simulations. The plain-strain approximation is adequate for geological structures with lateral continuity or for a specific sector of a structure. It is preliminary method to constrain models before 3D numerical simulations (which require higher computational costs) that we present in this chapter. In the next analysis, we examine the effects of the 3D geometries on the interseismic deformation along the Alto Tiberina Fault (ATF) and Gubbio Fault (GF). We adopt the same ATF5e model setting (the best model by 2D simulations); hence no lithology effect is considered. Moreover we examine two particular cases: the first considers a planar ATF zone whereas in the second case we investigate the effects of the ATF fault zone roughness as it has been defined by seismic profiles (Chapter 2).

### 5.2. Model description

We have selected a study volume of  $150 \times 150 \times 40 \text{ km}^3$  where the Alto Tiberina and Gubbio fault zones are located (Figure 33). We have defined the geometry by means of Rhinoceros (<http://www.rhino3d.com>, a graphic vector code for tridimensional objects). The surface topography is resampled at 1 km from Shuttle Radar Topographic Mission (SRTM, <http://www2.jpl.nasa.gov/srtm/>; Figure 34). We have built fault blocks including the ATF and GF zones (Figure 34) with thickness of 800



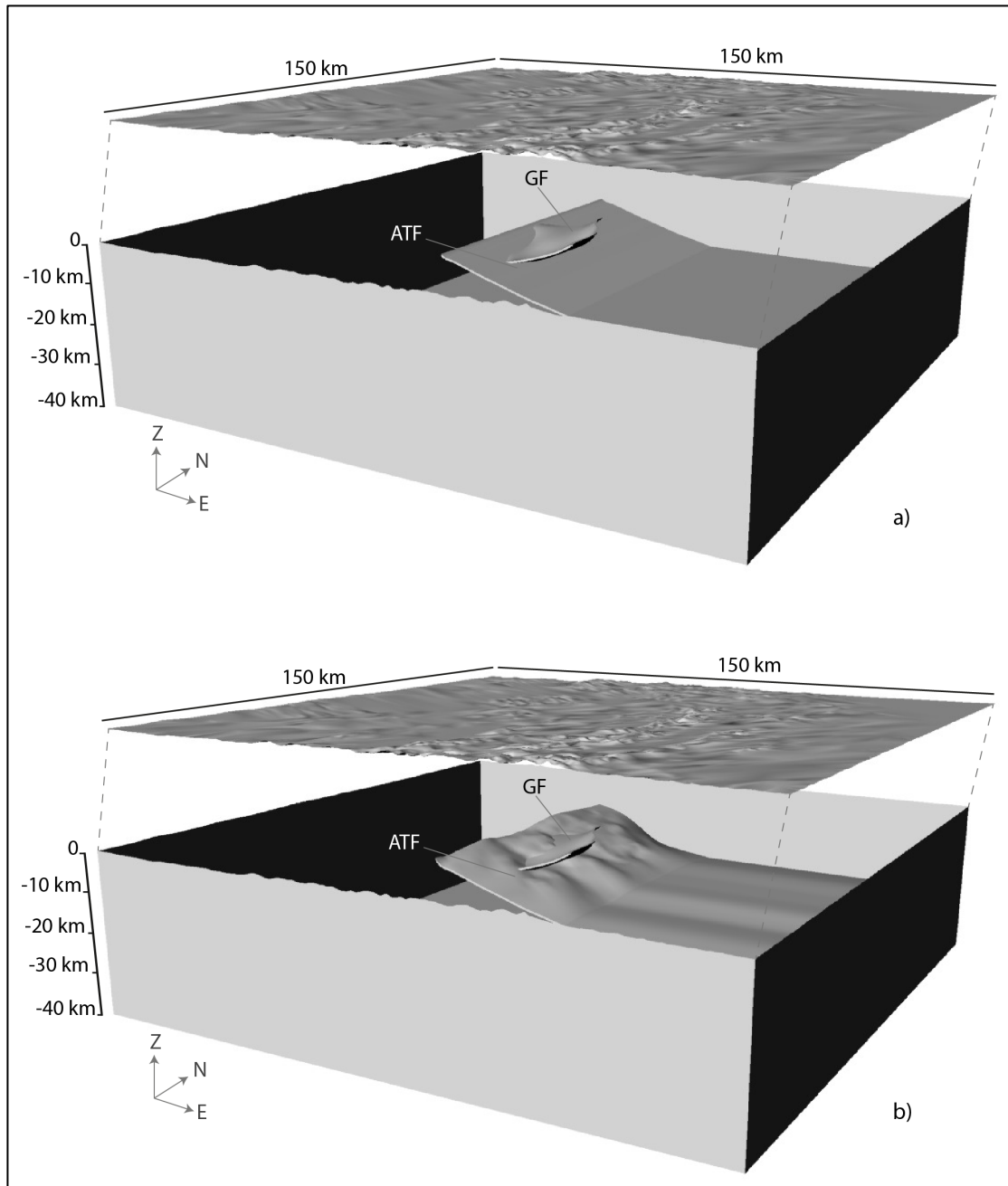


**Fig. 34.** Geometry for ATF\_planar model a) and ATF\_nonplanar model b). We build a crustal volume with dimension  $150 \times 150 \times 40 \text{ km}^3$ . The faults are thick 800 m.

We have imported the obtained geometries in Cubit (<https://cubit.sandia.gov>) to build the tetrahedral mesh (Figure 35). This element type increased the computational costs respect to hexahedra but is better suited to low angle geometries (as the ATF).

Rheology, material properties and boundary conditions are defined in PyLith (<http://geodynamics.org/cig/software/pylith/>; Chapter 3). The crust is characterised entirely by an elastic rheology defined in table 6. We consider an ATF locking depth of 5 km for both the models. As for the 2D models, in an initial stage the crust is subjected to gravity load and then stretched for 1000 years. According to the present-day plate kinematics of the Northern Apennines region, we apply a constant horizontal velocity of 0.5 mm/yr and 3.5 mm/yr on the SW and NE lateral boundaries respectively (Figure 35).

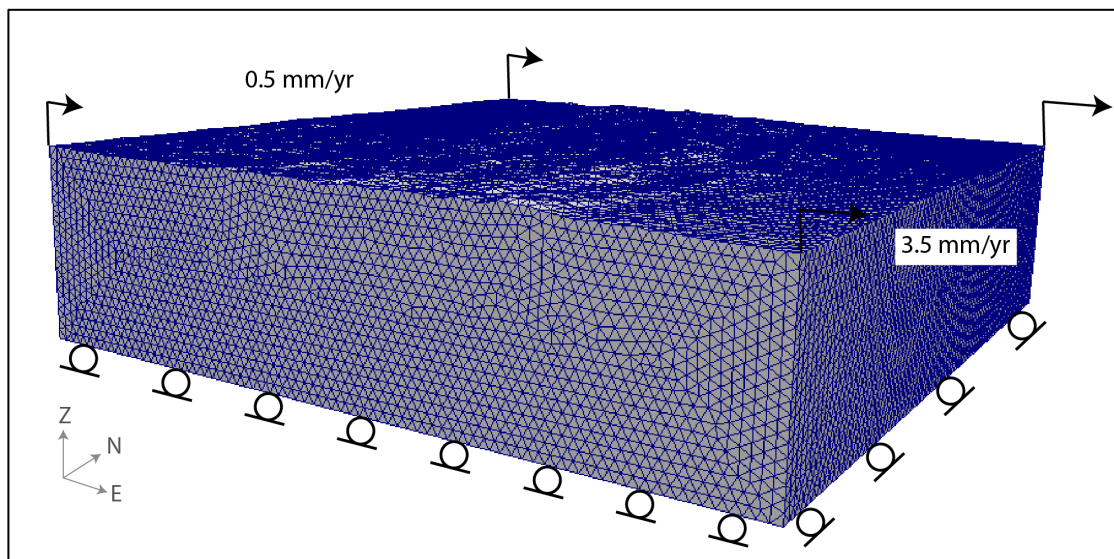


**Fig. 35.** Mesh and boundary conditions for ATF\_planar and ATF\_nonplanar models. Note that the boundary conditions are the same of the 2D models (Chapter 4).

	Young modulus (Pa)	Poissons ratio	Density (Kg/m <sup>3</sup> )
Intact rock	5.33e10	0.25	2570
ATF fault zone	1e7	0.35	2500
Gubbio fault zone	1e8	0.35	2500

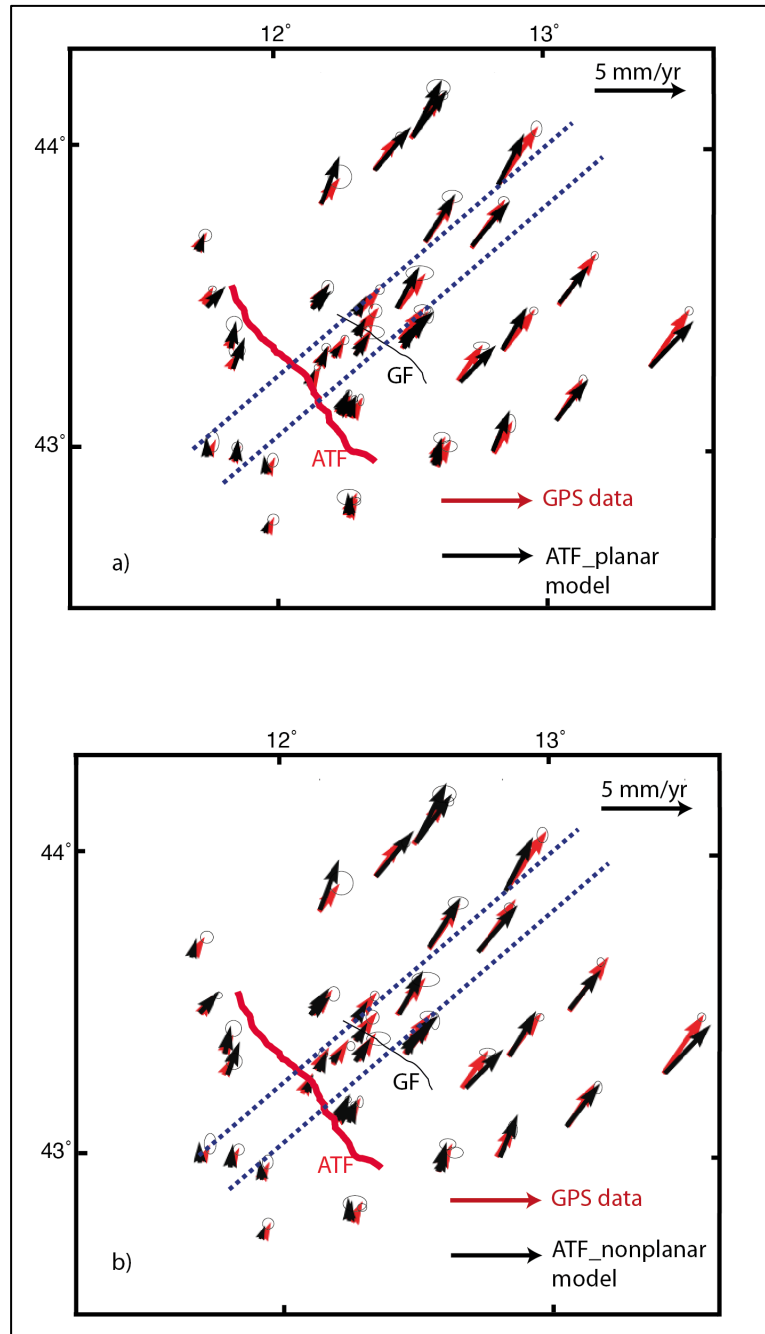
**Tab. 6.** Elastic properties for ATF\_planar and ATF\_nonplanar models.

### 5.3. Model results

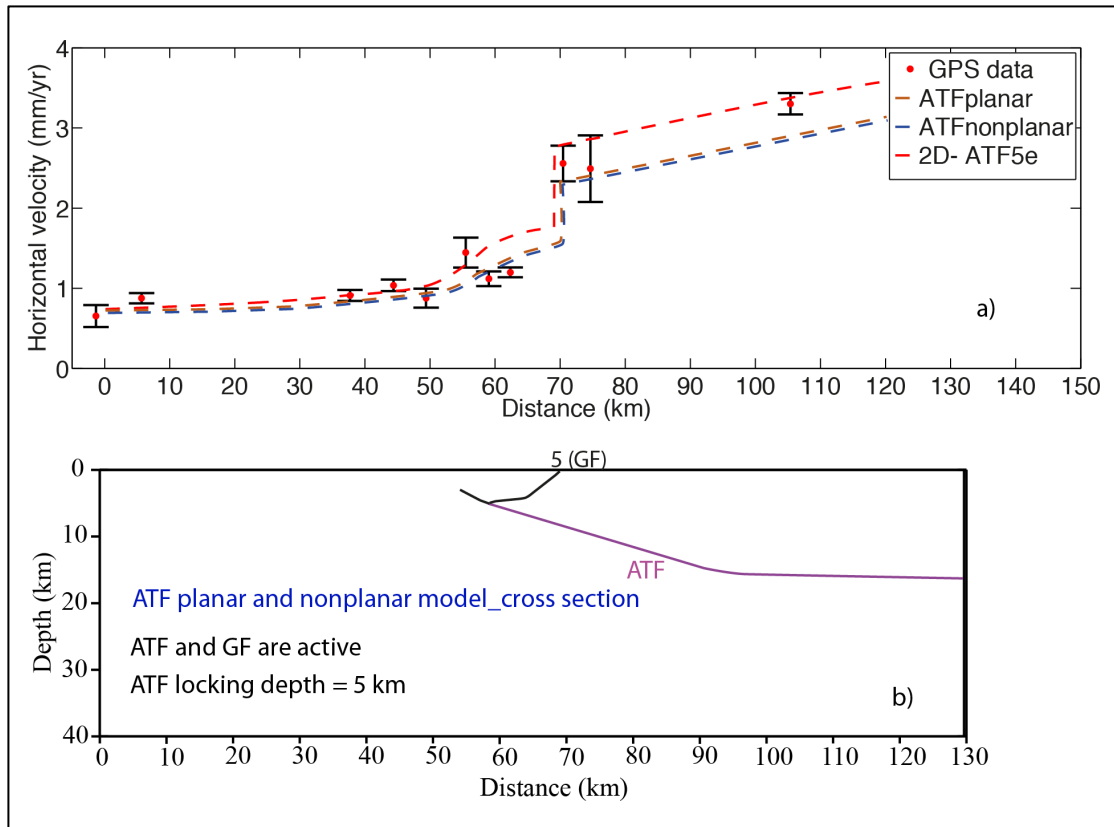
In Figure 36 we compare the velocity field obtained from the modelling with the observed GPS data. We can note that both the models (ATF\_planar and ATF\_nonplanar) agree with the general velocity field observed. The fitting is well constrained both for the velocity vector orientations that for the magnitude. The difference between ATF\_planar and ATF\_nonplanar models can be observed in Figure 37 where horizontal velocity profiles are plotted along the same cross section used for the 2D models. The models show approximately the same trend of the horizontal velocity. A very small decreasing of the ATF\_nonplanar respect to ATF\_planar model is observed.

Figure 38 shows the interseismic stress build-up for ATF\_planar and ATF\_nonplanar models. Here, larger differences between the models are found. Considering the ATF\_planar case (Figure 38a) we observe that the stress build-up is mainly located above 5 km of depth and along the Gubbio fault. Below the ATF locking depth the stress build-up decreases and it is homogeneous for the entire fault. Only local stress anomalies (with relative higher stress values) are found near 12 km of depth where there is an abrupt change of dip between ATF-ramp and ATF-flat. Otherwise in the

ATF\_nonplanar model (Figure 38b) the stress distribution is strongly affected by the ATF roughness both above that below the ATF locking depth. In particular we can observe that below 5 km of depth strong stress accumulations are located along the ATF ramp due to the roughness slopes.



**Fig. 36.** Comparison between the observed and modelled velocity field. Note that the differences between ATF\_planar (a) and ATF\_nonplanar (b) models are minimal. The dotted lines indicate the range of GPS stations considered in figure 37.



**Fig. 37.** Horizontal velocity obtained by ATF<sub>planar</sub> and ATF<sub>nonplanar</sub> models. In order to compare the velocity field obtained with the 2D models, we consider only the GPS stations whose distance from the cross-section is less than 10 km (the limit is represented by the dotted line in figure 36); in particular the GPS stations considered are from SW to NE: SIO1, REPI, CSSB, VALC, UMBE, ATLO, MVAL, PIET, ATFO, ATBU, FOSS.

#### 5.4. Discussion and concluding remarks

The ATF<sub>planar</sub> model results are in good agreement with the ATF<sub>nonplanar</sub> case at least in some aspects. In fact, if the horizontal velocity profiles (Figure 37) show similar trends, the stress distribution is strongly affected by the ATF roughness in the ATF<sub>nonplanar</sub> model (Figure 38). These models highlight that the stress build-up is mainly located in the first 5 km of depth along the Gubbio antithetic fault, that being well-oriented with  $\sigma_1$ , could fail seismically. At same time, overstressed patches induced by the geometrical irregularity of the ATF zone, could also fail seismically, if

well oriented with  $\sigma_1$ . In this case, the microseismicity situated below 5 km of depth could be justified (Chapter 2).

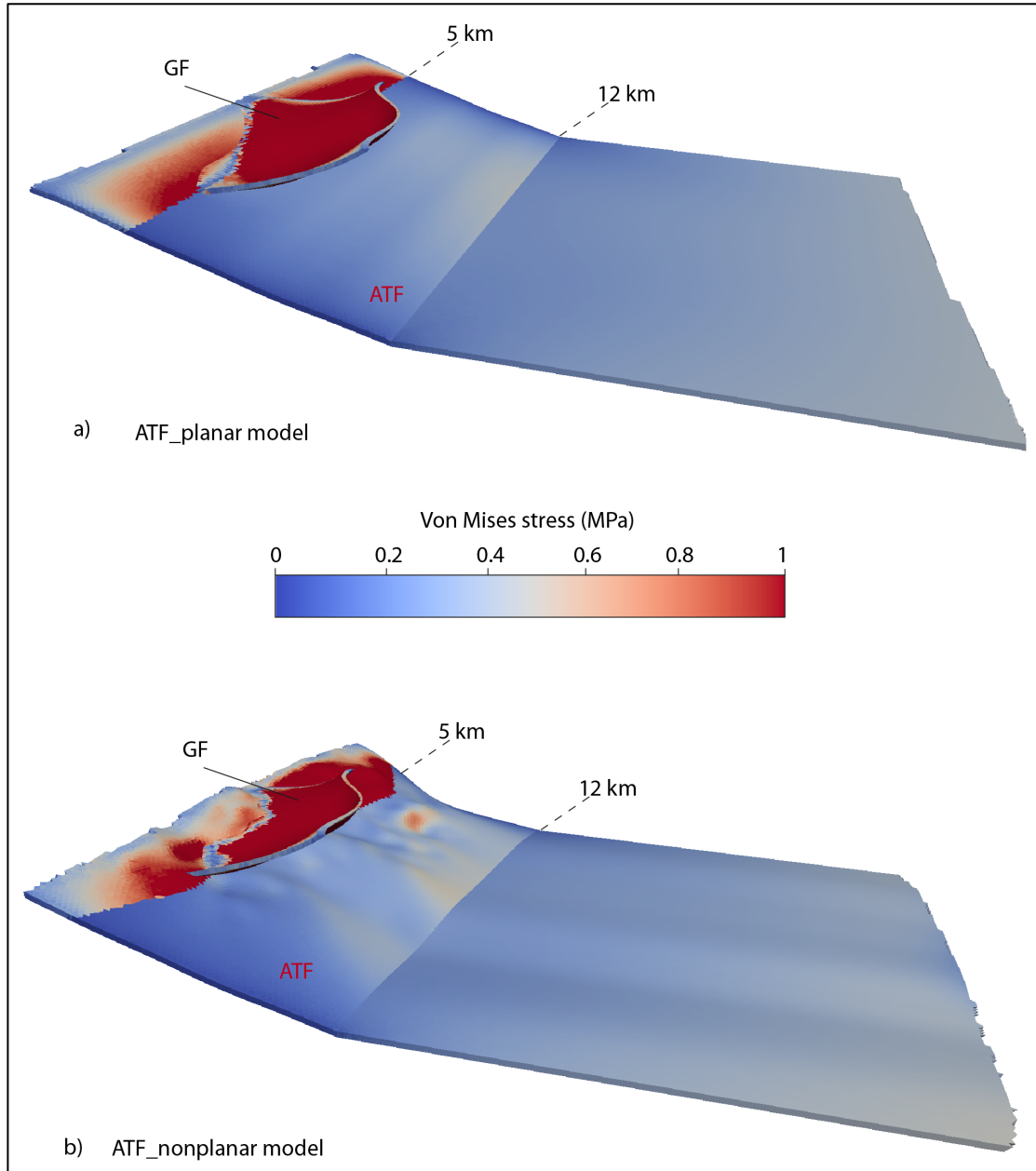


**Fig. 38.** Interseismic stress build-up for ATF\_planar (a) and ATF\_nonplanar (b) models. Note that, in the both cases, the stress is mainly accumulated in the first 5 km of depth and along the Gubbio fault zone. In the ATF\_nonplanar model the stress distribution is affected by the ATF roughness, in fact high values of stress below 5 km are found.

In this context the dip-angle variation of the fault plane assumes an important role respect to the frictional reactivation theory described in the chapter 2. In figure 39a we plot the ATF the dip-angle variation on the geometry by Mirabella et al., (2011). We can observe that the dip-angle distribution is strongly heterogeneous though the main dip is around  $17^\circ$ . In fact some very flat areas ( $1^\circ$ ) coexist with higher dip area (greater than  $35^\circ$ ). Considering the analysis on the frictional reactivation of a normal fault done in the chapter 2, we calculate the distribution of the maximum frictional coefficient  $\mu$  (Figure 39b) for which it is possible to obtain slip along the dip-angle distribution of figure 39a. In other words, initially, we calculate the reactivation angle  $2\theta^*$  (90-dip) for frictional lock-up ( $R \rightarrow \infty$ ) and after we calculate the correspondent frictional coefficient  $\mu$  (values of  $2\theta^*$  corresponding to different values of  $\mu$  are plotted in Figure 40). Figure 39b shows that the frictional reactivation of the Alto Tiberina low angle normal fault is possible along some patches even considering typical Byrlee friction coefficient (in this case 0.6-0.75) and without to invoke necessarily fluid overpressure. Then, these patches are surrounding by a matrix defined by low values of friction ( $\mu < 0.4$ ). Rocks with high values of friction ( $\mu > 0.6$ ) found along exhumed low-angle normal faults highlight a prevalent velocity weakening behaviour while for low values of  $\mu$  ( $< 0.4$ ) they point out a velocity strengthening behaviour (Collettini, 2011). This indicate that the microseismicity on the ATF plane could be induced on patches with high values of  $\mu$ , overstressed by the stable slip promoted by velocity strengthening material.

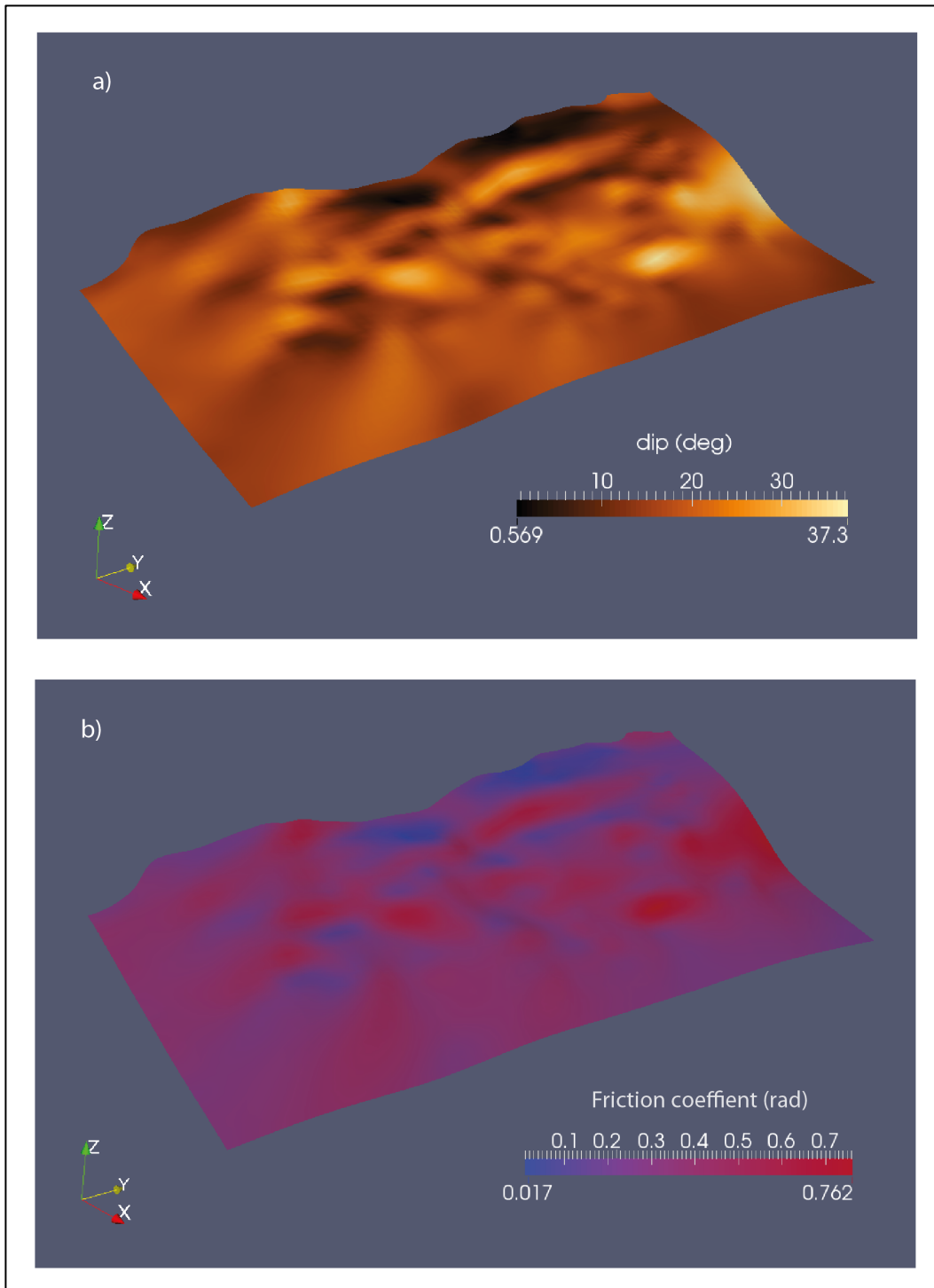


**Fig. 39.** a) ATF dip-angle variation depending of the roughness in degree. b) Maximum friction coefficient  $\mu$  for which it is possible to reactivate the fault along the dip-angle distribution of figure a.

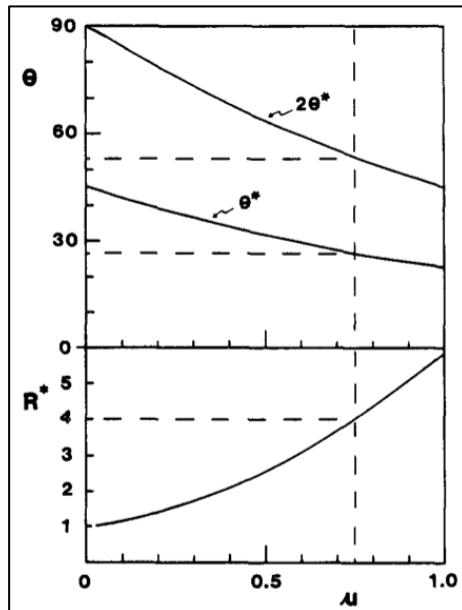


**Figure 40.** Variation of optimum reactivation angle,  $\theta^*$ ,  $2\theta^*$  and minimum positive stress ratio for reactivation,  $R^*$ , with frictional coefficient,  $\mu$  (from Sibson, 1985).

In order to understand as the fault plane roughness influence the interseismic stress build-up we consider another model where a Coulomb friction law is applied along the ATF plane (ATF\_fri model; Fig 41). In this case we consider that the entire fault is locked assuming high values of friction ( $\mu=0.7$ ) and cohesion (100 MPa). In this way no spontaneous rupture are generated during the total time of the simulation (1000 years). The boundary conditions are the same of the previous models (ATF\_planar or nonplanar models) and they are shown in figure 41b. In this case we build a mesh of hexahedral elements because it facilitates the convergence when frictional contacts are used.

Figure 42 shows the stress distribution along the ATF plane. We can observe that the stress build-up is strongly sensible at the change of dip along the fault. In fact high stress accumulations are located in proximity of the patches with higher dip-angles, while very flat area along the fault plane present lower values of stress.

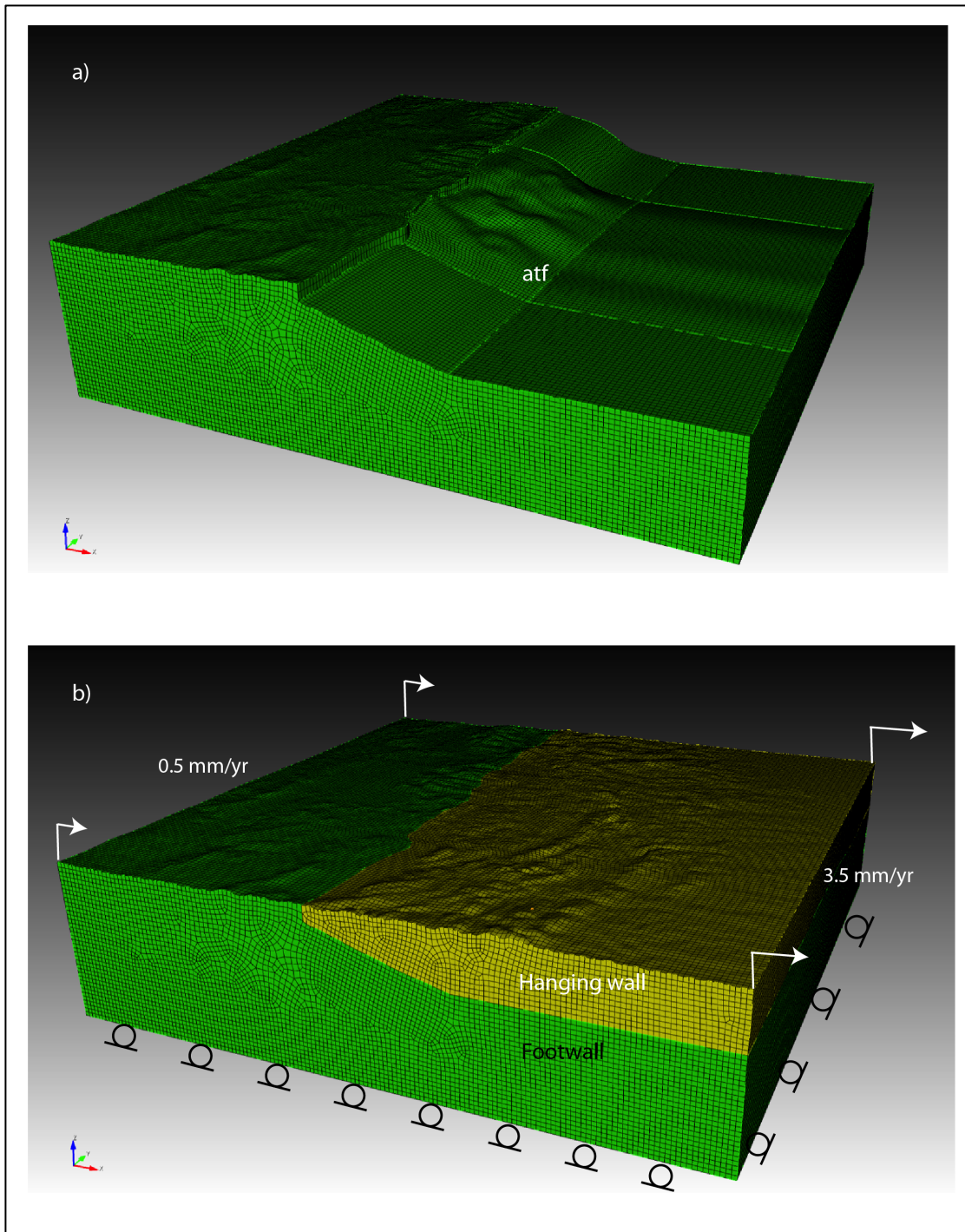


**Fig. 41.** Hexahedral mesh and boundary conditions for ATF\_fri model. Note that mesh is divided in two subdomains (hanging-wall and footwall) in order to insert cohesive cells to define the fault (Chapter 3).

The 3D models discussed in this chapter demonstrate that a stable slip is prevalent below 5 km of depth in according with the 2D simulations. In addition we hypothesise that same patches could be locked and seismically reactivated due at the loading on

roughness slope  $> 30^\circ$ . The new challenge is therefore to understand whether these patches, during the dynamic rupture, can communicate with each other through velocity strengthening material, generating moderate or large magnitude earthquakes. Nevertheless, new seismological data are necessary to constrain velocity-weakening patches along the ATF.

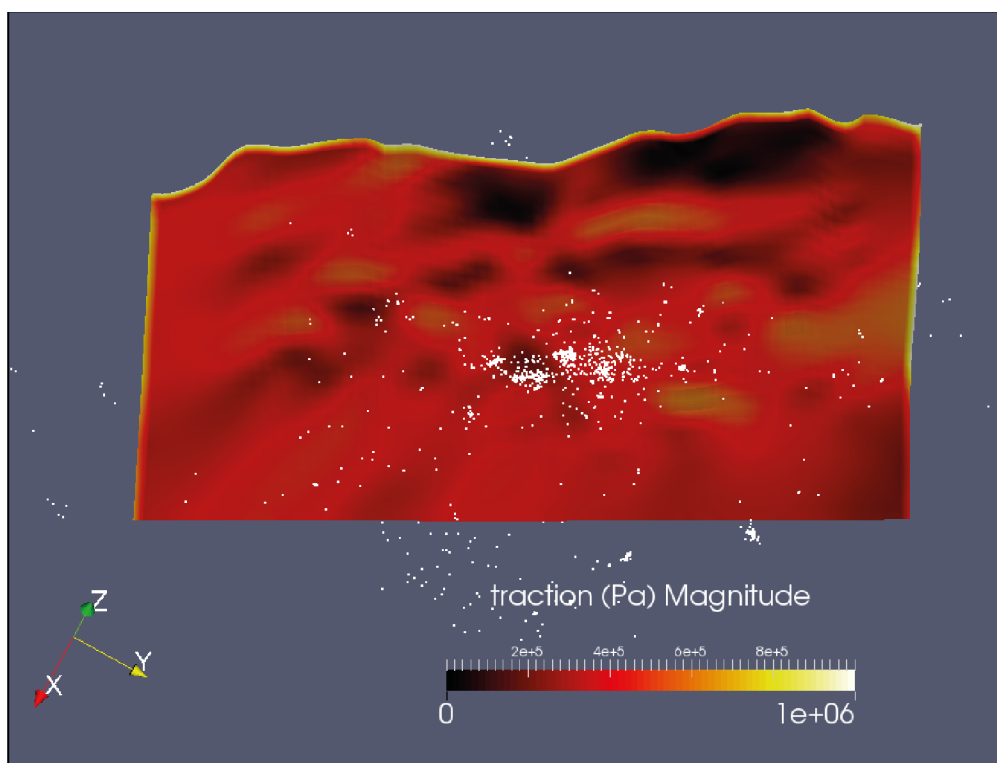


**Fig. 42.** Comparison between the interseismic stress build-up obtained by ATF\_fri model and microseismicity (from Chiaraluce et al., 2007) whole distance from the ATF plane is 2 km. In the future, new data from microseismic event localisation could be helpful to constrain velocity-weakening patches along the ATF.

## **6. Rupture dynamics from 3D Alto Tiberina rough-fault numerical simulations.**

### 6.1. Introduction

In chapter 6, we have seen that the fault roughness affects the interseismic stress build-up along the fault plane: the stress distribution on the ATF is strongly heterogeneous and controlled by asperity with high values of stress that could be the nucleation area for unstable slip along ATF. We have hypothesized that these asperity are surrounding by a velocity strengthening material that could explain the stable slip simulated by 2D and 3D quasi-static models to fit the geodetic velocity field. However stable (creeping) and unstable (earthquakes) fault segments are not separated in space but they can interact in different ways. For example, fault segments that stably slide at low slip rates can become dynamically unstable due to rapid shear heating of pore fluids (Noda and Lapusta, 2011). In addition a seismic rupture may propagate at high sliding velocity along the phyllosilicate rich horizons with velocity strengthening behavior (e.g. Boutareaud et al., 2008; Niemeijer and Spiers, 2006). In this way other velocity weakening segments of the fault could reach the rupture, increasing the maximum magnitude expected. For this reason the seismic potential of the ATF cannot be undervalued. In this chapter we will present the preliminary results of a set of studies on the ATF dynamic rupture. In particular we will quantify how the fault roughness affects the maximum magnitude expected for a seismic event simulated along the ATF, if a slip weakening friction is considered. Two study cases will be discuss: (i) a planar fault (ATFD\_P model) and (ii) a rough-fault (ATFD\_NP model).

## 6.2. Rupture dynamic modeling setup

We perform 3D dynamic numerical simulations of the ATF using a new version of SPECFEM3D code that incorporate dynamic rupture modeling capabilities (Galvez et al., 2013). We build two crustal blocks with dimension 150x150x40 km constituted by a topographic surface as described in chapter 5. In the first block we implement the ATF planar fault, while in the second block the rough-fault (Fig. 43) following the geometry defined in Mirabella et al. (2011). We have imported these crustal blocks in CUBIT (Chapter 3) where an unstructured mesh of 1264971 hexahedral elements is built (Fig. 44). The faults are described by the split-node method (Dalguer and Day; 2007) as in chapter 3. In this way the faults are represented by two matching surfaces in contact. We have defined in CUBIT the crustal domain where the velocity model is applied, the surfaces for the absorbing boundary conditions, the topographic surface and the nodes associated at the fault where a friction law is applied. In order to simulate a spontaneous rupture, we use a linear slip weakening friction law (e.g. Palmer and Rice, 1973; Ida, 1973; Andrews, 1976):

$$\mu = \mu_s - (\mu_s - \mu_d) \min\left(\frac{\delta}{D_c}, 1\right) \quad (38)$$

$$\dot{\delta} = |\dot{s}| \quad (39)$$

where  $\mu_s$  and  $\mu_d$  are the static and dynamic friction coefficient respectively,  $D_c$  the critical slip distance,  $\delta$  and  $\dot{\delta}$  are the magnitude of the slip and slip rate respectively. Even if this friction law is more simple than rate-and state, it represents key features of fault strength: a finite friction coefficient  $\mu$ , progressive weakening ( $\mu_s - \mu_d$ ), and finite fracture energy (Fig. 45):

$$G_c = \frac{1}{2} (\mu_s - \mu_d) D_c \quad (40)$$

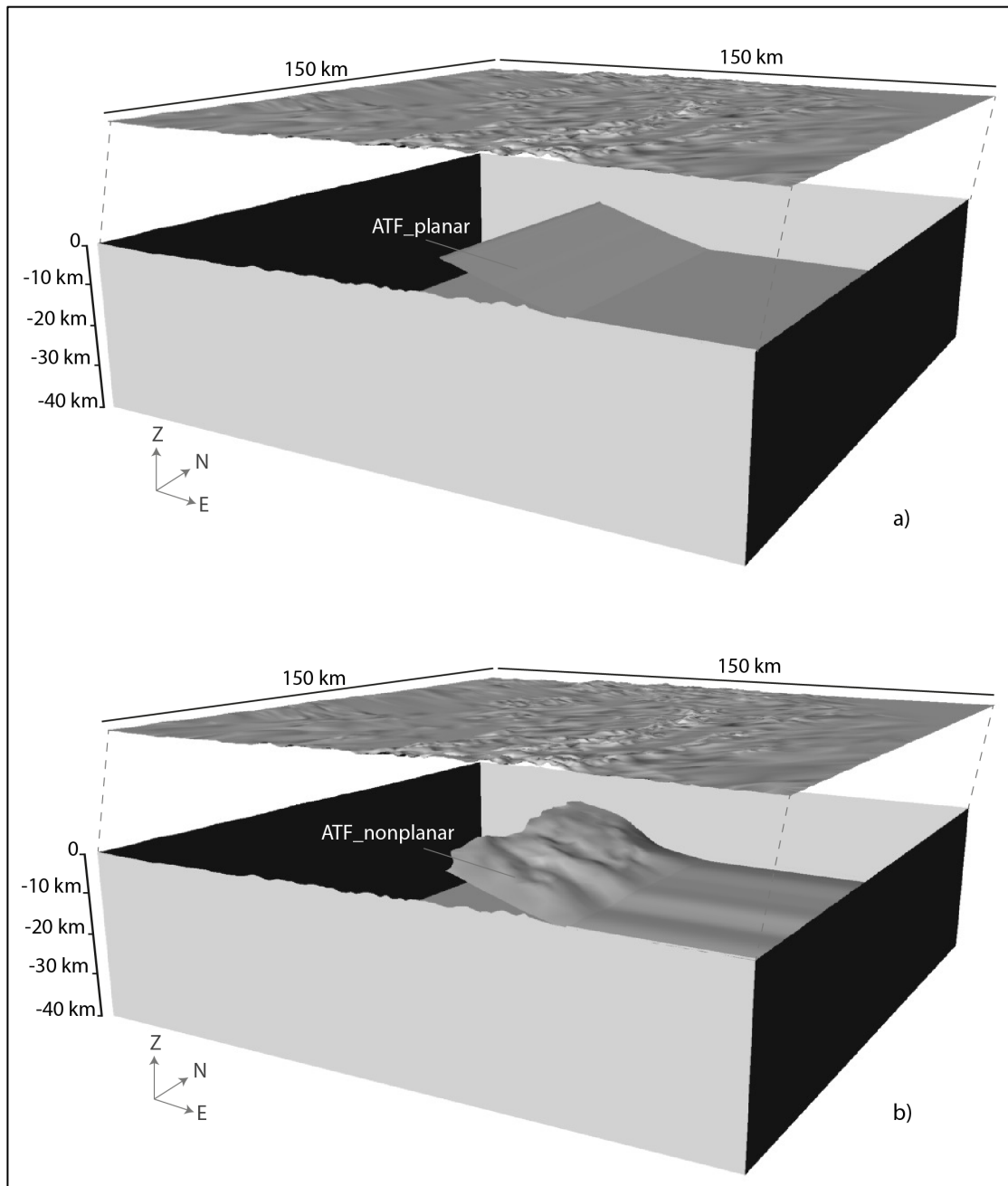


**Fig. 43.** Crustal block and fault geometries used for ATFD\_P (a) and ATFD\_NP dynamic models. Note that in these models a fault plane is used (and no a fault zone as in the 3D quasi-static models). The area of the crustal block is located in figure 33 (Chapter 5).

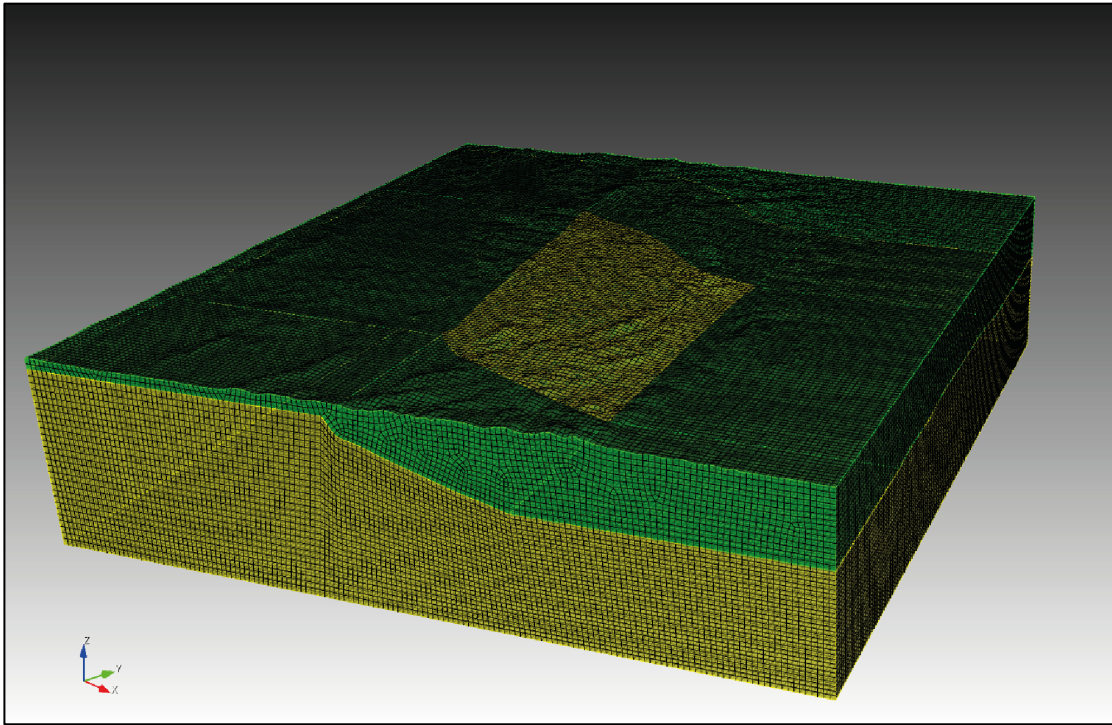


**Fig. 44.** Hexahedral mesh for dynamic models. The mesh is defined by 1264971 elements with length of 1000 m. Along the fault plane the element dimension decrease to 800 m.

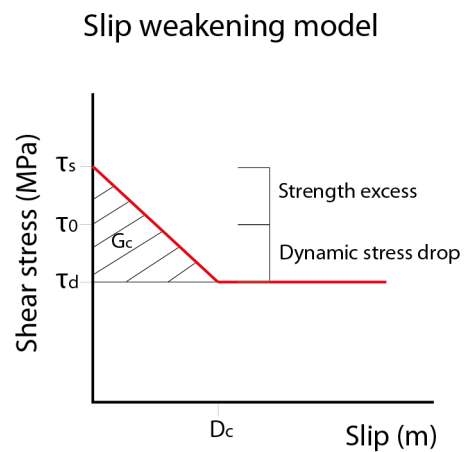


**Fig. 55.** Shear stress evolution curve for a dynamic rupture along the fault plane, where  $\tau_s$ ,  $\tau_0$  and  $\tau_d$  are the static yielding stress, the initial shear stress and dynamic yielding stress respectively. These parameters define the dynamic stress drop and the strength excess.  $D_c$  is the critical slip distance and the dashed area  $G_c$  represents the fracture energy.

In the models the rupture is allowed along the entire fault plans. An homogeneous crust is assumed with elastic properties show in Table 8. The distributions of the initial stresses and frictional parameters on the fault are specified in Table 7. The nucleation occurs in 3 km x 3 km square area that is centered in the fault, as shown in figure 46. The rupture initiates because the initial shear stress in the nucleation patch is set to be slightly higher than the initial static yield stress in that patch (Tab. 7). Then the rupture propagates spontaneously through the fault area (hence outside the nucleation patch), following the linear slip-weakening friction law. The simulation time for both the models is about 40 s. We run the simulations on the INGV cluster ELIOS that has 64 compute nodes, each with 2 quad-core AMD Opteron 2374 processors at 2.4 GHz and with 16 GB RAM (512 total cores, 2 GB RAM/core). The simulations require 5 hours on 128 cores.

	Nucleation	Outside Nucleation
Initial shear stress $\tau_0$ ; MPa	70.4	60
Initial normal stress $-\sigma_n$ ; Mpa	100	100
Static friction coefficient $\mu_s$	0.7	0.7
Dynamic friction coefficient $\mu_d$	0.55	0.55
Static yielding stress $\tau_s = -\mu_s\sigma_n$ ; Mpa	70	70
Dynamic yielding stress $\tau_d = -\mu_d\sigma_n$ ; Mpa	55	55
Dynamic stress drop $\Delta\tau = \tau_0 - \tau_d$ ; Mpa	15.4	5
Strength excess $\tau_s - \tau_0$ ; Mpa	-0.4	10
Critical slip distance $D_0$ ; m	0.3	0.3

**Tab. 7.** Stress and frictional parameters used into and outside the nucleation area.

	Density, kg/m <sup>3</sup>	Shear modulus,Gpa	Poisson's ratio	Vp m/s	Vs m/s
Crust	2590	21.36	0.25	5089	2938

**Tab. 8.** Elastic properties used for the crust.

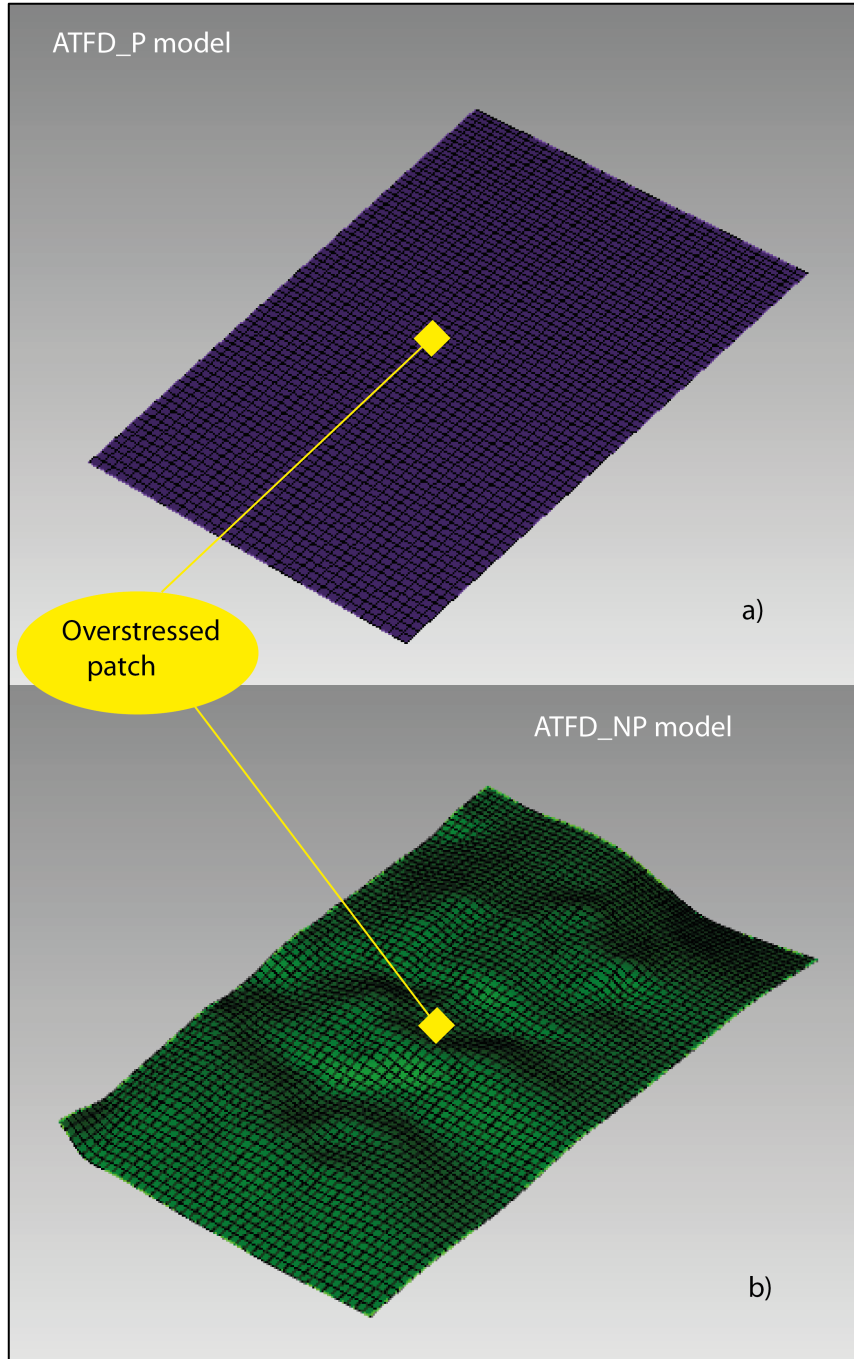


**Fig. 46.** Planar and non planar fault geometries used for the rupture dynamic models. The yellow square (centered at 7.5 km of depth and with side lengths 3000 m) represents the nucleation area defined by different stress and frictional parameters respect to the rest of the fault (see Table 7.).

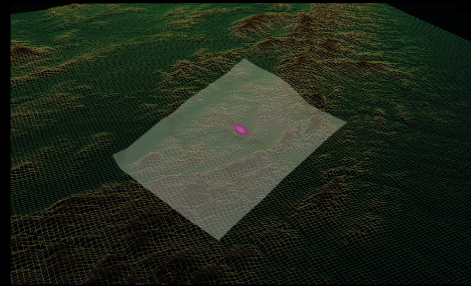
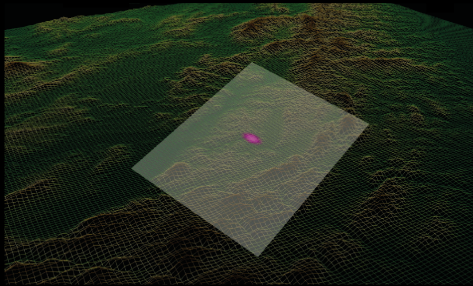
### 6.3. Results

Figure 52 shows the rupture history for ATFD\_P and ATFD\_NP models in terms of the z-component seismic wavefield plotted on the topographic surface and cumulative slip along the fault plane. We can observe that after 1 s the rupture is triggered but is confined at the nucleation patch for both the models. The differences are immediately marked after 5s, in fact the rupture front is faster in ATFD\_P model and, in addition, evolves in a wider area respect to the ATFD\_NP model. At 10s in the planar case, the rupture continues to propagate, in concentric way, around the nucleation patch with the wavefield still localized above the fault plane. On the contrary for the non-planar case the slip distribution is not concentric around the nucleation patch, but is mainly located in the northern sector of the ATF. At 15s, in the ATFD\_P model the rupture covers almost the entire fault plane, while the non-planar fault is yet locked in the southern sector. After 20s we can observe that the seismic wavefield is split due to the rupture propagation along the fault corners for both the models. We underline that no healing is considered, therefore the rupture propagates for the entire fault and reaches the southern sector also in the non-planar case.. Figure 48 shows the last time step for ATFD\_P and ATFD\_NP models. We note that in the planar case the cumulative slip is uniformly distributed on the plane. On the contrary the non-planar model is characterized by a heterogeneous slip distribution and, in particular, higher values are located near the lateral sides. In the central part, instead, some patches have very low values of cumulative slip; in some cases, approximately near to zero.

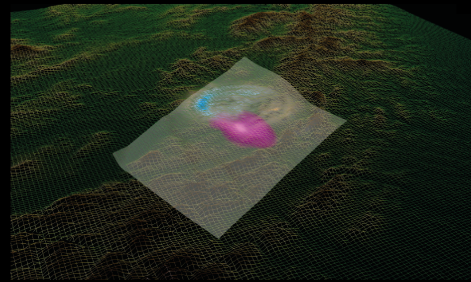
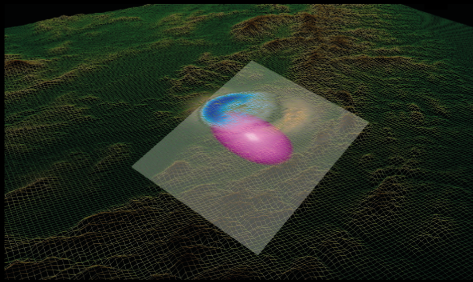
ATFD\_P model

ATFD\_NP model

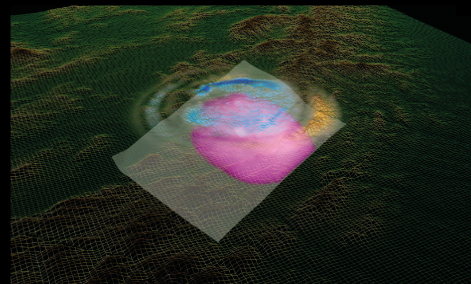
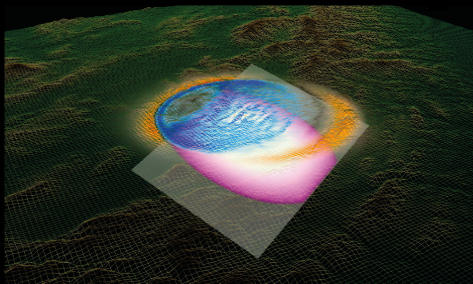
Time: 1 s



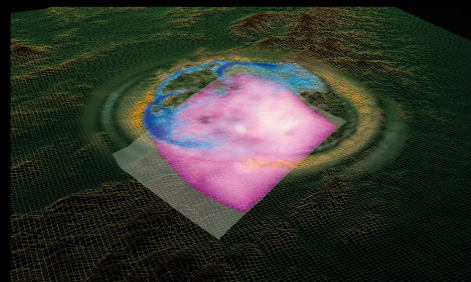
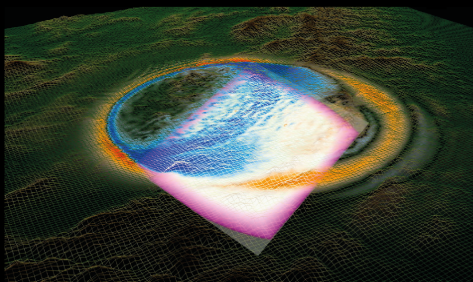
Time: 5 s



Time: 10 s



Time: 15 s



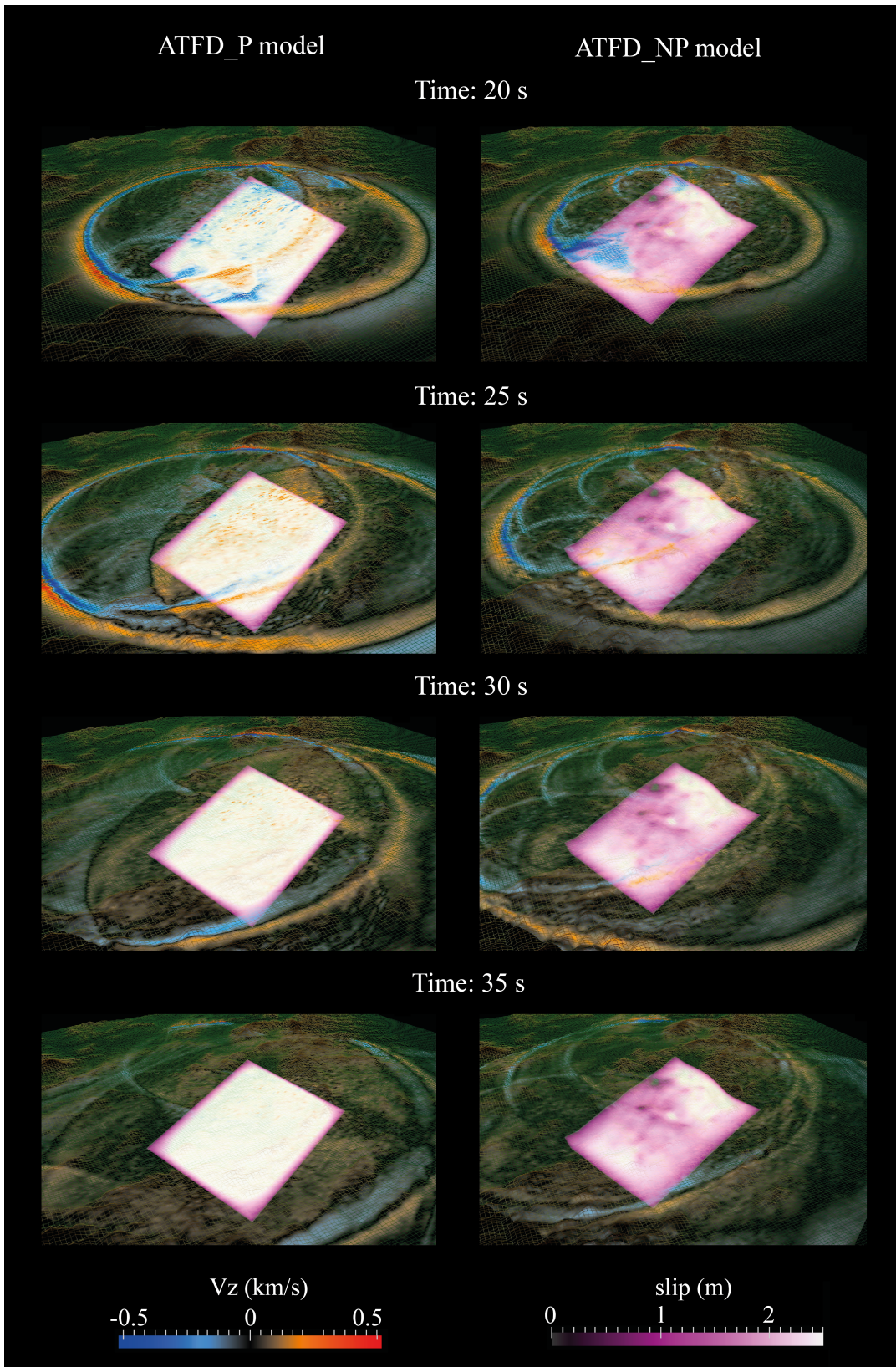


**Fig. 47.** Wave front z-component and cumulative slip for ATFD\_P and ATFD\_NP models at different time steps.



**Fig. 48.** Final time step after 38 s for ATFD\_P and ATFD\_NP models..

These models suggest that the rupture dynamic is strongly controlled by the roughness of the fault plane and in the next paragraph we try to explain what this means in terms of moment magnitude.

#### 6.4. Discussion and concluding remarks

During the last decades 3D numerical simulations have been applied with success to simulate the rupture dynamic of faults and seismic wave propagation in different tectonic setting. Laboratory experiments define performing friction laws that allow us to constrain seismological and geodetic observations in a better way. This is fundamental to reproduce the phenomena (i.e, earthquakes) and to improve our seismological knowledge (i.e, ground motion estimates). However, one of the principal assumptions of these models has been to consider planar fault geometries. This is because the real geometry of the faults is often an incognita or because the computational cost for this type of problem was prohibitive. Nowday, HPC resources, associated with efficient parallel computation code like SPECFEM3D, consent to explore also this aspect of the rupture dynamics.

The results by ATFD\_NP model demonstrate a strong influence of the fault roughness on the cumulative slip and dynamic propagation of the rupture in agreement to other works in literature (e.g. Dieterich and Smith, 2010; Dunham et al., 2011; Shi and Day, 2013) . In particular in the non-planar fault case we observe that the rupture front is initially directed towards the northern side of the plane. This can be due at steeper segment (Fig. 39a) next to the nucleation patch that could work like as instantaneous barrier and direct the rupture towards north. In addition, we observe very low slip values in same patches of the fault associated at restraining slopes, where stress loading leads to a local increase of normal compression (Shi and Day, 2013).

Now we compare the moment magnitude calculated from the ATFD\_P and ATFD\_NP models. At first we define the seismic moment  $M_0 = \mu S |u|$  ; where  $\mu$ , S

and  $\mu$  are the shear modulus, rupture area and average slip respectively. For the ATFD\_P model:  $S = 2.99e9 \text{ m}^2$ ;  $\mu = 2.1e10 \text{ Pa}$  and  $u = 2.2 \text{ m}$ . Then  $M_0 = 1.404e20 \text{ N m}$ . Instead for ATFD\_NP model:  $S = 3.03e9 \text{ m}^2$ ;  $\mu = 2.1e10 \text{ Pa}$  and  $u = 1.17 \text{ m}$ . In this case  $M_0 = 7.555e19 \text{ N m}$ . Finally we obtain the moment magnitude  $M_w = 7.4$  and  $M = 7.2$  for ATFD\_P and ATFD\_NP models respectively. These results obtained, although preliminary, demonstrate that the maximum magnitude expected can decrease if we consider the ATF rough-faults. In this way the fault geometry, when known, can be very important for the seismic hazard. In the future, the effects of differential initial stress and a realistic tomographic model could be taken in account.

## 7. Conclusions

This work aims to understand the deformation pattern and the mechanical behavior associated to the Alto Tiberina fault system. We integrate geological, seismological and geodetic data to build quasi-static and dynamic numerical models to simulate interseismic phase and rupture dynamic. Considering 2D and 3D quasi-static simulations, the following main conclusions can be drawn:

1. The deformation pattern inferred by GPS data is consistent with the Alto Tiberina (that we suggest active from 5 to 15 km of depth) and Gubbio fault activity.
2. The presence of a very compliant Alto Tiberina fault zone (or a free-slip plane) is a first order condition to redistribute the stress in the Umbria-Marche region; the stress bipartition between hanging wall (high values) and footwall (low values) inferred by the Alto Tiberina fault activity is consistent with the microseismicity rates that are higher in the hanging wall respect to the footwall.
3. The interseismic stress build-up along the Alto Tiberina fault is strongly heterogeneous due to the fault roughness. Strong stress accumulations are located near patches with higher dip ( $30^\circ < \text{dip} < 37^\circ$ ) respect to the average dip of the fault ( $17^\circ$ ) where relative low values of stress are calculated. We suggest that the overstressed patches could fail seismically even if a typical Byerlee friction (0.6-0.75) is assumed.

These findings suggest that the mechanical behavior of the Alto Tiberina fault system is characterized by a prevalent seismic behavior above 5 km of depth (and mainly associated at antithetic fault zones) and by a prevalent aseismic behavior below 5 km

of depth (associated at the Alto Tiberina fault zone). We hypothesize that the seismic potential of the Alto Tiberina fault zone could increase if a mechanism of interaction between the overstressed patches is invoked. In this way only complex rupture dynamic numerical models could explain if such mechanism is plausible. In this work we have started to explore this path focusing on the rupture dynamic of rough faults. These results obtained, although preliminary, demonstrate that the maximum magnitude expected, after that an event is simulated on the Alto Tiberina fault, can decrease if we consider the fault plane roughness with important consequences for the seismic hazard estimates.

## References

- Aagaard, B., S. Kientz, M. Knepley, L. Strand, and C. Williams, 2013, *PyLith User Manual, Version 1.9.0*. Davis, CA: Computational Infrastructure of Geodynamics.
- Abers, G.A., Mutter, C.Z., Fang, J., 1997. Shallow dips of normal faults during rapid extension: earthquakes in the Woodlark-D'Entrecasteaux rift system, Papua New Guinea. *Journal of Geophysical Research* 102, 15301–15317.
- Ampuero, J.-P. (2009). Notes on modeling earthquake dynamics with the spectral element method; <http://www.gps.caltech.edu/~ampuero/docs/fsem.pdf>.
- Anderson, E.M., 1951. *The Dynamics of Faulting*, 2nd edition. Oliver and Boyd, Edinburgh, p. 206.
- Anderson, R.E., 1971. Thin-skin distention in the Tertiary rock of southwestern Nevada. *Geological Society of America Bulletin* 105, 1019–1052.
- Andrews, D. J., 1976. Rupture Propagation With Finite Stress in Antiplane Strain, *Journal of Geophysical Research*, 81(20).
- Antonioli, A., D. Piccinini, L. Chiaraluce, and M. Cocco (2005), Fluid flow and seismicity pattern: Evidence from the 1997 Umbria- Marche (central Italy) seismic sequence, *Geophys. Res. Lett.*, 32, L10311, doi:10.1029/2004GL022256.
- Alvarez, W. (1972), Rotation of the Corsica-Sardinia microplate, *Nature*, 248, 309–314.
- Axen, G.J., 2004, Mechanics of low-angle normal faults, in Karner, G., Taylor, B., Driscoll, N., and Kohlstedt, D.L., eds., *Rheology and deformation in the lithosphere at continental margins*: New York, Columbia University Press, p. 46–91.
- Barchi, M., R. Minelli, and G. Pialli, 1998, The crop 03 profile: A synthesis of results on deep structures of the northern Apennines, *Mem. Soc. Geol. Ital.*, 52, 383–400.
- Blacker, T., Knupp, P., Lober, R. R., Melander, D., Sjaardema, G. D., Sample, W. A., Smith, M. K., Tautges, T. J., White, D. R., Benzley, S., Kerr, R., Jankovich, S. R., McRae, D. B., & Panthaki, M., 1994. CUBIT Mesh Generation Environment Users Manual Vol. 1 , Sandia National Laboratories, Albuquerque, NM. 50

- Boncio, P., F. Brozzetti, and G. Lavecchia, 2000, Architecture and seismotectonics of a regional low-angle normal fault zone in central Italy, *Tectonics*, 19, 1038–1055.
- Boutareaud, S., et al., 2008. Clay-clast aggregates: a new textural evidence for seismic fault sliding? *Geophysical Research Letters* 35, L05302. doi:10.1029/2007GL032554.
- Byerlee, J.D., 1978. Friction of rocks. *Pure and Applied Geophysics* 116, 615–626.
- Carmignani, L., and R. Kligfield, 1990, Crustal extension in the northern Apennines: The transition from compression to extension in the Alpi Apuane core complex, *Tectonics*, 9, 1275–1303.
- Carpenter, B.M., Marone, C., Saffer, D.M., 2011. Weakness of the San Andreas Fault revealed by samples from the active fault zone. *Nature Geoscience* 4, 251–254 doi:10.1038/ngeo1089.
- Casarotti, E., Stupazzini, M., Lee, S., Komatitsch, D., Piersanti, A., Tromp, J., 2008, CUBIT and seismic wave propagation based upon the spectral-element method: An advanced unstructured mesher for complex 3D geological media, in Proceedings of the 16th International Meshing Roundtable, vol. 5B.4, pp. 579–597. 16, 19, 51
- Chaljub, E., Komatitsch, D., Vilotte, J. P., Capdeville, Y., Valette, B., & Festa, G., 2007. Spectral element analysis in seismology, in Advances in wave propagation in heterogeneous media, vol. 48 of Advances in Geophysics,
- Chiarabba, C., L. Jovane, and R. Di Stefano (2005), A new view of Italian seismicity using 20 years of instrumental recordings, *Tectonophysics*, 395, 251–268.
- Chiaraluce, L., Chiarabba, C., Collettini, C., Piccinini, D., Cocco, M., 2007. Architecture and mechanics of an active low-angle normal fault: Alto Tiberina Fault, northern Apennines, Italy. *Journal of Geophysical Research* 112, B10310. doi:10.1029/2007JB005015.
- Chiaraluce, L., et al., 2004, Complex normal faulting in the Apennines Thrust and fold belt: The 1997–1998 seismic sequence in central Italy, *Bull. Seismol. Soc. Am.*, 94(1), 99–116.
- Collettini, C., 2011. The mechanical paradox of low-angle normal faults: Current understanding and open questions. *Tectonophysics*, 510, 253–268.
- Collettini, C., Viti, C., Smith, S.F.A., Holdsworth, R.E., 2009, The development of interconnected talc networks and weakening of continental low-angle normal faults. *Geology* 37, 567–570.
- Collettini, C., and M. R. Barchi, 2002, A low angle normal fault in the Umbria region (central Italy): A mechanical model for the related micro-seismicity, *Tectonophysics*, 359, 97–115.

- Collettini, C., Holdsworth, R.E., 2004. Fault zone weakening processes along low-angle normal faults: insights from the Zuccale Fault, Isle of Elba, Italy. *Journal of the Geological Society* 161, 1039–1051.
- Collettini, C., Sibson, R.H., 2001. Normal faults normal friction? *Geology* 29, 927–930.
- Dalguer, L. A. & Day, S. M., 2007. Staggered-grid split-node method for spontaneous rupture simulation, *Journal of Geophysical Research*, 112(B2), B02302.
- Day, S. M., Dalguer, L. A., Lapusta, N., & Liu, Y., 2005. Comparison of finite difference and boundary integral solutions to three-dimensional spontaneous rupture, *Journal of Geophysical Research*, 110(B12), B12307.
- Dieterich, J. H., and D. E. Smith, 2010, Nonplanar faults: mechanics of slip and off-fault damage, in *Mechanics, Structure, and Evolution of Fault Zones*, edited by Y. Ben-Zion and C. Sammis, pp. 1799-1815, Birkhäuser Basel, doi:10.1007/978-3-0346-0138-2\_12.
- Dunham, E. M., Belanger D, Cong L, Kozdon J E, 2011, Earthquake Ruptures with Strongly Rate-Weakening Friction and Off-Fault Plasticity, Part 2: Nonplanar Faults, *BSSA*, 101:2308-2322; doi:10.1785/0120100076.
- Elter, P., G. Giglia, M. Tongiorgi, and L. Trevisan, 1975, Tensional and contractional areas in recent Tortonian to Present evolution of the northern Apennines, *Boll. Geofis. Teorica Appl.*, 17, 2–18.
- Engelder, T., 1993, *Stress Regimes in the Lithosphere*, 475 pp., Princeton Univ. Press, Princeton, N. J.
- Galvez, P., Ampuero J-P, Dalguer L,A, Somala S.N and T. F. Nissen-Meyer, 2013, Dynamic earthquake rupture modeled with an unstructured 3D spectral element method applied to the 2011 M9 Tohoku earthquake, Submitted to *Geophys. J. Int.*
- Gudmundsson, A., 2004. Effects of Young's modulus on fault displacement. *C.R. Geo- sciences*, 336, 85-92.
- Gudmundsson, A, 2011, *Rock Fractures in Geological Processes*. Cambridge University Press.
- Hayman, N.W., Knott, J.R., Cowan, D.S., Nemser, E., Sarna-Wojcicki, A., 2003. Quaternary low-angle slip on detachment faults in Death Valley, California. *Geology* 31, 343–346.
- Hoek, E., 200, *Practical Rock Engineering*, available at <http://www.rocscience.com>.

- Hreinsdottir, S., Bennett, R.A., 2009. Active aseismic creep on the Alto Tiberina low-angle normal fault, Italy. *Geology* 37, 683–686.
- Ida, Y., 1973. Stress Concentration and Unsteady Propagation of Longitudinal Shear Cracks, *Journal of Geo- physical Research*, 78.
- Ismail-Zadeh, A., Tackley, P., 2010, *Cambridge University Press*.
- Jackson, J.A., White, N.J., 1989. Normal faulting in the upper continental crust: observations from regions of active extension. *Journal of Structural Geology* 11, 15–36.
- John, B.E., Foster, D.A., 1993. Structural and thermal constraints on the initiation angle of detachment faulting in the southern Basin and Range: the Chemehuevi Mountains case study. *Geological Society of America Bulletin* 105, 1091–1108. doi:10.1130/0016-7606(1993) 105.
- Jolivet, L., Lecomte, E., Huet, B., Denèle, Y., Lacombe, O., Labrousse, L., Le Pourhiet, L., Mehl, C., 2010. The North Cycladic detachment system. *Earth and Planetary Science Letters* 289, 87–104. doi:10.1016/j.epsl.2009.10.032.
- Kaneko Y., N. Lapusta, and J.-P. Ampuero, 2008, Spectral element modeling of spontaneous earthquake rupture on rate and state faults: Effect of velocity-strengthening friction at shallow depths, *Journal of Geophysical Research*, 113, B09317, doi:10.1029/2007JB005553.
- Keller, J. V. A., G. Minelli, and G. Pialli, 1994, Anatomy of late orogenic extension: The northern Apennines case, *Tectonophysics*, 238, 275 – 294.
- Lavecchia, G., F. Brozzetti, M. R. Barchi, M. Menichetti, and J. V. Keller, 1994, Seismotectonic zoning in east-central Italy deduced from analysis of the Neogene to present deformations and related stress fields, *Geol. Soc. Am. Bull.*, 106, 1107–1120.
- Komatitsch, D., Tsuboi , S., Tromp,J., 2005. The spectral-element method in seismology, in *Seismic Earth: Array Analysis of Broadband Seismograms*, vol. 157 of *Geophysical Monograph*, pp. 205–228, eds Levander, A. & Nolet, G., American Geophysical Union, Washington DC, USA
- Lister, G.S., Davis, G.A., 1989. The origin of metamorphic core complexes and detachment faults formed during Tertiary continental extension in the northern Colorado River region, U.S.A. *Journal of Structural Geology* 11, 65–94.
- Longwell, C.R., 1945. Low-angle normal faults in the Basin and Range province. *Transactions of the American Geophysical Union* 26, 107–118.
- Magnoni, F., 2012, Spectral-Element and Adjoint 3D Full-Wave Tomography for the Lithosphere of Central Italy, [Dissertation thesis], Alma Mater Studiorum Università di Bologna. Dottorato di ricerca in Geofisica, 24. Ciclo.

- Miller, S. A., C. Collettini, L. Chiaraluce, M. Cocco, M. R. Barchi, and J. B. Kraus, 2004, Aftershocks driven by a high-pressure CO<sub>2</sub> source at depth, *Nature*, 427, 724–727.
- Mirabella, F., M. G. Ciaccio, M. R. Barchi, and S. Merlini, 2004, The Gubbio normal fault (central Italy): Geometry, displacement distribution and tectonic evolution, *J. Struct. Geol.*, 26, 2233–2249.
- Mirabella, F., F. Brozzetti, A. Lupattelli, and M. R. Barchi, 2011, Tectonic evolution of a low-angle extensional fault system from restored cross-sections in the Northern Apennines (Italy), *Tectonics*, 30, TC6002, doi:10.1029/2011TC002890.
- Montone, P., M. T. Mariucci, S. Pondrelli, and A. Amato, 2004, An improved stress map for Italy and surrounding regions (central Mediterranean), *J. Geophys. Res.*, 109, B10410, doi:10.1029/2003JB002703.
- Niemeijer, A.R., Spiers, C.J., 2006. Velocity dependence of strength and healing behaviour in simulated phyllosilicate-bearing fault gouge. *Tectonophysics* 427, 231–253.
- Noda H, Lapusta N, 2013, Stable creeping fault segments can become destructive as a result of dynamic weakening. *Nature*, DOI: 10.1038/nature11703
- Palmer, A. C. & Rice, J. R., 1973. The growth of slip surfaces in the progressive failure of overconsolidated clay, *Proceedings of the Royal Society of London*, A 332, 527–548
- Pauselli, C., and C. Federico, 2002, The brittle/ductile transition along the Crop03 seismic profile: Relationship with the geological features, *Boll. Soc. Geol. Ital.*, 121(1), 25–35.
- Pauselli, C., and C. Federico, 2003, Elastic modeling of the Alto Tiberina normal fault (central Italy): Geometry and lithological stratification influences on the local stress field, *Tectonophysics*, 374, 99–113.
- Pauselli, C., M. R. Barchi, C. Federico, B. M. Magnani, and G. Minelli, 2006, The crustal structure of the northern Apennines (central Italy): An insight by the CROP03 seismic line, *Am. J. Sci.*, 306, 428–450.
- Patera, A.T., 1984, Spectraelement method for fluid dynamics: laminar flow in a channel expansion, *J. Comput. Phys.*, 54, 468–488. 3
- Pellegrini, F. & Roman, J., 1996, SCOTCH: A software package for static mapping by dual recursive bipartitioning of process and architecture graphs, *Lecture Notes in Computer Science*, 1067, 493–498. 51

- Peter, D., Komatitsch, D., Luo, Y., Martin, R., Le Goff, N., Casarotti, E., Le Loher, P., Magnoni, F., Liu, Q., Blitz, C., Nissen-Meyer, T., Basini, P., & Tromp, J., 2011. Forward and adjoint simulations of seismic wave propagation on fully unstructured hexahedral meshes, *Geophys. J. Int.*, 186, 721–739. 16, 17, 24, 50, 51, 52, 53, 54, 55, 56
- Pialli, G., M. Barchi, and G. Minelli, 1998, Results of the CROP03 deep seismic reflection profile, Mem. 52., 657 pp., Soc. Geol. Ital., Rome.
- Reches, Z., and T. A. Dewers, 2005, Gouge formation by dynamic pulverization during earthquake rupture, *Earth Planet. Sci. Lett.*, 235, 361–374, doi:10.1016/j.epsl.2005.04.009.
- Reutter, K. J., P. Giese, and H. Closs (1980), Lithospheric split in the descending plate: Observations from the northern Apennines, *Tectonophysics*, 64, T1–T9.
- Rietbrock, A., Tiberi, C., Scherbaum, F., Lyon-Caen, H., 1996. Seismic slip on a low-angle normal fault in the Gulf of Corinth: evidence from high-resolution cluster analysis of microearthquakes. *Geophysical Research Letters* 23, 1817–1820.
- Rolandone, F., R. Bürgmann, D. C. Agnew, I. A. Johanson, D. C. Templeton, M. A. d'Alessio, S. J. Titus, C. DeMets, and B. Tikoff (2008), Aseismic slip and fault-normal strain along the central creeping section of the San Andreas fault, *Geophys. Res. Lett.*, 35, L14305, doi:10.1029/2008GL034437.
- Shi, Z., and S. M. Day, 2013, Rupture dynamics and ground motion from 3-D rough-fault simulations, *J. Geophys. Res. Solid Earth*, 118, 1122–1141, doi:10.1002/jgrb.50094.
- Schon, J. H., 2004, *Physical Properties of Rocks: Fundamental and Principles of Petrophysics*. Oxford: Elsevier.
- Sibson, R.H., 1985. A note on fault reactivation. *Journal of Structural Geology* 7, 751–754.
- Smith, S.A.F., Faulkner, D.R., 2010. Laboratory measurements of the frictional strength of a natural low-angle normal fault. *Journal of Geophysical Research* 115, B02407. doi:10.1029/2008JB006274.
- Tong, X., D. T. Sandwell, and B. Smith-Konter (2013), High-resolution interseismic velocity data along the San Andreas Fault from GPS and InSAR, *J. Geophys. Res. Solid Earth*, 118, doi:10.1029/2012JB009442
- Turner, R. C., R. M. Nadeau, and R. Bürgmann, 2013, Aseismic slip and fault interaction from repeating earthquakes in the Loma Prieta aftershock zone, *Geophys. Res. Lett.*, 40, 1079–1083, doi:10.1002/grl.50212.

Wernicke, B., 1981. Low angle normal faults in the Basin and Range Province: Nappe tectonics in an extending orogene. *Nature* 291, 645–648.

Wernicke, B., 1985, Uniform-sense normal simple shear of the continental lithosphere, *Can. J. Earth Sci.*, 22, 108–125.

Wernicke, B., 1995. Low-angle normal faults and seismicity: a review. *Journal of Geophysical Research* 100, 20159–20174.

## **Acknowledgments**

I'd like to begin with a heartfelt thank you to my tutor, Emanuele Casarotti, for having been an integral guide, always there for me in the hardest moments and for having shared this passion along with me. A thank you to Lauro Chiaraluce and Massimo Cocco for the edifying discussions during the years and for the vision they have towards Geosciences. I also wish to thank Francesco Mirabella and Enrico Serpelloni for having provided important data but foremost because without it this work would have not been possible to carry out. Last but not least a thank you to Professor Jean Paul Ampuero for his kind hospitality during my stay at Caltech and for his precious teachings on the “Fault Rupture Dynamic” field.